A 2500 Square-Degree CMB Lensing Map From Combined South Pole Telescope and Planck Temperature Data, And Cross-Correlation With Large-Scale Structure

A DISSERTATION PRESENTED
BY
YUKI OMORI
TO
THE DEPARTMENT OF PHYSICS

IN PARTIAL FULFILLMENT OF THE REQUIREMENTS
FOR THE DEGREE OF
DOCTOR OF PHILOSOPHY
IN THE SUBJECT OF
PHYSICS

MCGILL UNIVERSITY
MONTRÉAL, CANADA
NOVEMBER 2017

A 2500 Square-Degree CMB Lensing Map From Combined South Pole Telescope and Planck Temperature Data, And Cross-Correlation With Large-Scale Structure

Abstract

The cosmic microwave background (CMB) is one of the prime observables in studying cosmology. With the increased sensitivity and frequency coverage, the recent CMB experiments have allowed us to investigate subtle secondary effects such as gravitational lensing. In this thesis, the theoretical background of CMB lensing is described, and the methods used to reconstruct a map of the gravitational lensing potential is outlined. The methodology is applied to temperature data obtained by the South Pole Telescope and *Planck*, and the resulting lensing map is presented. We perform numerous tests to verify that the lensing map is not dominated by systematic errors.

This lensing map will be correlated with other probes of large-scale structure, namely galaxy density and galaxy weak lensing. We simulate each of these data sets using Flask, a code that produces maps of correlated fields. Using the suite of simulation realizations, we calculate the correlations between the probes and estimate the covariance. The two-point correlation measurements for the individual probes are then combined to constrain cosmology. Finally we discuss the future landscape of multi-probe cosmological analyses.

Abrégé

Le fond diffus cosmologique (CMB) est un des observables les plus importants en cosmologie. Avec une sensibilité accrue au cours des dernières années, les expériences de mesure du CMB nous ont permis de mesurer des effets secondaires subtils, tel que l'effet de lentillage gravitationnel. Dans cette thèse, nous décrivons le cadre théorique de l'effet de lentillage du CMB ainsi que les méthodes utilisées pour reconstruire une carte de potentiel de l'effet de lentille gravitationnelle. Cette méthodologie est appliquée à une carte en température du CMB obtenue à partir de données du télescope du Pôle Sud et du satellite *Planck*; la carte de potentiel résultante est présentée. Nous réalisons plusieurs tests pour vérifier que la carte de lentillage obtenue ne correspond pas principalement à du bruit systématique.

Cette carte de lentillage sera corrélée avec d'autres observations de la structure à grandes échelles, plus particulièrement la densité de galaxies ainsi que le lentillage des galaxies. Nous simulons chacune de ces observations à l'aide de Flask, un code qui produit des cartes de champs corrélés. En utilisant ces simulations, nous calculons les corrélations entre ces observations et estimons la variance. Ces différentes mesures sont ensuite combinées pour contraindre les paramètres cosmologiques. Nous terminons en discutant le futur des analyses de paramètres cosmologiques utilisant ces observations combin es.

Contents

To everyone who is interested in astronomy, astrophysics and cosmology.

"If I have seen further it is by standing on the shoulders of Giants"

–Isaac Newton, 1676

Acknowledgments

I thank my supervisor, Gil Holder, for his guidance over the years and all the cosmological wisdom he has shared with me in addition to interesting quotes and plots about life. I also thank Matt Dobbs for supervising me after Gil's departure from McGill. I would like to thank everyone who I have interacted with at McGill, especially long-term office/Holder group mates Gabrielle Simard and Elinore Roebber for all the useful discussions (both academic and non-academic). I am greatly indebted to Gabrielle for her help in translating the abstract of this thesis to Français. I also greatly appreciate Duncan Hanson for helping me understand CMB weak lensing and creating QUICKLENS which this thesis is heavily dependent on. Special thanks goes to Robert Brandenberger, (who supervised me for M.Sc., but continued to support me throughout my Ph.D. years) and also his group members Elisa Ferreira, Jerome Quintin and Ryo Namba for helping me understand the theoretical aspect of cosmology.

Outside of McGill, I thank all my scientific collaborators. From SPT, I thank Lindsey Bleem, Tom Crawford, Ryan Chown and Kyle Story for their help in data analyses, resources, and providing detailed comments on paper drafts. From DES, I thank my close collaborators Eric Baxter, Chihway Chang, Tommaso Giannantonio, Donnacha Kirk and Elisabeth Krause, who I have worked closely with for several projects. I also thank everyone who was involved in building the telescopes, operating them, and processing the raw data; without those arduous efforts, there would be no data to analyze.

I am grateful to have Yumiko Tamaki, Takao Uno, Momoka Watanabe, Michael Zamfir and Sebastien Guillot around me during my Ph.D. years. Life would have been very different without them.

Last but not least, I thank my father, mother, brother and Konomi for continuously supporting me despite my poor habit of not responding to emails.

Resources

I acknowledge funding from the Natural Sciences and Engineering Research Council of Canada, Canadian Institute for Advanced Research, and Canada Research Chairs program.

Computations were made on the supercomputer Guillimin from McGill University, managed by Calcul Québec and Compute Canada. The operation of this supercomputer is funded by the Canada Foundation for Innovation (CFI), the ministère de l'Économie, de la science et de l'innovation du Québec (MESI) and the Fonds de recherche du Québec - Nature et technologies (FRQ-NT).

Research in this thesis is part of the Blue Waters sustained-petascale computing project, which is supported by the National Science Foundation (awards OCI-0725070 and ACI-1238993) and the state of Illinois. Blue Waters is a joint effort of the University of Illinois at Urbana-Champaign and its National Center for Supercomputing Applications.

Some of the work in this thesis used resources made available on the Jupiter cluster, a joint data-intensive computing project between the High Energy Physics Division and the Computing, Environment, and Life Sciences (CELS) Directorate at Argonne National Laboratory.

This research used resources of the National Energy Research Scientific Computing Center (NERSC), a DOE Office of Science User Facility supported by the Office of Science of the U.S. Department of Energy under Contract No. DE-AC02-05CH11231.

The thesis acknowledges the use of many python packages: Astropy, a community-developed core Python package for Astronomy (Astropy Collaboration et al., 2013), CAMB (Lewis et al., 2000; Howlett et al., 2012), Chain consumer[*], HEALPix (Górski et al., 2005), IPython (Pérez & Granger, 2007), LensPix (Lewis, 2005), Matplotlib (Hunter, 2007), NumPy & SciPy (van der Walt et al., 2011), PolSpice (Chon et al., 2004), Quicklens[†] and TreeCorr (Jarvis, 2015).

[*] https://samreay.github.io/ChainConsumer

[†] https://github.com/dhanson/quicklens

Preface

Chapters 3, 4, 5: A version of this material is published in the Astrophysical Journal as Omori et al. 2017 with the title "A 2500 Square-Degree CMB Lensing Map from Combined South Pole Telescope and *Planck* Data". The input CMB simulations were made by myself, and the foreground components were produced by Zhen Hou. The mock observations of the simulated CMB skies were carried out by Ryan Chown using SPT software. All other works were carried out by myself, including the combining, lensing reconstruction and the validation tests. The paper was mostly written by myself, but comments were provided by the members of the SPT collaboration analysis group (Eric Baxter, Brad Benson, Lindsey Bleem, John Carlstrom, Ryan Chown, Tom Crawford, Gil Holder, William Holzapfel, Christian Reichardt, Gabrielle Simard and Kyle Story).

Chapter 7, Section 7.2: This paper is published in the Monthy Notices of the Royal Astronomical Society as Kirk et al. 2015 with the title "Cross-correlation of gravitational lensing from DES Science Verification data with SPT and *Planck* lensing". I lead this project on the SPT side and am listed as one of the corresponding authors, while Donnacha Kirk lead the project on the DES side. The shear catalogue was provided by the DES shear catalogue group, and the SPT lensing map was provided by Gil Holder. My main contributions were carrying out the cross-correlation calculations, testing the SPT lensing map for systematics errors and the development of the flat-sky calculations. Approximately one third of the text in the paper is written by myself (although this section is rewritten by myself in this thesis).

Chapter 7, sections $7.3 - 7.5$: Some of this material will be presented in the DES×SPT 5×2pt multi-probe methodology paper, which is currently being written. CosmoSIS is mainly developed by Joe Zuntz with large contributions from various members of the DES collaboration. While I take no credit in making the infrastructure, I did contribute to certain modules related to CMB lensing and tSZ bias modelling. Many of other the DES×SPT related modules were developed by Eric Baxter, Donnacha Kirk and Simon Samuroff. Testing of the DES×SPT pipeline was done by Eric Baxter, Chihway Chang and myself. In calculating the tSZ bias, the simulated tSZ map from redMaPPer clusters was produced by Eric Baxter. The testing of the tSZ map, lensing reconstruction, and the tSZ bias calculations were carried out by myself. All the likelihoods presented in this thesis are calculated by myself.

1

Introduction: The CMB and Galaxies

1.1 Cosmic Microwave Background

In the standard paradigm of modern cosmology, the universe began with a Big Bang, and underwent a period of accelerated expansion, known as cosmic inflation. In this framework, microscopic quantum fluctuations were expanded to cosmological scales and these inhomogeneities are hypothesized to have seeded the large-scale structure that we observe today (Guth, 1981; Sato, 1981; Linde, 1982; Albrecht & Steinhardt, 1982).

In the post-inflationary era, the universe continues to expand, and the energy density gradually dilutes, due to the increase in volume and the redshifting of photons. This reduces the probability of a high energy photon ionizing a hydrogen atom, and hence the number of hydrogen atoms increases (Peebles, 1968; Zel'dovich et al., 1969; Dodelson, 2003). At such temperatures, the mean-free path of photons becomes greater than that of the horizon, and photons free-stream without colliding with another particle. This happens more or less isotropically, and we observe

the redshifted view of the surface at which the photons were last scattered. The surface turns out to have a radiation spectrum that is remarkably akin to that of a blackbody (Mather et al., 1990) at a temperature of 2.72548 ± 0.00057 K (Fixsen et al., 2009). The spectral radiance $dE_\nu/d\nu$ peaks at 160.24 GHz or 1.063 mm, and is known as the cosmic microwave background (CMB).

The CMB is a valuable cosmological observable because it gives us insight into the early universe physics. Prior to the photon-free streaming, the photon-baryon fluid plasma was coupled to the underlying density perturbations produced by inflation (Lyth & Riotto, 1999; Dodelson, 2003). In overdense regions, the plasma experiences both an in-fall due to the gravitational potential, as well as outgoing force coming from thermal pressure (the opposite is true for underdense regions), resulting in an oscillatory behaviour known as acoustic oscillations (Hu & Dodelson, 2002). In addition, the nature of these oscillations depend on the composition of the universe (Hu et al., 1997). Therefore, by measuring the statistical properties of these fluctuations, we are probing the state and the content of the universe when it was $379,000$ years old.

1.2 CMB Experiments

The CMB was first observed serendipitously by Penzias and Wilson while they were mapping signals from the Milky Way (Penzias & Wilson, 1965). Prior to their discovery, Gamow 1948 had already predicted that a thermal background emission should exist in a hot early universe scenario. The discovery of the CMB was therefore a direct support for the Big Bang theory, and was a piece of evidence against the steady state model, which was still a viable theory at the time (Durrer, 2015).

In 1989, the *Cosmic Background Explorer* (*COBE*) satellite was launched. Not only did the far-infrared absolute spectrophotometer (FIRAS; Mather et al. 1994) instrument measure the spectrum of the CMB to extreme precision (a measurement that is deemed a major triumph in modern cosmology), the Differential Microwave Radiometer (DMR; Smoot et al. 1992) instrument measured anisotropies beyond the dipole (which was first measured by Conklin et al. 1969) on the CMB at $\frac{\Delta T}{T} \sim \mathcal{O}(10^{-5})$ for the first time, providing evidence that the universe is not per-

fectly isotropic.

The CMB community then advanced towards measuring finer angular scales to characterize the first few acoustic peaks. Although there were several competing experiments that attempted to accomplish this, it is generally regarded that MAT/TOCO (Miller et al., 1999), BOOMERanG (Netterfield et al., 2002) and MAXIMA (Hanany et al., 2000; Lee et al., 2001) experiments provided convincing evidence (Bucher, 2016). These experiments measured the CMB anisotropies down to ~ 0.18 degrees, and the results agreed with each other as well as certain theoretical models. At around the same time, codes that allow efficient and accurate calculations of the CMB power spectrum for a given model, cosmological parameters, and initial perturbations were developed by several groups* (Durrer et al., 2003).

Following the initial detections of the acoustic peaks, NASA launched the *Wilkinson Microwave Anisotropy Probe* (*WMAP*; Bennett et al. 2003a) in 2001. Arguably, *WMAP* is one of the most successful science teams in observational cosmology, and has contributed to "precision cosmology" in many ways. One important result that came out of the *WMAP* experiment was the detection of the gravitational lensing effect (Smith et al., 2007), which was made possible for the first time due to *WMAP*'s sensitivity and large sky coverage.

Following *WMAP*, the *Planck* satellite was launched in 2009 and observed the microwave sky in nine frequency bands ranging from 30 GHz to 850 GHz. The initial temperature maps for all the frequencies were made public in 2013, and the revised maps were released in 2015 in addition to the polarization maps. On the ground, where there are fewer restrictions on the primary mirror size, experiments (e.g. the South Pole Telescope (SPT; Carlstrom et al. 2011), Atacama Cosmology Telescope (ACT; Swetz et al. 2011), POLARBEAR (Arnold et al., 2010)) were designed to make high resolution and low noise maps. Some of the scientific achievements to date include the measurement of the small scale fluctuations (also known as the "damping tail") (Fowler et al., 2010; Das et al., 2011; Keisler et al., 2011; Reichardt et al., 2012; Story et al., 2013), detection of high redshift galaxy clusters (Marriage et al., 2011; Reichardt et al., 2013; Hasselfield et al.,

*This is possible because CMB anisotropies can be described with linear perturbation theory, which is well established (Seljak & Zaldarriaga, 1996; Lewis et al., 2000)

2013; Bleem et al., 2015; de Haan et al., 2016), and the characterization of foregrounds in three frequency channels (George et al., 2015).

In particular, SPT has completed two generations of surveys: (1) the SPT-SZ survey (2008-2011) that observed the temperature fluctuations at ∼1 arcminute resolution using three frequencies 95, 150 and 220 GHz over 2500 deg^2 down to a noise level of approximately 40, 18 and 70 μK-arcmin respectively (Bleem et al., 2015) and (2) the SPT-pol survey (2012-2015) that observed with the same angular resolution at 95 and 150 GHz with added polarization sensitivity over 500 deg^2 to a noise-level of 6 μK-arcmin at 150 GHz (Benson et al., 2014). The third generation camera (SPT-3G) was attached to the telescope in late 2016, and is currently observing the sky.

This thesis is mainly based on the SPT-SZ 150 and *Planck* 143 GHz data, although other auxiliary maps provided by the *Planck* collaboration are used for verification purposes.

1.3 Large-scale Structure

One of the primary goals of galaxy surveys is to map out the large-scale structure of the universe. The distribution of galaxies is not random; the cosmic web consists of highly clustered nodes, planar sheets and filamentary structures. On the other hand, voids with few or no galaxies can also be found (Mo et al., 2010). The origin of these structures can be traced back to the quantum fluctuations that become stretched out by inflation, leaving inhomogeneities in the universe. Regions that start off slightly denser grow faster under the influence of gravity, and continue to grow by accumulating mass over cosmological time scales. Therefore, the large-scale structure that we observe today is the result of both the initial perturbations and their evolution.

The clustering statistics of galaxies can be used to measure the composition of the universe (e.g. cold dark matter cluster more compared to warm dark matter). The *evolution* of clustering provides us insight into the matter density and the nature of dark energy (Munshi et al., 2004; Coil, 2013).

1.4 Galaxy Surveys

Broadly speaking, there are two types of galaxy surveys. First, spectroscopic surveys which use diffraction gratings or grisms to obtain spectra of galaxies. The spectral information is used to determine the physical features, kinematics and chemical compositions of galaxies as well as precise measurements of their redshifts. With the development of multi-object spectrographs, an instrument that is able to take the spectra of multiple objects simultaneously, the cosmological volume one could study with a survey increased dramatically. Two notable redshift surveys of this type are the Two Degree Field Galaxy Redshift Survey (2dFGRS; Colless et al. 2001) and the Sloan Digital Sky Survey (SDSS; York et al. 2000).

While spectroscopic surveys have the benefit of mapping the positions of galaxies in three-dimensions, the downside is the longer exposure time required to reach a certain magnitude, and hence the volume that can be surveyed within a limited observational time is smaller. In contrast, *photometric* surveys use several filters to sample narrow regions of the spectral energy distribution. Although neither the precise three-dimensional information nor the chemical compositions of galaxies are obtained, we are able to map out a larger volume of the universe at a significantly faster rate. Some of the recent photometric galaxy surveys include the Canada-Hawaii-France-telescope Legacy Survey (CFHTLS[†]), Canada-France-Hawaii Telescope Lensing Survey (CFHTLenS; Heymans et al. 2012), Kilo-Degree Survey (KiDS; de Jong et al. 2013), Dark Energy Survey (DES; The Dark Energy Survey Collaboration 2005) and Hyper Suprime-Cam (HSC; Miyazaki et al. 2012).

1.5 ΛCDM

Although arbitrary theories could be sculpted to match observational data, a large number of model parameters are usually required for a theory to agree well with *all* the observational pieces of evidence, given the precision of modern day measurements. One cosmological model that is commonly used to parametrize the universe is the ΛCDM model, which assumes a flat universe

[†]http://www.cfht.hawaii.edu/Science/CFHLS/

dominated by a cosmological constant (Λ) and cold dark matter (CDM), with initial Gaussian fluctuations seeded by inflation.

Six parameters are fit for in the ΛCDM framework (each of which will be explained next): baryon energy density ($\Omega_{\rm b}h^2$), cold dark matter energy density ($\Omega_{\rm c}h^2$), scalar spectral index ($n_{\rm s}$), primordial scalar fluctuation amplitude ($A_{\rm s}$), reionization optical depth (τ) and the Hubble constant ($H_0 = 100h$)[‡].

The expansion of a homogeneous and isotropic universe can be characterized by the Friedmann equation:

$$H^2(t) = \left(\frac{\dot{a}}{a}\right)^2 = \frac{8\pi G}{3}\sum_i \rho_i(t) - \frac{Kc^2}{a^2(t)}, \tag{1.1}$$

where $H(t)$ is the Hubble parameter at a given time, ρ_i are the energy densities of different components, a is the cosmological scale factor defined as $a(t)=1/[1+z(t)]$ (with $z(t)$ the redshift), and K is the Gaussian curvature that could be positive, negative or zero depending on the curvature of the universe. Dividing this equation with $H^2(t)$, we obtain:

$$1 = \sum_i \Omega_i + \Omega_K, \tag{1.2}$$

where we have used $\rho_{\rm crit} = \frac{3H^2}{8\pi G}$, $\Omega_i \equiv \frac{\rho_i}{\rho_{\rm crit}}$, and defined $\Omega_K = -Kc^2/H^2(t)a^2(t)$ ($\Omega_K = 0$ for a spatially flat cosmology).

The density fluctuations in the early universe can be modelled as a simple power law:

$$\mathcal{P}_{\mathcal{R}}(k) = A_{\rm s}\left(\frac{k}{k_0}\right)^{n_{\rm s}-1}, \tag{1.3}$$

where k is the wave number, $A_{\rm s}$ is the amplitude of the fluctuation at a fiducial wavenumber k_0, and $n_{\rm s}$ parametrizes the tilt of the spectrum.

τ is the optical depth of reionization which provides a measure of the line-of-sight free-electron

[‡]The last parameter is occasionally casted differently. For example, Hinshaw et al. 2013 uses Ω_Λ instead of H_0, but the two are related via the Friedmann equation (Equation 1.1). Planck Collaboration et al. 2014b and Planck Collaboration VIII. 2015 use $\theta_{\rm MC}$, which is the angular size of the sound horizon at recombination estimated using CosmoMC.

opacity to the CMB radiation.

1.6 Angular Power Spectra

One of the most commonly used statistics in CMB and galaxy clustering analyses is the angular power spectrum[§], which characterizes the amplitude of fluctuations as a function of angular scales. A map defined over the full sphere $X(\hat{\boldsymbol{n}})$ (where $\hat{\boldsymbol{n}}$ is the directional vector), can be decomposed into different spherical harmonic modes:

$$X(\hat{\boldsymbol{n}}) = \sum_{\ell} \sum_{m=-\ell}^{m=+\ell} x_{\ell m} Y_{\ell m}(\hat{\boldsymbol{n}}), \tag{1.4}$$

where $Y_{\ell m}$ are the spherical harmonic functions, and $x_{\ell m}$ are the coefficients that quantify the contribution of a particular mode to the map:

$$x_{\ell m} = \int d\hat{\boldsymbol{n}} X(\hat{\boldsymbol{n}}) Y^*_{\ell m}(\hat{\boldsymbol{n}}), \tag{1.5}$$

where the integral is taken over all directions. The angular auto-power spectrum C_ℓ of a map $X(\hat{\boldsymbol{n}})$ is defined as the variance of $x_{\ell m}$ for each ℓ:

$$C_\ell^{XX} = \frac{1}{2\ell+1} \sum_{m=-\ell}^{m=+\ell} |x_{\ell m}|^2. \tag{1.6}$$

Similarly, the angular cross-spectrum, that measures the correlation between two maps $X(\hat{\boldsymbol{n}}), Z(\hat{\boldsymbol{n}})$ is given by:

$$C_\ell^{XZ} = \frac{1}{2\ell+1} \sum_{m=-\ell}^{m=+\ell} x^*_{\ell m} z_{\ell m}. \tag{1.7}$$

These auto/cross-spectra are calculated throughout this thesis and are used to characterize temperature fluctuations T, lensing potential ϕ and galaxy over-densities $\delta_{\rm g}$.

[§]A pedagogical review of angular power spectra in the context of CMB analysis is given in Hivon et al. 2002 and Hinshaw et al. 2003

1.7 Thesis Layout

This thesis will discuss about CMB weak lensing, galaxy clustering and galaxy weak lensing, with an emphasis on the CMB weak lensing map, and the cross-correlation with galaxy density and galaxy weak lensing data. The goal of this work is to show how cosmology can be constrained by combining multiple probes simultaneously, which is currently a popular effort in the field.

In Chapter 2, we provide a general overview of gravitational lensing, and some of the key equations will be derived. In Chapter 3, descriptions of the CMB temperature data used in this analysis will be given and the method of combining SPT and *Planck* data will be detailed. In Chapter 4, we describe the methodology used to reconstruct the lensing map from the combined temperature map and systematic error tests and validations of the map are presented in Chapter 5. The theoretical background behind cross-correlations is given in Chapter 6, and measurements made on realistic simulations is presented in Chapter 7. In Chapter 8, the cross-correlation measurements are combined with other probes and are used to produce combined constraints. In Chapter 9, we produce simulations that mimic SPT-3G and DES-Y5 data, and repeat the forecast to investigate the constraining power for these future data sets. Finally, concluding remarks are given in Chapter 10.

1.8 Notation and Conventions

We first define galaxy density as $\delta_{\rm g}(\hat{\boldsymbol{n}}) = (N(\hat{\boldsymbol{n}}) - \langle N \rangle)/\langle N \rangle$, where N is the number of galaxies that fall in a pixel. Following Planck Collaboration XV. 2015 we will use ℓ, m to denote multipole moments for temperature, and L, M to denote multipole moments for lensing. Lensing potential ϕ generated by an isolated over-density will be defined to be *negative*.

1.9 Assumed Cosmology

Throughout the chapters on the topic of CMB lensing reconstruction, we assume a spatially flat ΛCDM *Planck* 2015 cosmology[¶] (Planck Collaboration XV., 2015) with fitted parameters $\Omega_{\rm b}h^2 = 0.0223$, $\Omega_{\rm c}h^2 = 0.118$, $H_0 = 100\ h\text{km s}^{-1}\text{Mpc}^{-1}$ with $h = 0.679$, power spectrum of primordial curvature perturbations with an amplitude (at $k = 0.05\ \text{Mpc}^{-1}$) $A_{\rm s} = 2.14 \times 10^{-9}$, spectral index $n_{\rm s} = 0.968$, optical depth to reionization $\tau = 0.0666$. For the derived parameters, we use an amplitude of the (linear) power spectrum on the scale of $8\ h^{-1}\text{Mpc}$ $\sigma_8 = 0.82$, and we assume one massive neutrino with a 0.06 eV mass. We use the subscript "fid" to denote a quantity calculated from the best-fit *Planck* cosmology.

In chapters that involve DES, we use the cosmology that is adopted by the main DES analysis group: $\Omega_{\rm b}h^2 = 0.0222$, $\Omega_{\rm c}h^2 = 0.117$, $\Omega_{\rm m} = 0.295$, $H_0 = 100\ h\text{km s}^{-1}\text{Mpc}^{-1}$ with $h = 0.688$, $A_{\rm s} = 2.26 \times 10^{-9}$, $n_{\rm s} = 0.968$, and $\tau = 0.08$. σ_8 is set to 0.834, and we assume one massive neutrino with a mass of 0.06 eV.

[¶]base_plikHM_TT_lowTEB_lensing from https://wiki.cosmos.esa.int/planckpla2015/images/6/67/Params_table_2015_limit68.pdf

2

Gravitational lensing

This chapter on the derivation of the deflection angle is based on Mo et al. 2010; Kilbinger 2015 and M. Meneghetti's lecture notes[*]. In the absence of perturbations, light rays travel along the null geodesics of the homogeneous and isotropic Friedmann-Lemaître space-time. It travels such that the comoving separation vector $\vec{x}$ between neighbouring rays follows (Schneider et al., 1992):

$$\frac{d^2\vec{x}}{d\chi^2} + K\vec{x} = 0, \tag{2.1}$$

where $\vec{x}$ is the comoving separation vector, χ is the comoving radial distance and K is the curvature parameter introduced in Section 1.5. Using Equation 2.1, we can consider the path of light rays starting from the observer, which implies the initial conditions:

$$\vec{x}|_{\chi=0} = 0, \quad \frac{d\vec{x}}{d\chi}|_{\chi=0} = \vec{\theta}, \tag{2.2}$$

[*] http://www.ita.uni-heidelberg.de/~massimo/sub/Lectures/gl_all.pdf

where $\vec{\theta}$ is the apparent angular separation between the light rays that the observer sees. The general solution for this equation with the given boundary condition is:

$$\vec{x}_0(\chi) = f_K(\chi)\vec{\theta}, \tag{2.3}$$

where the subscript 0 implies an unperturbed path, and f_K is the curvature parameter that depends on the sign of K

$$f_K(\chi) = \begin{cases} K^{-1/2}\sin(K^{1/2}\chi), & K > 0 \\ \chi, & K = 0 \\ (-K)^{-1/2}\sinh((-K)^{1/2}\chi). & K < 0 \end{cases} \tag{2.4}$$

The universe, however, contains density perturbations. We assume these perturbations to be much smaller than the Hubble radius, and therefore localized. In such a framework, the space-time can be described by the metric:

$$ds^2 = \left(1 + \frac{2\Phi}{c^2}\right)c^2dt^2 - \left(1 - \frac{2\Phi}{c^2}\right)d\vec{x}^2, \tag{2.5}$$

where Φ is the Newtonian gravitational potential. Since for light, $ds = 0$:

$$\begin{aligned} \left(1 + \frac{2\Phi}{c^2}\right)c^2dt^2 &= \left(1 - \frac{2\Phi}{c^2}\right)d\vec{x}^2 \\ \frac{d\vec{x}}{dt} = c' &= c\sqrt{\frac{(1 + \frac{2\Phi}{c^2})}{(1 - \frac{2\Phi}{c^2})}} \sim c\left(1 + \frac{2\Phi}{c^2}\right), \end{aligned} \tag{2.6}$$

where the last term is obtained by assuming $\frac{2\Phi}{c^2} \ll 1$. This is equivalent to photons travelling through a medium with index of refraction $n = c/c' \sim 1 - \frac{2\Phi}{c^2}$[†] , which is where the name *gravitational lensing* originates from. In such a medium, it can be derived[‡] that the apparent angular

[†] $n>1$, $\Phi < 0$

[‡] See for example M. Meneghetti's lecture notes

difference between the lensed and unlensed ray $\vec{\hat{\alpha}}$ is:

$$\vec{\hat{\alpha}} = \frac{2}{c^2}\int_{\lambda_a}^{\lambda_b} \nabla_\perp \Phi d\lambda, \tag{2.7}$$

where λ is a parametrization of the photons' path. In comoving coordinates, the amount of angular deflection is:

$$d\vec{\hat{\alpha}} = \frac{2}{c^2}\nabla_\perp \Phi(\vec{x}, \chi')d\chi', \tag{2.8}$$

and the comoving separation between the perturbed and unperturbed rays at a distance χ is given by:

$$d\vec{x} = f_K(\chi - \chi')d\vec{\hat{\alpha}}. \tag{2.9}$$

From the viewpoint of the observer, the image is located at:

$$\begin{aligned}\vec{x} &= \vec{x}_0 + \int d\vec{x} \\ &= \vec{x}_0 + \frac{2}{c^2}\int_0^\chi f_K(\chi - \chi')\nabla_\perp \Phi(\vec{x}, \chi')d\chi',\end{aligned} \tag{2.10}$$

and in terms of angles (using $\vec{x} = f_K(\chi)\vec{\theta}$), this can be written as:

$$\begin{aligned}\vec{\theta}_0(\chi) &= \vec{\theta}(\chi) - \frac{2}{c^2}\int_0^\chi d\chi' \frac{f_K(\chi - \chi')}{f_K(\chi)}\nabla_\perp \Phi(\vec{x}, \chi') \\ &= \vec{\theta}(\chi) - \vec{\alpha}(\chi),\end{aligned} \tag{2.11}$$

which is the *lens equation*, and $\vec{\alpha}$ is the scaled deflection angle.

In practice, the deflection caused by gravitational lensing is small ($\Phi/c^2 \ll 1$), and therefore, the integral can be taken along the unperturbed path (i.e. using the Born approximation), which sets $\Phi(\vec{x}, \chi') \sim \Phi(f_K(\chi')\vec{\theta}, \chi')$ and $\nabla_\perp \sim \frac{1}{f_K}\nabla_{\vec{\theta}}$. Under this approximation, the deflection angle can be expressed as the gradient of a projected 2D potential defined as:

$$\phi(\vec{\theta}, \chi) = \frac{2}{c^2}\int_0^\chi d\chi' \frac{f_K(\chi - \chi')}{f_K(\chi)f_K(\chi')}\Phi(f_K(\chi')\vec{\theta}, \chi'). \tag{2.12}$$

From Equation 2.11, we can calculate the Jacobian, which gives:

$$\begin{aligned}\nabla_{\vec{\theta}}\vec{\theta_0} &= \begin{bmatrix} \frac{\partial\theta_1}{\partial\theta_1} & \frac{\partial\theta_1}{\partial\theta_2} \\ \frac{\partial\theta_2}{\partial\theta_1} & \frac{\partial\theta_2}{\partial\theta_2} \end{bmatrix} - \begin{bmatrix} \frac{\partial\alpha_1}{\partial\theta_1} & \frac{\partial\alpha_1}{\partial\theta_2} \\ \frac{\partial\alpha_2}{\partial\theta_1} & \frac{\partial\alpha_2}{\partial\theta_2} \end{bmatrix} \\ &= \delta_{ij} - \begin{bmatrix} \frac{\partial^2\phi}{\partial\theta_1\partial\theta_1} & \frac{\partial^2\phi}{\partial\theta_1\partial\theta_2} \\ \frac{\partial^2\phi}{\partial\theta_1\partial\theta_2} & \frac{\partial^2\phi}{\partial\theta_2\partial\theta_2} \end{bmatrix}. \end{aligned} \tag{2.13}$$

The second term is a symmetric matrix which can be separated into a diagonal and a trace-free term:

$$\begin{aligned}\begin{bmatrix} \frac{\partial^2\phi}{\partial\theta_1\partial\theta_1} & \frac{\partial^2\phi}{\partial\theta_1\partial\theta_2} \\ \frac{\partial^2\phi}{\partial\theta_1\partial\theta_2} & \frac{\partial^2\phi}{\partial\theta_2\partial\theta_2} \end{bmatrix} &= \begin{bmatrix} \frac{1}{2}\left(\frac{\partial^2\phi}{\partial\theta_1\partial\theta_1} + \frac{\partial^2\phi}{\partial\theta_2\partial\theta_2}\right) & 0 \\ 0 & \frac{1}{2}\left(\frac{\partial^2\phi}{\partial\theta_1\partial\theta_1} + \frac{\partial^2\phi}{\partial\theta_2\partial\theta_2}\right) \end{bmatrix} \\ &+ \begin{bmatrix} \frac{1}{2}\left(\frac{\partial^2\phi}{\partial\theta_1\partial\theta_1} - \frac{\partial^2\phi}{\partial\theta_2\partial\theta_2}\right) & \frac{\partial^2\phi}{\partial\theta_1\partial\theta_2} \\ \frac{\partial^2\phi}{\partial\theta_1\partial\theta_2} & -\frac{1}{2}\left(\frac{\partial^2\phi}{\partial\theta_1\partial\theta_1} - \frac{\partial^2\phi}{\partial\theta_2\partial\theta_2}\right) \end{bmatrix}. \end{aligned} \tag{2.14}$$

Therefore, the equation can be re-written as:

$$\nabla_{\vec{\theta}}\vec{\theta_0} = (1-\kappa)\begin{bmatrix} 1 & 0 \\ 0 & 1 \end{bmatrix} - \begin{bmatrix} \gamma_1 & \gamma_2 \\ \gamma_2 & -\gamma_1 \end{bmatrix}, \tag{2.15}$$

where we have used

$$\frac{1}{2}\left(\frac{\partial^2\phi}{\partial\theta_1\partial\theta_1} + \frac{\partial^2\phi}{\partial\theta_2\partial\theta_2}\right) = \frac{1}{2}\nabla^2_{\vec{\theta}}\phi = \kappa \tag{2.16}$$

$$\frac{1}{2}\left(\frac{\partial^2\phi}{\partial\theta_1\partial\theta_1} - \frac{\partial^2\phi}{\partial\theta_2\partial\theta_2}\right) = \gamma_1 \tag{2.17}$$

$$\frac{\partial^2\phi}{\partial\theta_1\partial\theta_2} = \gamma_2 \tag{2.18}$$

The first term of Equation 2.15 is the isotropic component of lensing where the size of the image is increased or decreased. The second part quantifies the anisotropic stretching, which converts a circular image into an ellipse (see Figure 2.1). This is called the shear (often written as a com-

plex quantity $\gamma = \gamma_1 + i\gamma_2 = |\gamma|e^{2i\varphi}$, where φ is the angle between the shear components), and is used to measure the lensing signal from the shapes of galaxies. In practice, we measure the moments of the surface brightness:

$$q_{ij} \equiv \int d^2\theta \mathcal{S}^{\rm obs}(\vec{\theta})\theta_i\theta_j, \tag{2.19}$$

and quantify the two components of ellipticity (Dodelson, 2017):

$$\epsilon_1 \equiv \frac{q_{11} - q_{22}}{q_{11} + q_{22} + 2\sqrt{q_{11}q_{22} - q_{12}^2}} \tag{2.20}$$

$$\epsilon_2 \equiv \frac{2q_{12}}{q_{11} + q_{22} + 2\sqrt{q_{11}q_{22} - q_{12}^2}}, \tag{2.21}$$

which we use to define the complex ellipticity $\epsilon = \epsilon_1 + i\epsilon_2 = |\epsilon|e^{2i\varphi}$. For a galaxy with an intrinsic ellipticity $\epsilon^{\rm int}$, the sheared ellipticity is (Seitz & Schneider, 1997):

$$\epsilon^{\rm lensed} = \frac{\epsilon^{\rm int} + g}{1 + g^*\epsilon^{\rm int}} \tag{2.22}$$

when $g \leq 1$, where g is the reduced shear defined as $g = \gamma/(1-\kappa)$. In the weak lensing regime where $\gamma \ll 1$ and $\kappa \ll 1$, this reduces to $\epsilon^{\rm lensed} \approx \epsilon^{\rm int} + g \approx \epsilon^{\rm int} + \gamma$. Furthermore, if we can assume that orientations of the source galaxies are random (although there are physical effects such as intrinsic alignment that violate this assumption; See section 6.1.1), then for a large sample of galaxies, the average intrinsic ellipticity vanishes, and we obtain $\langle\epsilon\rangle = \langle\gamma\rangle$.

Equation 2.16 can be written as:

$$\begin{aligned}\kappa &= \frac{1}{2}\nabla_{\vec{\theta}}\vec{\alpha} \\ &= \frac{1}{c^2}\int_0^{\chi} d\chi' \frac{f_K(\chi')f_K(\chi-\chi')}{f_K(\chi)}\nabla_\perp^2\Phi[f_K(\chi')\vec{\theta},\chi'],\end{aligned} \tag{2.23}$$

and the 2D Laplacian could be described in terms of the 3D Laplacian by adding a second-order derivative along the line of sight $\partial^2/\partial\chi^2$, which vanishes when an integration is performed (con-

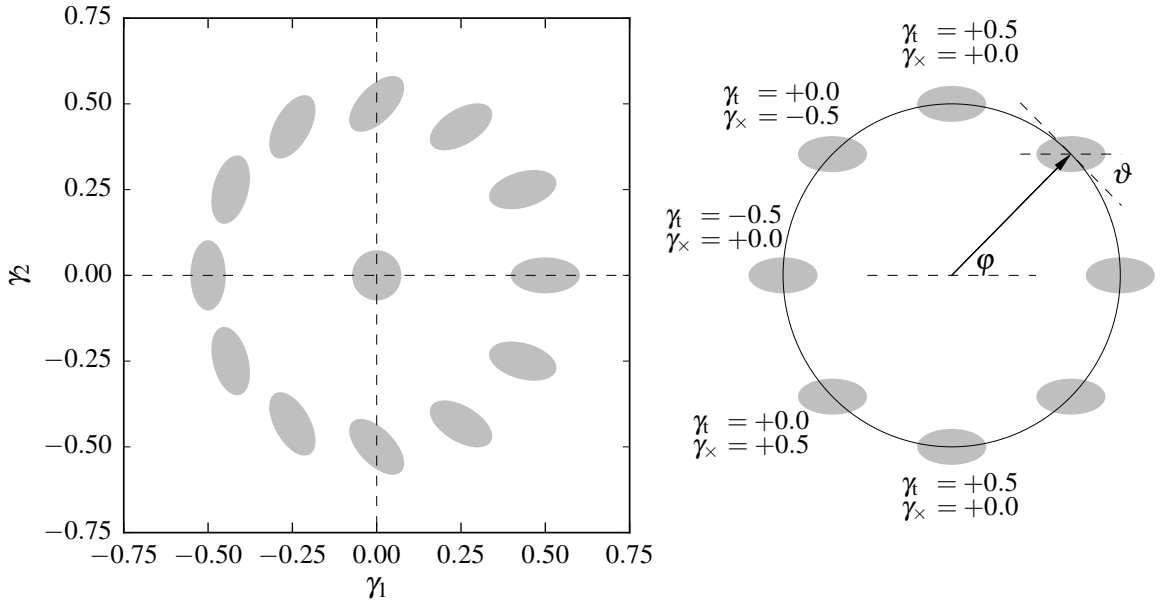

Figure 2.1 **Left:** definitions of γ_1 and γ_2. In the case of no shear, $\gamma_1 = 0$ and $\gamma_2 = 0$ as shown in the centre. The shapes are with respect to the xy-coordinates of the image, which in practice are lines of equal right ascension and declination in the limit of small sky area. **Right:** values of tangential shear and cross shear as the sample galaxy represented in grey is rotated around a reference point at the centre (discussed in Section 7.4).

tributions coming from behind and in front of the lens cancel out). The 3D Laplacian of the potential is related to the mass density via the Poisson equation, which in comoving coordinates can be written as (see e.g. Bertschinger 1995):

$$\begin{aligned}\nabla^2\Phi &= 4\pi G a^2 \rho_{\rm m} \\ &= 4\pi G a^{-1} \bar{\rho}_{\rm m,0}(\delta + 1) \\ &= a^{-1}\frac{3H_0^2\Omega_{\rm m,0}}{2}(\delta + 1)\end{aligned} \tag{2.24}$$

where we have used $\delta = (\rho_{\rm m} - \bar{\rho}_{\rm m})/\bar{\rho}_{\rm m}$, which is the definition for matter over-densities and $\bar{\rho}_{\rm m} = \bar{\rho}_{\rm m,0}/a^3$ which is the redshift scaling relation for non-relativistic matter. Substituting these

into Equation 2.23, we obtain an expression for convergence:

$$\kappa(\vec{\theta},\chi) = \frac{3H_0^2\Omega_{\mathrm{m},0}}{2c^2}\int_0^{\chi} d\chi' \frac{f_K(\chi')f_K(\chi-\chi')}{f_K(\chi)}\frac{\delta[f_K(\chi')\vec{\theta},\chi']}{a(\chi')}, \tag{2.25}$$

where the background term was ignored. What we often want to calculate is the mean projected convergence for the source population (for galaxies, there is a spread in χ). In such a case, we integrate the convergence up to the comoving horizon distance χ_*, and model the redshift distribution of the sources:

$$\kappa(\vec{\theta}) = \int_0^{\chi_*} d\chi G(\chi)\kappa(\vec{\theta},\chi), \tag{2.26}$$

where $G(\chi)$ describes the distribution of the sources. Plugging Equation 2.25 into 2.26 :

$$\kappa(\vec{\theta}) = \frac{3H_0^2\Omega_{\mathrm{m},0}}{2c^2}\int_0^{\chi_*} d\chi' W(\chi')f_K(\chi')\frac{\delta[f_K(\chi')\vec{\theta},\chi']}{a(\chi')} \tag{2.27}$$

where $W(\chi')$ is the lensing efficiency or the kernel:

$$W(\chi') = \int_{\chi'}^{\chi_*} d\chi G(\chi)\frac{f_K(\chi-\chi')}{f_K(\chi)} \tag{2.28}$$

Equation 2.27 describes the projected convergence signal for a given direction $\vec{\theta}$. This is a general formulation, and can be used to describe convergence calculated from both galaxy weak lensing and CMB weak lensing. We return to this equation in Section 6.1.

3

CMB Temperature Data

3.1 SPT Data

The South Pole Telescope (SPT; Carlstrom et al. 2011) is a 10-m telescope located at the National Science Foundation Amundsen-Scott South Pole Station in Antarctica. From 2008 to 2011, the telescope was used to conduct the SPT-SZ survey, a survey that mapped approximately 2500 deg^2 of the southern galactic cap (Story et al., 2013). The survey footprint extends from 20^h to 7^h in right ascension (R.A.) and from $-65°$ to $-40°$ in declination (decl.). The full 2500 deg^2 field is divided into 19 sub-fields, with roughly 1 degree of overlapping coverage at the field boundaries. These fields were observed at three frequency bands centred at roughly 95, 150, and 220 GHz. For this analysis, we exclusively work with the 150 GHz data, since the noise level for this channel is the lowest out of the three. The main lobe of the 150 GHz beam could be approximated by an azimuthally symmetric, two dimensional Gaussian with a full width at half maximum (FWHM) of $1.2'$ (Crawford et al., 2016) for the scales used in this analysis. Although the noise

levels vary field-per-field, the typical noise level of SPT-SZ maps at 150 GHz is 18 μK-arcmin. The maps were made by combining a large number of left-going and right-going scans performed along constant declination, with small steps in elevation between scans. Since both left and right-going scans equally measure the underlying astrophysical signal (which is invariant over the timescale of telescope scans), these are added to increase the signal-to-noise ratio of the map. By taking the difference between the left and right going scans, the underlying signal is removed, and an estimate of the noise can be obtained.

3.2 Planck Data

The *Planck* satellite, launched in 2009 by the European Space Agency (Planck Collaboration I., 2015), was used to observe the millimeter sky in nine frequency bands ranging from 30 to 857 GHz using both the high-frequency instrument (HFI; Planck Collaboration VIII. 2015) and the low-frequency instrument (LFI; Planck Collaboration et al. 2016a). It achieved better resolution, higher sensitivity, and a wider range of frequencies than its predecessor, the *Wilkinson Microwave Anisotropy Probe* (*WMAP*; Bennett et al. 2003b). In this work, we use the publicly available *Planck* 143 GHz map[*] and beam[†] provided in the 2015 data release (Planck Collaboration VIII., 2015). This *Planck* channel was chosen because it contains the greatest overlap with the SPT-SZ 150 GHz channel. The 143 GHz beam function is similar to an azimuthally symmetric Gaussian beam with a FWHM of $\sim 7'$, and the instrument noise is approximately white with an RMS of ~ 30 μK-arcmin over 67% of the sky (Planck Collaboration VIII., 2015) and ~ 27 μK-arcmin over the SPT 2500 deg^2 patch.

[*] http://irsa.ipac.caltech.edu/data/Planck/release_2/all-sky-maps/maps/HFI_SkyMap_143_2048_R2.02_full.fits

[†] http://irsa.ipac.caltech.edu/data/Planck/release_2/ancillary-data/HFI_RIMO_Beams-100pc_R2.00.fits

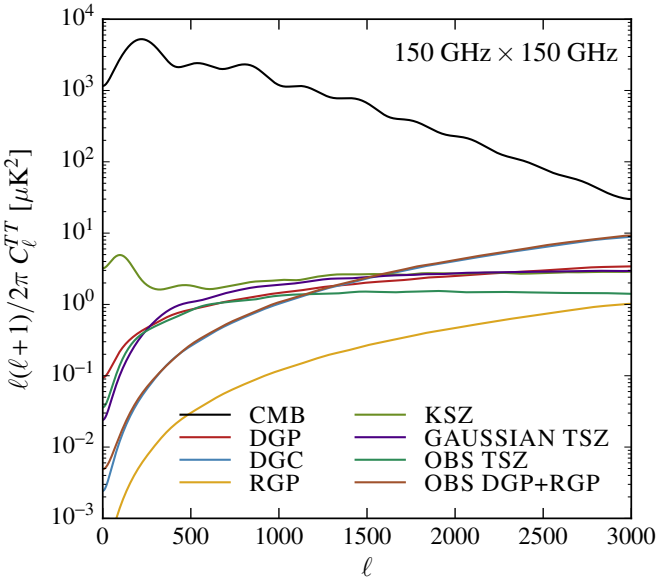

Figure 3.1 Input power spectra for the lensed CMB, and all the other foreground components at 150 GHz. Two components based on data are added: Poisson dusty and radio galaxies (obs DGP+RGP), and observed tSZ emission (obs tSZ). Gaussian realizations of the other components are generated using the derived spectra presented in George et al. 2015.

3.3 Simulations

Simulations of the temperature and noise maps are used to obtain key building blocks of this analysis including the SPT-SZ transfer function and the average noise $\langle |n_{\ell m}|^2 \rangle$, which are used to define the weights used in the combining process (described in Section 3.4).

Simulated temperature maps consist of four components.

(i) Lensed CMB.

(ii) Gaussian foregrounds: thermal Sunyaev-Zel'dovich effect (tSZ), kinetic Sunyaev-Zel'dovich effect (kSZ), cosmic infrared background (CIB), and unresolved faint radio sources in the flux density range F_{150}<6.4 mJy.

(iii) Individually detected point sources: radio and dusty star forming galaxies.

(iv) Detected galaxy clusters.

For (i), lensed CMB maps are produced by running LensPix (Lewis, 2005) with an unlensed temperature power spectrum $C_\ell^{TT,\mathrm{unl}}$ calculated using CAMB (Lewis et al., 2000) with cosmological parameters defined in Section 1.9 as input. We produce maps in HEALPix format with $N_{\mathrm{side}} = 8192$ and apply a cut-off in the input spectrum at $\ell_{\mathrm{max}} = 9500$. The resulting lensed maps are consistent ($< 2\%$ difference) with the theoretically calculated lensed spectrum $C_\ell^{TT,\mathrm{len}}$ up to $\ell \sim 7000$. For each realization of the lensing potential, we lens two background CMB maps, which yields two sets of lensed CMB maps. The purpose of this second set will be explained in Chapter 4. For (ii), we add simulated Gaussian foreground components. The shapes of the tSZ and kSZ spectrum are taken from Shaw et al. (2010) and Shaw et al. (2012) models, respectively, with the amplitudes calibrated to match with George et al. (2015). A similar procedure is followed for the CIB component using templates from George et al. (2015). For the clustered CIB component, the spectrum is set to follow $D_\ell \propto \ell^{0.8}$ (where $D_\ell = \ell(\ell+1)/2\pi \times C_\ell$) with an amplitude of $D_{3000}^{\mathrm{clus}} = 3.46\ \mu\mathrm{K}^2$. The shot-noise or "Poisson" CIB power from galaxies dimmer than 6.4 mJy is taken to be $D_{3000}^{\mathrm{Poisson}} = 9.16\ \mu\mathrm{K}^2$. For the unresolved faint radio sources, we generate random realizations using dN/dS taken from De Zotti et al. (2005), and calibrate the amplitude using SPT-SZ 150 GHz observations. Correlations between these Gaussian foreground components were neglected[‡].

We place point sources at the observed locations with their measured fluxes for point sources in the flux density range $6.4 < F_{150} < 50$ mJy listed in the SPT-SZ point source catalogue (Everett et al. 2017, in preparation). The SPT-SZ point source catalogue is listed in units of intensity MJy/sr. We first compute the energy that falls into a HEALPix pixel (using $N_{\mathrm{side}} = 8192$) and convert this into CMB temperature by applying the conversion factor:

$$\frac{\Delta T\ \ [\mathrm{K_{CMB}}]}{I\ \ \ [\mathrm{MJy/sr}]} = \frac{c^2}{2\nu k_{\mathrm{B}}} \frac{(\exp(x)-1)^2}{x^2 \exp(x)} \tag{3.1}$$

[‡]Realistically there is a tSZ-CIB correlation as shown in George et al. 2015, but the correlation amplitude is small, and hence such consideration will be left for future works.

where ν is the frequency, $x = h\nu/k_{\rm B}T_{\rm CMB}$ with $T_{\rm CMB} = 2.7255$ K. Similarly for (iv), we add clusters with detection significance $\mathrm{S/N}_{\rm clus} > 4.5$[§] listed in Bleem et al. (2015) and model the Compton y profile using a projected β model (Cavaliere & Fusco-Femiano, 1976):

$$y_{\rm tSZ}^{0.75'} = 2\pi \int_0^{0.75'} y_{\rm tSZ,0}(1+\theta^2/\theta_c^2)^{(1-3\beta)/2}\theta d\theta, \tag{3.2}$$

with $\beta = 1$, where $y_{\rm tSZ,0}$ is the peak Comptonization, $y_{\rm tSZ}^{0.75'}$ is the integrated Comptonization within a $0.75'$ radius (Bleem et al., 2015), θ is the angular separation from the centre of the cluster, and $\theta_{\rm c}$ is the cluster core scale. This measurement is converted into temperature using:

$$\Delta T = T_{\rm CMB} g(\nu) y \tag{3.3}$$

where $g(\nu) = x\coth(x/2) - 4$ with $x = h\nu/k_{\rm B}T_{\rm CMB}$ (Carlstrom et al., 2002). This effect causes a temperature decrement around clusters for frequencies less than 217 GHz and an increase for above, as shown in Figure 3.2. From the sum of all these inputs, we produce the simulated SPT-SZ and *Planck* maps separately.

For SPT-SZ simulations, the input HEALPix maps are passed through a mock observing pipeline, which creates mock time-ordered data for each detector, filters those data in the same manner as the real data, and creates maps using the inverse-noise weights from the real data. The observation runs for each of the fields are co-added and the beams are deconvolved using the beam models associated with those fields. All the fields are then reconvolved with a FWHM $= 1.75'$ Gaussian beam, projected onto a single HEALPix map of $N_{\rm side} = 8192$, and then stitched to produce a map that spans over 2500 deg^2.

From the noise-free mock maps, we calculate the filter transfer function:

$$\mathcal{Y}_{\ell m} = \frac{\langle T_{\ell m}^{\rm out} T_{\ell m}^{\rm in,*}\rangle}{\langle T_{\ell m}^{\rm in} T_{\ell m}^{\rm in,*}\rangle}, \tag{3.4}$$

[§]in Bleem et al. 2015 ξ is used to denote the signal-to-noise ratio. We avoid this notation and reserve ξ for two-point angular correlations.

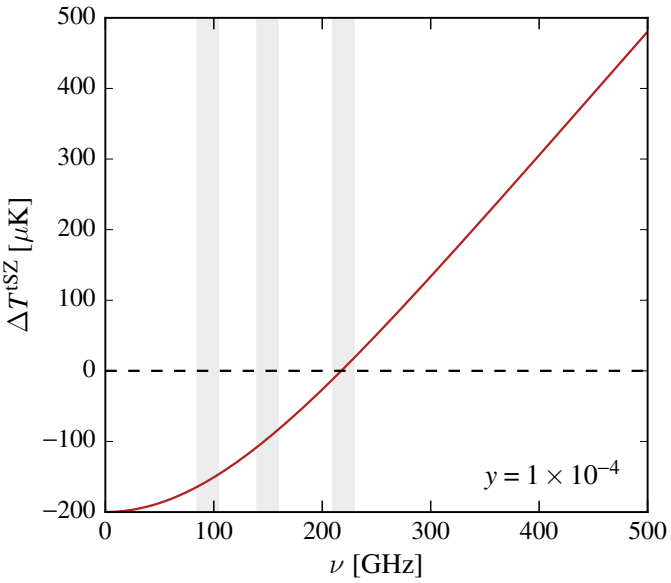

Figure 3.2 Temperature decrement caused by the tSZ effect for a range of frequencies. The grey bands correspond to the SPT-SZ 95, 150 and 220 GHz channels. Compton y parameter is assumed to be 1×10^{-4}.

where the $T_{\ell m}$ are computed from 200 boundary masked temperature maps, and the superscripts "out" and "in" refer to the outputs and inputs of the mock observing pipeline. The filter transfer function encodes how the input data is transformed when passed through the observation pipeline, and is deconvolved from the outputs of the real observations to obtain the estimated true sky signal. Noise maps are produced separately by taking the difference between two SPT-SZ observations, which effectively removes the underlying signal and leaves noise behind. We add noise maps obtained in this way to the noise-free simulation outputs to produce realistic data-like maps.

To produce simulated *Planck* maps, we simply convolve the input signal maps by the *Planck* 143 GHz beam and add noise from the 8th Full Focal Plane simulation set (FFP8; Planck Collaboration XII. 2016). We assume the SPT-SZ 150 and *Planck* 143 GHz channels to have similar bandpass responses to foreground signal, and therefore, do not introduce additional free parameters correcting for the small difference.

3.4 Combining SPT-SZ and Planck

To form the nearly optimal combination of SPT-SZ and *Planck* data, we create the inverse-variance-weighted sum of the two data sets in harmonic-space, after deconvolving the beam and filtering from each data set. To avoid position-space artifacts, we apodize the data and mask bright sources and galaxy clusters before transforming to harmonic-space, and we mask some noisy ℓ, m modes before transforming the combination back to position-space. Each of these steps are described in more detail below.

3.4.1 Boundary Mask

A binary mask defined by the nominal SPT region ($20^h < \text{R.A.} < 7^h$ and $-65° < \text{decl.} < -40°$) is first produced. The PROCESS_MASK routine in the HEALPix package is then used to calculate the distance from the nearest masked pixel, and this distance map is smoothed using a Gaussian beam of FWHM = $15'$. This smoothing is applied to soften the corners of the mask. The distance map is then used to apodize the binary mask with a Gaussian beam of FWHM = $20'$. This results in a mask with an effective area of ~ 2350 deg^2 which we apply to both SPT-SZ and *Planck* maps.

3.4.2 Bright Point Source and Cluster Masking

The brightest point sources are removed at the stage of time-stream filtering. We revisit these locations in the map and mask these regions to avoid artifacts which result from applying spherical harmonic transforms on band-limited maps. Apertures of radii $R = 6'$ and $R = 9'$ are placed at the locations of point sources with $50 < F_{150} < 500$ mJy, and $F_{150} > 500$ mJy respectively. In addition, clusters above $\text{S/N}_{\text{clus}} > 6$ are masked with an aperture of $R = 6'$.

3.4.3 Noise-Weighted Combining

The CMB maps from SPT-SZ and *Planck* have different noise characteristics, in particular as a function of ℓ or angular scale as shown in Figure 3.3. The maps are optimally combined such

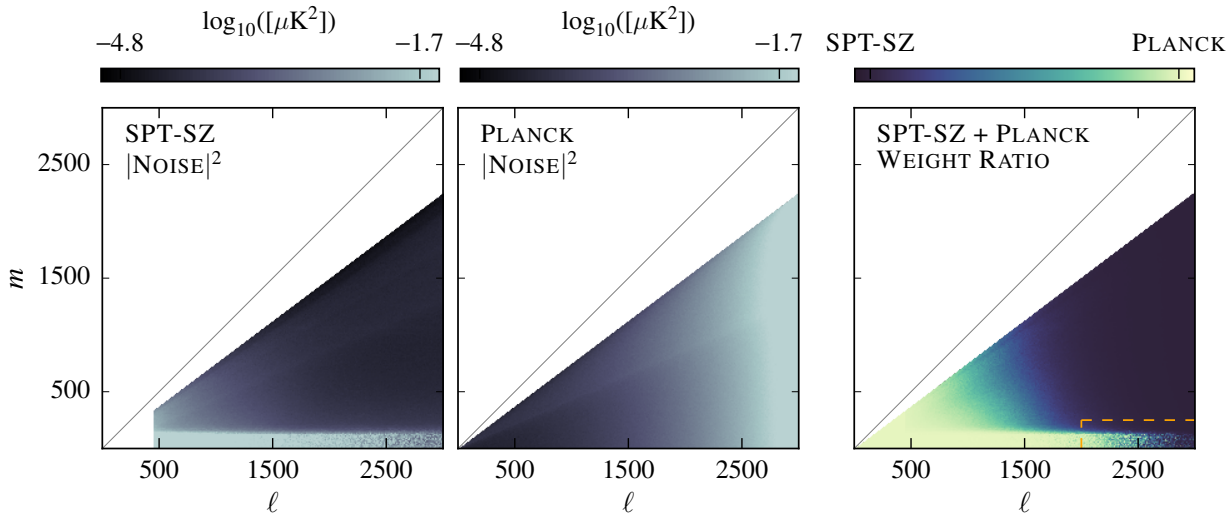

Figure 3.3 Noise characteristics of SPT-SZ and *Planck* data, and the ratio of weights used in combining the data, all shown on (ℓ, m) grids. **Left:** transfer-function-deconvolved SPT-SZ noise obtained by taking the difference between the left-going and right-going scans. The noisy low m stripe is due to the scanning strategy of SPT-SZ. **Centre:** beam-deconvolved *Planck* noise. **Right:** ratio of weights for SPT-SZ and *Planck*. In all the panels, high m modes ($m > 0.75\ell$) where the values are small due to the mask, have been zeroed out to retain the scale.

that the resulting map has lower noise than the individual maps alone at all scales, which is advantageous for lensing map reconstruction. This is achieved by constructing a simple linear combination of SPT-SZ and *Planck* in harmonic-space, weighted by their relative noise variance for each mode (ℓ, m):

$$w_{\ell m}^{\rm SPT} = \frac{1}{\langle |n_{\ell m}^{\rm SPT}/\mathcal{Y}_{\ell m} b_\ell^{\rm SPT}|^2 \rangle} \tag{3.5}$$

$$w_{\ell m}^{Planck} = \frac{1}{\langle |n_{\ell m}^{Planck}/b_\ell^{Planck}|^2 \rangle} \tag{3.6}$$

$$T_{\ell m}^X = \left(\frac{w_{\ell m}^{\rm SPT}}{w_{\ell m}^{\rm SPT} + w_{\ell m}^{Planck}} \frac{T_{\ell m}^{\rm SPT}}{\mathcal{Y}_{\ell m} b_\ell^{\rm SPT}} + \frac{w_{\ell m}^{Planck}}{w_{\ell m}^{\rm SPT} + w_{\ell m}^{Planck}} \frac{T_{\ell m}^{Planck}}{b_\ell^{Planck}} \right) b_\ell^{1.75'}, \tag{3.7}$$

where $b_\ell^{\rm SPT}, b_\ell^{Planck}$ are the beams, $\mathcal{Y}_{\ell m}$ is the SPT-SZ transfer function calculated using Equation 3.4, $n_{\ell m}^{\rm SPT}$, $n_{\ell m}^{Planck}$ are the noise estimates for SPT-SZ and *Planck*, $w_{\ell m}^{\rm SPT}$ and $w_{\ell m}^{Planck}$ are the weights, $T_{\ell m}^{\rm SPT}, T_{\ell m}^{Planck}$ are the beam *convolved* temperature multipole moments, and $T_{\ell m}^X$ is the output combined SPT-SZ + *Planck* spherical harmonic coefficients convolved with a FWHM=1.75′ Gaussian beam $b_\ell^{1.75'}$.

The SPT-SZ data map and the noise maps are calibrated to match with the *Planck* 143 GHz data using results from Hou et al. 2017. We evaluate the sensitivity of the lensing results to the exact value of this calibration factor in section 5.5.2.6.

3.4.4 Masking of modes

Low-m modes from SPT-SZ are noisy, primarily due to the combination of $1/f$ noise, the atmosphere, and the SPT-SZ scanning strategy. Low-ℓ, low-m modes are improved by the combining procedure since *Planck* has relatively low noise for those modes. High-ℓ, low-m modes, however, are noisy in both data sets and hence in the combination. Transforming $T_{\ell m}$ into maps that contain noisy modes translate to anisotropic noise that is difficult to treat in position-space. We therefore mask these modes by setting them to zero. In our baseline analysis, we set all modes $\ell > 2000$ and $m < 250$ to zero (shown as the area enclosed by the orange dashed lines in Figure

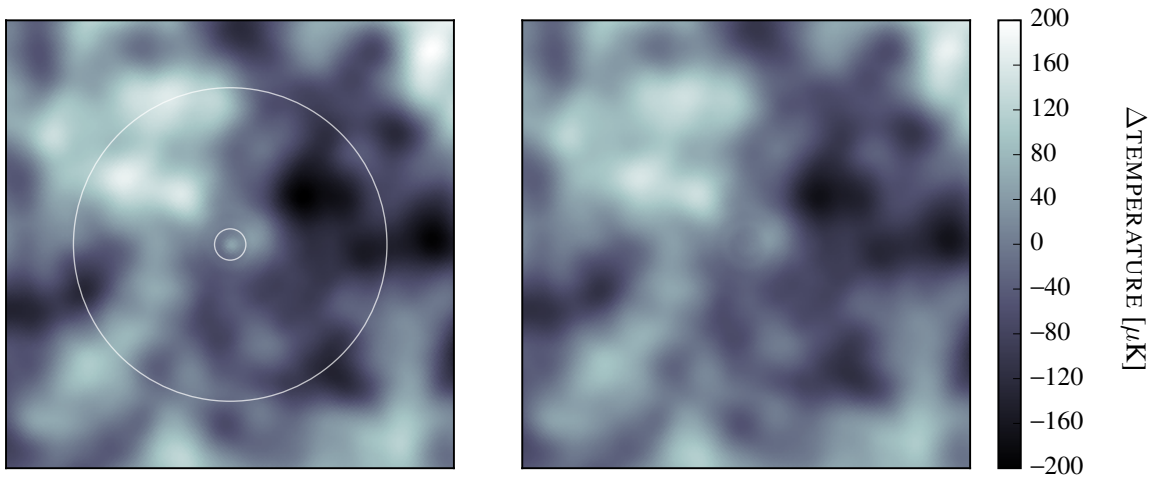

Figure 3.4 **Left:** map of the CMB temperature difference relative to the mean prior to inpainting applied. The point source is located at the centre of the image. The inner $R = 2'$ circle shows the region to be inpainted and the region between the inner and outer circles is the area used to estimate the inpainting values. **Right:** inpainted CMB temperature map.

3.3). Various choices of these cuts are discussed in section 5.5.2.2.

3.4.5 Faint Point Source Inpainting

In addition to the bright sources and galaxy clusters masked in section 3.4.2, the combined SPT-SZ +*Planck* temperature map also contains point sources with flux densities between $6.4 < F_{150} < 50$ mJy. These point sources are painted over in the combined map using the constrained Gaussian inpainting method (Hoffman & Ribak, 1991; Benoit-Lévy et al., 2013). The pixel values of the region to be inpainted are estimated using the fiducial lensed CMB correlation function and the pixel values of the surrounding region:

$$T_i^{\rm obs} = T_i^{\rm sim} + \Xi_{ij}\Xi_{jj}^{-1}(T_j^{\rm obs} - T_j^{\rm sim}), \tag{3.8}$$

where $T^{\rm obs}$, $T^{\rm sim}$ are the data and simulated CMB map generated from the fiducial temperature power spectrum, the matrices Ξ_{ij} and Ξ_{jj} represent the cross-correlation between the region in-

side (denoted by subscript i) and outside the masked region (denoted by subscript j), and the auto-correlation of the outer region, respectively. The elements of these matrices are estimated using the correlation function calculated from a fiducial lensed CMB spectrum, using:

$$w_\theta^{TT} = \sum_\ell \frac{2\ell+1}{4\pi} C_{\ell,\mathrm{fid}}^{TT} P_\ell(\cos(\theta)). \tag{3.9}$$

We inpaint regions within $R = 2'$ centred at the point sources using the pixel values in the region of $2' < R < 20'$. We have evaluated the validity of this method by applying this procedure on a simulated map without point sources, and obtained a difference of $\ll 1\%$ in power relative to the map without inpainting. Finally, the Gaussian beam $b_\ell^{1.75'}$ convolved in section 3.4.3 is deconvolved from the maps.

The outcome of combining the SPT-SZ 150 GHz and *Planck* 143 GHz temperature maps is shown in Figure 3.5 and the benefit of the combining process is visually apparent. In position-space, and limiting to $\ell_{\mathrm{max}} = 2000$, the combined map resembles the *Planck* only map since the modes at the largest scales stand out visually. Extending to $\ell_{\mathrm{max}} = 6000$ (4000 for *Planck*), the *Planck* map becomes dominated by noise, whereas the SPT-SZ + *Planck* map resembles the input CMB fluctuations. In contrast, the input CMB and the SPT-SZ maps appear different due the missing low-ℓ modes removed in the filtering, and it is evident that these modes are recovered by combining with *Planck*. In the next chapter, the quadratic estimator will be used to estimate the lensing potential from the combined SPT-SZ + *Planck* temperature map.

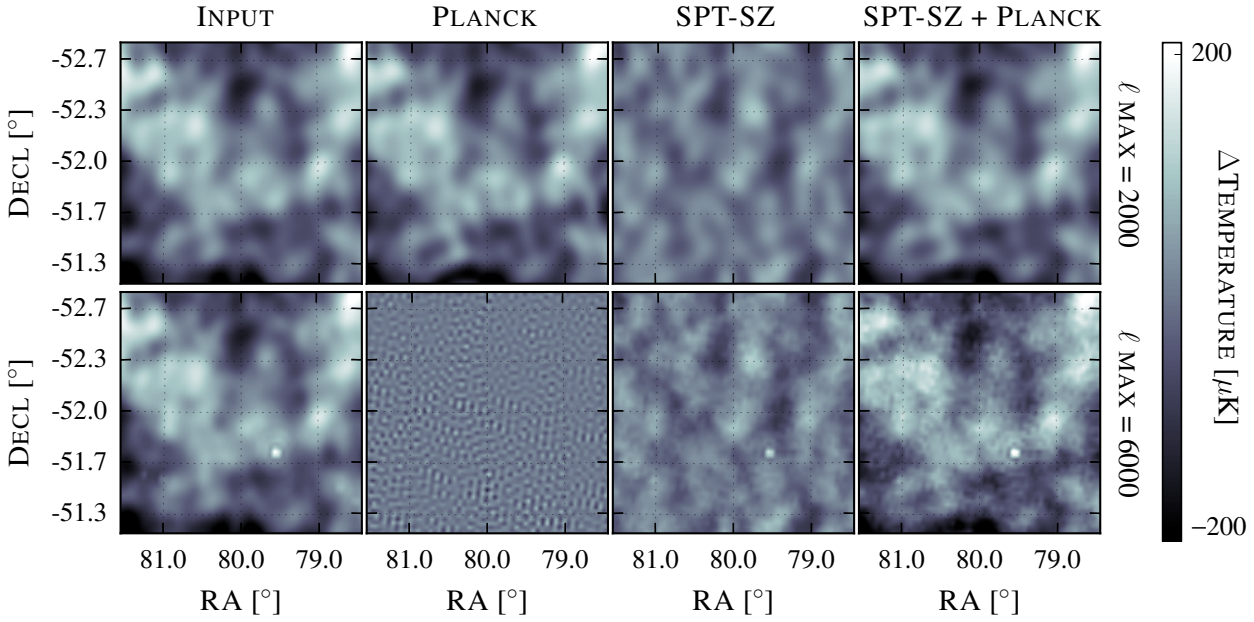

Figure 3.5 **Upper panels:** simulated CMB temperature maps for the input, *Planck*, SPT-SZ and SPT-SZ + *Planck* using multipoles up to $\ell = 2000$. **Lower panels:** same as above, but going to $\ell = 6000$ (except for *Planck*, which is cut off at $\ell = 4000$). For *Planck* and SPT-SZ maps, the beams have been deconvolved and re-convolved with a FWHM $= 1.75'$ Gaussian beam to match the resolution of the SPT-SZ + *Planck* map. A point source that is not visible with $\ell_{\rm max} = 2000$ becomes visible using $\ell_{\rm max} = 6000$. Since the noise coming from modes $\ell > 2000$ dominates over the signal for *Planck* when using $\ell_{\rm max} = 4000$, the second panel in the bottom row is mostly noise.

4

CMB Lensing Map Reconstruction

In this chapter, we first outline the mathematical background of CMB weak lensing. We then describe the methods used to reconstruct the lensing potential ϕ from a temperature map, and the output lensing map is presented as the main result.

4.1 Quadratic Estimator

The stretching and distortion of the CMB image is due to deflections of photon paths by the underlying potential. Mathematically, this could be written as (Lewis & Challinor, 2006; Hanson et al., 2010):

$$T^{\rm len}(\hat{\boldsymbol{n}}) = T^{\rm unl}[\hat{\boldsymbol{n}} + \nabla_i \phi(\hat{\boldsymbol{n}}) + \epsilon_j{}^k \nabla_k \psi(\hat{\boldsymbol{n}})], \tag{4.1}$$

where the first term is the unlensed temperature field, the second and third terms are the deflection field decomposed into the gradient and curl* components (Hirata & Seljak, 2003). The curl

*The word curl is often used to describe this component but is rather a gradient rotated by 90 degrees.

term $\epsilon_j{}^k \nabla_k \psi(\hat{\boldsymbol{n}})$, to first order, is not expected (Namikawa et al., 2012). Although there exist mechanisms such as gravitational waves (Cooray et al., 2005) that will generate such a mode, the amplitude is expected to be comparatively small and can be neglected. Therefore, the presence of curl modes is an indication of systematic errors introduced in the lensing reconstruction process, and can be used as a null test.

With the curl component neglected, we can perform a Taylor expansion on equation 4.1 to obtain:

$$T^{\rm len}(\hat{\boldsymbol{n}}) = T^{\rm unl}(\hat{\boldsymbol{n}}) + \nabla_i \phi(\hat{\boldsymbol{n}}) \nabla^i T^{\rm unl}(\hat{\boldsymbol{n}}) \tag{4.2}$$

to first order in $\nabla\phi(\hat{\boldsymbol{n}})$. Taking the spherical harmonic transform of both sides:

$$\begin{aligned} T^{\rm len}_{\ell_1 m_1} &= T^{\rm unl}_{\ell_1 m_1} + \int d\hat{\boldsymbol{n}} Y^*_{\ell_1 m_1}(\hat{\boldsymbol{n}}) \left[\nabla_i \sum_{LM} \phi_{LM} Y_{LM}(\hat{\boldsymbol{n}})\right] \left[\nabla^i \sum_{\ell'_1 m'_1} T^{\rm unl}_{\ell'_1 m'_1} Y_{\ell'_1 m'_1}(\hat{\boldsymbol{n}})\right] \\ &= T^{\rm unl}_{\ell_1 m_1} + \sum_{LM} \sum_{\ell'_1 m'_1} \phi_{LM} T^{\rm unl}_{\ell'_1 m'_1} \int d\hat{\boldsymbol{n}} Y^*_{\ell_1 m_1}(\hat{\boldsymbol{n}}) [\nabla_i Y_{LM}(\hat{\boldsymbol{n}})][\nabla^i Y_{\ell'_1 m'_1}(\hat{\boldsymbol{n}})]. \end{aligned} \tag{4.3}$$

Now taking $T^{\rm len}_{\ell_1 m_1} T^{\rm len}_{\ell_2 m_2}$ (again to first order in ϕ):

$$\begin{aligned} T^{\rm len}_{\ell_1 m_1} T^{\rm len}_{\ell_2 m_2} = T^{\rm unl}_{\ell_1 m_1} T^{\rm unl}_{\ell_2 m_2} &+ \sum_{LM} \sum_{\ell'_2 m'_2} \phi_{LM} T^{\rm unl}_{\ell_1 m_1} T^{\rm unl}_{\ell'_2 m'_2} \int d\hat{\boldsymbol{n}} Y^*_{\ell_2 m_2}(\hat{\boldsymbol{n}}) [\nabla_i Y_{LM}(\hat{\boldsymbol{n}})][\nabla^i Y_{\ell'_2 m'_2}(\hat{\boldsymbol{n}})] \\ &+ \sum_{LM} \sum_{\ell'_1 m'_1} \phi_{LM} T^{\rm unl}_{\ell_2 m_2} T^{\rm unl}_{\ell'_1 m'_1} \int d\hat{\boldsymbol{n}} Y^*_{\ell_1 m_1}(\hat{\boldsymbol{n}}) [\nabla_i Y_{LM}(\hat{\boldsymbol{n}})][\nabla^i Y_{\ell'_1 m'_1}(\hat{\boldsymbol{n}})]. \end{aligned} \tag{4.4}$$

Using $T^{\rm unl}_{\ell_1 m_1} = (-1)^{m_1} (T^{\rm unl}_{\ell_1 - m_1})^*$, and taking the average over many CMB realizations:

$\langle (T^{\rm unl}_{\ell_1 -m_1})^* T^{\rm unl}_{\ell'_2 m'_2}\rangle = C^{TT,{\rm unl}}_{\ell_1}\delta_{\ell_1\ell'_2}\delta_{-m_1 m'_2}$ and $\langle (T^{\rm unl}_{\ell_2 -m_2})^* T^{\rm unl}_{\ell'_1 m'_1}\rangle = C^{TT,{\rm unl}}_{\ell_2}\delta_{\ell_2\ell'_1}\delta_{-m_2 m'_1}$ we obtain:

$$\begin{aligned}\langle T^{\rm len}_{\ell_1 m_1} T^{\rm len}_{\ell_2 m_2}\rangle_{\rm CMB} =&(-1)^{m_2} C^{TT,{\rm unl}}_{\ell_2}\delta_{\ell_2\ell_1}\delta_{-m_2 m_1}\\ &+\sum_{LM}\sum_{\ell'_2 m'_2}\phi_{LM}(-1)^{m_1} C^{TT,{\rm unl}}_{\ell_1}\delta_{\ell_1\ell'_2}\delta_{-m_1 m'_2}\int d\hat{\boldsymbol{n}} Y^*_{\ell_2 m_2}(\hat{\boldsymbol{n}})[\nabla_i Y_{LM}(\hat{\boldsymbol{n}})][\nabla^i Y_{\ell'_2 m'_2}(\hat{\boldsymbol{n}})]\\ &+\sum_{LM}\sum_{\ell'_1 m'_1}\phi_{LM}(-1)^{m_2} C^{TT,{\rm unl}}_{\ell_2}\delta_{\ell_2\ell'_1}\delta_{-m_2 m'_1}\int d\hat{\boldsymbol{n}} Y^*_{\ell_1 m_1}(\hat{\boldsymbol{n}})[\nabla_i Y_{LM}(\hat{\boldsymbol{n}})][\nabla^i Y_{\ell'_1 m'_1}(\hat{\boldsymbol{n}})],\end{aligned} \tag{4.5}$$

which gives us:

$$\begin{aligned}\langle T^{\rm len}_{\ell_1 m_1} T^{\rm len}_{\ell_2 m_2}\rangle_{\rm CMB} =&(-1)^{m_2} C^{TT,{\rm unl}}_{\ell_2}\delta_{\ell_2\ell_1}\delta_{-m_2 m_1}\\ &+\sum_{LM}\phi_{LM}(-1)^{m_1} C^{TT,{\rm unl}}_{\ell_1}\int d\hat{\boldsymbol{n}} Y^*_{\ell_2 m_2}(\hat{\boldsymbol{n}})[\nabla_i Y_{LM}(\hat{\boldsymbol{n}})][\nabla^i Y_{\ell_1 -m_1}(\hat{\boldsymbol{n}})]\\ &+\sum_{LM}\phi_{LM}(-1)^{m_2} C^{TT,{\rm unl}}_{\ell_2}\int d\hat{\boldsymbol{n}} Y^*_{\ell_1 m_1}(\hat{\boldsymbol{n}})[\nabla_i Y_{LM}(\hat{\boldsymbol{n}})][\nabla^i Y_{\ell_2 -m_2}(\hat{\boldsymbol{n}})].\end{aligned} \tag{4.6}$$

The term in the integral can be rewritten using the identity $\nabla^2 Y_{\ell m}(\hat{\boldsymbol{n}}) = -\ell(\ell+1)Y_{\ell m}(\hat{\boldsymbol{n}})$ (Hu, 2000), such that:

$$\int d\hat{\boldsymbol{n}} Y^*_{\ell m}(\hat{\boldsymbol{n}})\nabla_i Y_{LM}(\hat{\boldsymbol{n}})\nabla^i Y_{\ell' m'}(\hat{\boldsymbol{n}}) = \frac{1}{2}[L(L+1)+\ell'(\ell'+1)-\ell(\ell+1)]\int d\hat{\boldsymbol{n}} Y^*_{\ell m}(\hat{\boldsymbol{n}}) Y_{LM}(\hat{\boldsymbol{n}}) Y_{\ell' m'}(\hat{\boldsymbol{n}}), \tag{4.7}$$

and the integral of three spherical harmonics could be rewritten using the Wigner-3j symbol:

$$\int d\hat{\boldsymbol{n}} Y^*_{\ell m}(\hat{\boldsymbol{n}}) Y_{LM}(\hat{\boldsymbol{n}}) Y_{\ell' m'}(\hat{\boldsymbol{n}}) = (-1)^m\sqrt{\frac{(2L+1)(2\ell+1)(2\ell'+1)}{4\pi}}\begin{pmatrix}\ell & L & \ell'\\ 0 & 0 & 0\end{pmatrix}\begin{pmatrix}\ell & L & \ell'\\ -m & M & m'\end{pmatrix} \tag{4.8}$$

and therefore:

$$\begin{aligned}\langle T^{\rm len}_{\ell_1 m_1} T^{\rm len}_{\ell_2 m_2}\rangle_{\rm CMB} =&(-1)^{m_2} C^{TT,{\rm unl}}_{\ell_2}\delta_{\ell_2\ell_1}\delta_{-m_2 m_1}\\ &+\sum_{LM}\phi_{LM}(-1)^{m_1+m_2}C^{TT,{\rm unl}}_{\ell_1}\frac{1}{2}[L(L+1)+\ell_1(\ell_1+1)-\ell_2(\ell_2+1)]\\ &\sqrt{\frac{(2L+1)(2\ell_1+1)(2\ell_2+1)}{4\pi}}\begin{pmatrix}\ell_2 & L & \ell_1\\ 0 & 0 & 0\end{pmatrix}\begin{pmatrix}\ell_2 & L & \ell_1\\ -m_2 & M & -m_1\end{pmatrix}\\ &+\sum_{LM}\phi_{LM}(-1)^{m_2+m_1}C^{TT,{\rm unl}}_{\ell_2}\frac{1}{2}[L(L+1)+\ell_2(\ell_2+1)-\ell_1(\ell_1+1)]\\ &\sqrt{\frac{(2L+1)(2\ell_1+1)(2\ell_2+1)}{4\pi}}\begin{pmatrix}\ell_1 & L & \ell_2\\ 0 & 0 & 0\end{pmatrix}\begin{pmatrix}\ell_1 & L & \ell_2\\ -m_1 & M & -m_2\end{pmatrix},\end{aligned}\tag{4.9}$$

which can be written as:

$$\begin{aligned}\langle T^{\rm len}_{\ell_1 m_1} T^{\rm len}_{\ell_2 m_2}\rangle_{\rm CMB} =&(-1)^{m_2} C^{TT,{\rm unl}}_{\ell_2}\delta_{\ell_2\ell_1}\delta_{-m_2 m_1}\\ &+\sum_{LM}\phi_{LM}(-1)^{M}C^{TT,{\rm unl}}_{\ell_1}F_{\ell_2 L\ell_1}\begin{pmatrix}\ell_1 & \ell_2 & L\\ m_1 & m_2 & -M\end{pmatrix}(-1)^{\ell_1+\ell_2+L}\\ &+\sum_{LM}\phi_{LM}(-1)^{M}C^{TT,{\rm unl}}_{\ell_2}F_{\ell_1 L\ell_2}\begin{pmatrix}\ell_1 & \ell_2 & L\\ m_1 & m_2 & -M\end{pmatrix},\end{aligned}\tag{4.10}$$

using the symmetry properties of Wigner-3j symbols (see Appendix A.2), and

$$F_{\ell_2 L\ell_1}=\frac{1}{2}[L(L+1)+\ell_1(\ell_1+1)-\ell_2(\ell_2+1)]\sqrt{\frac{(2L+1)(2\ell_1+1)(2\ell_2+1)}{4\pi}}\begin{pmatrix}\ell_2 & L & \ell_1\\ 0 & 0 & 0\end{pmatrix},\tag{4.11}$$

$$F_{\ell_1 L\ell_2}=\frac{1}{2}[L(L+1)+\ell_2(\ell_2+1)-\ell_1(\ell_1+1)]\sqrt{\frac{(2L+1)(2\ell_1+1)(2\ell_2+1)}{4\pi}}\begin{pmatrix}\ell_1 & L & \ell_2\\ 0 & 0 & 0\end{pmatrix}.\tag{4.12}$$

Furthermore, $\ell_1+\ell_2+L$ must be even since $\begin{pmatrix}\ell_2 & L & \ell_1\\ 0 & 0 & 0\end{pmatrix}=0$ otherwise (which is one of the

properties of the Wigner-3j symbol), and therefore:

$$\begin{aligned}\langle T^{\rm len}_{\ell_1 m_1} T^{\rm len}_{\ell_2 m_2}\rangle_{\rm CMB} =&(-1)^{m_2} C^{TT,{\rm unl}}_{\ell_2}\delta_{\ell_2\ell_1}\delta_{-m_2 m_1} \\ &+\sum_{LM}(-1)^M \begin{pmatrix} \ell_1 & \ell_2 & L \\ m_1 & m_2 & -M \end{pmatrix} [C^{TT,{\rm unl}}_{\ell_1} F_{\ell_2 L\ell_1} + C^{TT,{\rm unl}}_{\ell_2} F_{\ell_1 L\ell_2}]\phi_{LM} \\ =&(-1)^{m_2} C^{TT,{\rm unl}}_{\ell_2}\delta_{\ell_2\ell_1}\delta_{-m_2 m_1} + \sum_{LM}(-1)^M \begin{pmatrix} \ell_1 & \ell_2 & L \\ m_1 & m_2 & -M \end{pmatrix} W^{TT}_{\ell_1 L\ell_2}\phi_{LM}, \quad (4.13)\end{aligned}$$

where we have defined the weight function[†]:

$$W^{TT}_{\ell_1 L\ell_2} = [C^{TT,{\rm unl}}_{\ell_1} F_{\ell_2 L\ell_1} + C^{TT,{\rm unl}}_{\ell_2} F_{\ell_1 L\ell_2}]. \quad (4.14)$$

This states that for a fixed lensing potential ϕ and multiple realizations of the unlensed CMB, lensing generates correlations between previously uncorrelated modes, which introduces off-diagonal terms in the harmonic-space covariance of the CMB modes. In this framework, we can write a general form that links two temperature multipole moments and the lensing potential:

$$\hat{\phi}_{LM} = \hat{A}_{LM} \sum_{\ell_1 m_1 \ell_2 m_2} (-1)^M \begin{pmatrix} \ell_1 & \ell_2 & L \\ m_1 & m_2 & -M \end{pmatrix} g^{TT}_{\ell_1 L\ell_2} T_{\ell_1 m_1} T_{\ell_2 m_2}, \quad (4.15)$$

where $\hat{\phi}_{LM}$ represents the *estimated* lensing potential, $\hat{A}_{LM}$ is a normalization factor and $g^{TT}_{\ell_1 L\ell_2}$ is a weight function that correlates temperature modes ℓ_1,ℓ_2 and lensing mode L. Ideally, we would like to obtain $g^{TT}_{\ell_1 L\ell_2}$ that gives the minimum variance estimate of $\hat{\phi}_{LM}$. For isotropic noise, this has been derived in Okamoto & Hu 2003 and is given by:

$$g^{TT}_{\ell_1 L\ell_2} = \frac{W^{TT}_{\ell_1 L\ell_2}}{2C^{TT,{\rm len+noise}}_{\ell_1} C^{TT,{\rm len+noise}}_{\ell_2}}, \quad (4.16)$$

[†]This is for the particular case of using two temperature fields $T_{\ell_1 m_1}, T_{\ell_2 m_2}$, and is, in general, different for other combinations that include polarization. For such cases, see Okamoto & Hu 2003.

where $C_\ell^{TT,\mathrm{len+noise}} = C_\ell^{TT,\mathrm{len}} + N_\ell^{TT}$, with N_ℓ^{TT} the noise power spectrum. Therefore, the estimator that is at first order in ϕ, formally optimal, can be written as:

$$\bar{\phi} = \frac{\hat{\phi}_{LM}}{\hat{A}_{LM}} = \sum_{\ell_1 m_1 \ell_2 m_2} \frac{(-1)^M}{2} \begin{pmatrix} \ell_1 & \ell_2 & L \\ m_1 & m_2 & -M \end{pmatrix} W^{TT}_{\ell_1 L \ell_2} \bar{T}_{\ell_1 m_1} \bar{T}_{\ell_2 m_2}, \tag{4.17}$$

where $\bar{\phi}$ represents the *filtered* (or *unnormalized*) estimate of ϕ, and $\bar{T}_{\ell m}$=$T_{\ell m}/C_\ell^{TT,\mathrm{len+noise}} \equiv F_\ell T$[‡]. However, we modify the filtering slightly since the combined SPT-SZ +*Planck* temperature map has large variations across m for a given ℓ due to the SPT-SZ noise, which can be seen in Figure 3.3. Instead, we use a filter that is both ℓ and m dependent, constructed by taking the sum of the *lensed* CMB spectrum, foreground components[§], and noise:

$$F_{\ell m} = \frac{1}{|T_{\ell m,\mathrm{fid}}|^2 + \langle |T_{\ell m,\mathrm{foregrounds}}|^2 \rangle + \langle |T_{\ell m,\mathrm{noise}}|^2 \rangle}, \tag{4.18}$$

where $|T_{\ell m,\mathrm{fid}}|^2$ is an expansion of the fiducial CMB input spectrum, $\langle |T_{\ell m,\mathrm{foregrounds}}|^2 \rangle$ is the average foreground power measured from simulations and $\langle |T_{\ell m,\mathrm{noise}}|^2 \rangle$ is the average noise power. The purpose of this filtering process is to down-weight the contribution from noisy modes.

4.2 Reconstruction Process

We use the $T_{\ell m}$ of the optimally combined and inpainted SPT-SZ +*Planck* temperature map, and $\bar{\phi}$ is calculated using the Quicklens[¶] package written by D. Hanson, which is widely used for various lensing analyses. Naive brute-force calculation of Equation 4.17 requires $\mathcal{O}(\ell^4_{\mathrm{max}} L^2_{\mathrm{max}})$ operations (ℓ^4_{max} to loop over the ℓm grids for the two $T_{\ell m}$, and L^2_{max} to loop over the LM grid), which is a computationally heavy calculation. Quicklens instead calculates $W^{TT}_{\ell_1 L \ell_2}$ efficiently by exploiting the separability of the weight function and running the calculation in position-space

[‡]Equal value is assumed for all m for a given ℓ

[§]We assume the foregrounds to be *unlensed* in this study although the high redshift foregrounds such as the CIB are likely to be lensed by the low redshift large-scale structure. We will leave this consideration for future studies.

[¶]https://github.com/dhanson/quicklens

(see Appendix A.3 for the derivation).

To produce an unbiased estimate of the lensing potential $\hat{\phi}_{LM}$, one must subtract off the reconstruction artifacts known as the mean-field bias $\bar{\phi}^{\rm MF}_{LM}$ and normalize by the response function $\mathcal{R}^{\bar{\phi}\bar{\phi}}_{LM} = 1/\hat{A}_{LM}$

$$\hat{\phi}_{LM} = \frac{1}{\mathcal{R}^{\bar{\phi}\bar{\phi}}_{LM}}(\bar{\phi}_{LM} - \bar{\phi}^{\rm MF}_{LM}). \tag{4.19}$$

The mean-field bias originates from any experimental features and analysis steps that introduce statistical anisotropies (such as inhomogeneous noise and mode-coupling induced when a spherical harmonic transform is applied to a masked map). The mean-field for a specific realization is produced by first splitting the set of $\bar{\phi}_{LM}$ reconstructed from simulated temperature maps into two halves, and taking the average, omitting the realization that we are trying to calculate the mean-field bias for:

$$\bar{\phi}^{\rm MF,(1)}_{LM,i} = \frac{1}{(N/2-1)} \sum_{\substack{0<j<N/2 \\ i\neq j}} \bar{\phi}_{LM,j} \tag{4.20}$$

$$\bar{\phi}^{\rm MF,(2)}_{LM,i} = \frac{1}{(N/2-1)} \sum_{\substack{N/2<j<N \\ (i+N/2)\neq j}} \bar{\phi}_{LM,j}, \tag{4.21}$$

where N is the number of simulations used (198 in this case), and the $(i + N/2)$-th realization is omitted in (2) to match the number of realizations to calculate (1). The splitting of the mean-field step is to ensure that the auto-correlation of the mean-field bias is omitted in the lensing auto-spectrum calculation. The response function $\mathcal{R}^{\bar{\phi}\bar{\phi}}_{LM}$ is often assumed to be azimuthally symmetric and is only calculated as a function of L. In the presence of strong m-dependence in the noise (which is the case for SPT-SZ and hence SPT-SZ +*Planck* also), it is necessary to obtain the response function as a function of L and M (i.e. $\mathcal{R}^{\phi\phi}_{LM}$). We compute this using simulations, taking the ratio of the average cross-spectrum of output ($\bar{\phi}_{LM}$) and input (ϕ_{LM}) lensing poten-

tials to the average auto-spectrum of the input potentials:

$$\mathcal{R}^{\bar{\phi}\bar{\phi}(1,2)}_{LM,i} = \frac{\sum_{j\neq i}\phi_{LM,j}\bar{\phi}^*_{LM,j}}{\sum_{j\neq i}\phi_{LM,j}\phi^*_{LM,j}}, \tag{4.22}$$

where the summations run over $0 < j < N/2$, $j \neq i$ for calculating $\mathcal{R}^{\bar{\phi}\bar{\phi}(1)}_{LM,i}$ and $N/2 < j < N$, $j \neq i + N/2$ for $\mathcal{R}^{\bar{\phi}\bar{\phi}(2)}_{LM,i}$. However, the response function obtained this way is rather noisy. Therefore, we apply a scale dependent Gaussian smoothing in M, with smoothing scale $\lambda = L/20$. The ratio of the smoothed and an M-independent response function on an (L, M) grid is shown in Figure 4.1.

In summary, we first compute the unnormalized estimate of the lensing potential $\bar{\phi}$, normalize $\bar{\phi}$ using equation 4.19, apply factors of L using the definition $\hat{\kappa}_{LM} = -\frac{1}{2}L(L+1)\hat{\phi}_{LM}$ [‖], apply a spherical harmonic transform to convert $\hat{\kappa}_{LM}$ into a map $\hat{\kappa}(\hat{\boldsymbol{n}})$, and apply the final analysis

[‖]Such a conversion is often desirable in practice, since it makes the spectrum flatter, which makes mode-coupling due to masks less severe.

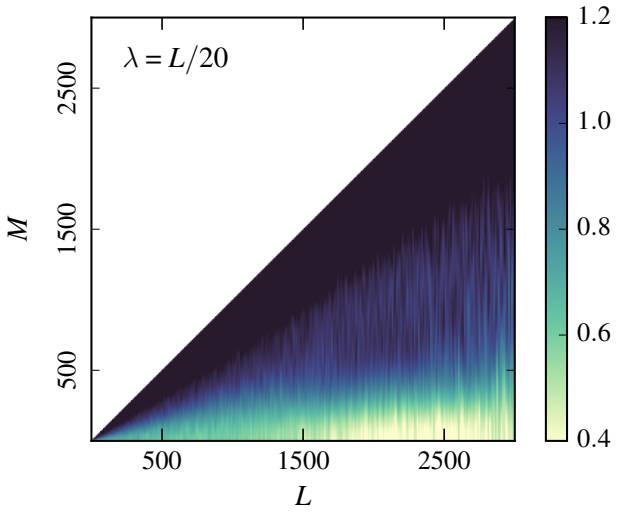

Figure 4.1 Ratio of the smoothed 2D response function with $\lambda = L/20$ against the M-averaged response function $\mathcal{R}^{\phi\phi}_{LM}/\mathcal{R}^{\phi\phi}_{L}$ presented on an (L, M) grid, where $\mathcal{R}^{\phi\phi}_{L} = \sum_M \langle \phi_{LM}\bar{\phi}^*_{LM}\rangle / \sum_M \langle \phi_{LM}\phi^*_{LM}\rangle$.

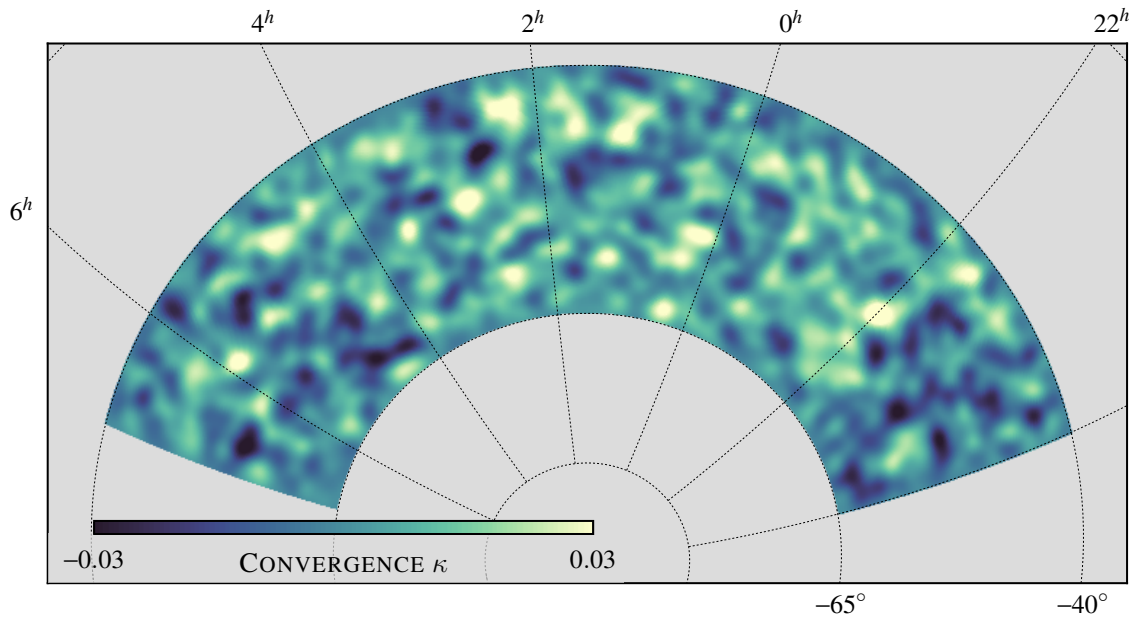

Figure 4.2 Reconstructed convergence map on a zenithal equal-area projection with a Gaussian FWHM=2° smoothing.

mask:

$$\widetilde{\phi}_{LM} = K^{-1} \int d\hat{\boldsymbol{n}} Y^*_{LM}(\hat{\boldsymbol{n}}) M(\hat{\boldsymbol{n}}) \left[\sum_{L'M'} Y_{L'M'}(\hat{\boldsymbol{n}}) K \hat{\phi}_{L'M'} \right] \tag{4.23}$$

where $K = -\frac{1}{2}L(L+1)$, and $M(\hat{\boldsymbol{n}})$ is the final analysis mask. The tilde on ϕ is used to denote that the final analysis mask has been applied. For our baseline analysis, the final mask removes circular patches of $R = 2'$ at the locations of point sources with flux density $6.4 < F_{150} < 50$ mJy, and $R = 5'$ at the locations of clusters between $4.5 < \mathrm{S/N}_{\mathrm{clus}} < 6$ in addition to the mask defined in Section 3.4.2.

The final lensing map produced using the methods outline in this chapter is shown in Figure 4.2. This lensing map is the largest lensing map yet produced using a high-resolution ground-based experiment—and with nearly 100% overlap with the Dark Energy Survey (Omori et al., 2017). The map will be used for cosmological parameter analysis (Simard et al. 2017, in preparation) and various cross-correlation analyses with DES, until the arrival of SPT-3G data.

5

Validation of The Lensing Map

In this chapter, the validity of the lensing map produced in Chapter 4 will be tested by measuring its auto-spectra and cross-spectra with external data sets. In Section 5.1, the method used to calculate the auto-spectra will be outlined first. Secondly, we will show the bandpowers of the mean auto-spectrum from the simulations and compare this with the theoretical input spectrum, which are expected to match for a valid reconstruction. Auto-spectrum of the data map calculated using the same pipeline will be shown next, and the amplitude will be compared against the theoretical prediction. In Sections 5.2 and 5.3, we also test whether the lensing map is properly correlated with galaxies and CIB in comparison to the *Planck* 2015 lensing map.

In producing auto- and cross-spectra, numerous analysis choices are made (e.g. mask, ℓ ranges, calibration factor), and these choices potentially introduce systematic errors in the lensing map. The degree of contamination is assessed by carrying out null tests, which are measurements that we expect to be consistent with zero for a map free of systematic errors (Section 5.5.1). We ad-

ditionally recalculate the auto- and cross-spectra by altering the analysis choices to test whether these impact the results (Section 5.5.2).

5.1 $\hat{C}_L^{\phi\phi}$ Auto-spectrum

5.1.1 Methods

The general auto-spectrum calculation is given by Equation 1.6. Here we calculate the auto-spectrum of the lensing map:

$$C_L^{\widetilde{\phi}\widetilde{\phi}} = \frac{1}{2L+1}\sum_{LM}(\widetilde{\phi}_{LM})^*\widetilde{\phi}_{LM}, \tag{5.1}$$

where tilde denotes ϕ with a final analysis masked applied. In this calculation, we are using two $\widetilde{\phi}_{LM}$, but each of these are produced from two temperature maps, and is therefore effectively correlating *four* temperature fields.

$C_L^{\widetilde{\phi}\widetilde{\phi}}$ calculated directly using Equation 5.1 is not equivalent to the true lensing spectrum $C_L^{\phi\phi}$ since it contains bias terms arising from correlations between the CMB and the lensing potentials. These are known as the $N^{(0)}$and $N^{(1)}$ biases, and are additional components which we subtract off from the measured raw spectrum (Hu & Okamoto, 2002; Kesden et al., 2003; Hanson et al., 2011):

$$\hat{C}_L^{\phi\phi} = C_L^{\widetilde{\phi}\widetilde{\phi}} - N_L^{(0)} - N_L^{(1)} + \cdots. \tag{5.2}$$

The superscripts (0), (1) denote the order at which the noise terms depend on the lensing potential power spectrum, and the relative amplitudes are shown in Figure 5.1. Higher-order terms in the equation above can be neglected under the assumption that the CMB and the lensing potential follow Gaussian statistics (Kesden et al., 2002).

The $N^{(0)}$ bias arises from chance correlations in the Gaussian CMB, foreground and noise (Story et al., 2015), and is present even in the absence of lensing (Cooray et al., 2008). It can

be calculated by[*]:

$$N_L^{(0)} = \left\langle C_L^{\widetilde{\phi}\widetilde{\phi}}[\widetilde{\phi}^{(1)}(\bar{S}_i^{\phi_1}\bar{S}_j^{\phi_2})\widetilde{\phi}^{(2)}(\bar{S}_i^{\phi_1}\bar{S}_j^{\phi_2})] + C_L^{\widetilde{\phi}\widetilde{\phi}}[\widetilde{\phi}^{(1)}(\bar{S}_i^{\phi_1}\bar{S}_j^{\phi_2})\widetilde{\phi}^{(2)}(\bar{S}_j^{\phi_2}\bar{S}_i^{\phi_1})]\right\rangle_{i,j}, \tag{5.3}$$

where $\bar{S}_i^{\phi_a}$ is the i-th simulated temperature map lensed with the potential ϕ_a and filtered using equation 4.18. i, j imply different CMB simulation realizations. Cross-correlation of two $\widetilde{\phi}_{LM}$ calculated using different mean-fields and response functions (denoted by the superscripts (1), (2)) are used to ensure that the auto-spectra of these components do not affect the resulting spectrum. The $N^{(0)}$ bias is calculated from 198 mock observed simulations that contain all the foreground components (point sources, Gaussian foregrounds and clusters).

Although simulations are produced to resemble the observed data as closely as possible, not all of the features are captured perfectly with the correct statistics due to our incomplete knowledge of the sky signal. Therefore, simply subtracting off Equation 5.3 (which is purely simulation based) from Equation 5.1 leads to a biased spectrum. The estimation of this $N^{(0)}$ bias in the data measurement can be improved by replacing one of the simulated temperature maps with data $\bar{D}$ to form a "realization dependent $N^{(0)}$" (Namikawa et al., 2013):

$$\begin{aligned} N_L^{(0),\mathrm{RD}} = \Big\langle & C_L^{\widetilde{\phi}\widetilde{\phi}}[\widetilde{\phi}^{(1)}(\bar{D}\bar{S}_i^{\phi_1})\widetilde{\phi}^{(2)}(\bar{D}\bar{S}_i^{\phi_1})] \\ & + C_L^{\widetilde{\phi}\widetilde{\phi}}[\widetilde{\phi}^{(1)}(\bar{S}_i^{\phi_1}\bar{D})\widetilde{\phi}^{(2)}(\bar{S}_i^{\phi_1}\bar{D})] \\ & + C_L^{\widetilde{\phi}\widetilde{\phi}}[\widetilde{\phi}^{(1)}(\bar{S}_i^{\phi_1}\bar{D})\widetilde{\phi}^{(2)}(\bar{D}\bar{S}_i^{\phi_1})] \\ & + C_L^{\widetilde{\phi}\widetilde{\phi}}[\widetilde{\phi}^{(1)}(\bar{D}\bar{S}_i^{\phi_1})\widetilde{\phi}^{(2)}(\bar{S}_i^{\phi_1}\bar{D})] \\ & - C_L^{\widetilde{\phi}\widetilde{\phi}}[\widetilde{\phi}^{(1)}(\bar{S}_i^{\phi_1}\bar{S}_j^{\phi_2})\widetilde{\phi}^{(2)}(\bar{S}_i^{\phi_1}\bar{S}_j^{\phi_2})] \\ & - C_L^{\widetilde{\phi}\widetilde{\phi}}[\widetilde{\phi}^{(1)}(\bar{S}_i^{\phi_1}\bar{S}_j^{\phi_2})\widetilde{\phi}^{(2)}(\bar{S}_j^{\phi_2}\bar{S}_i^{\phi_1})]\Big\rangle_{i,j}. \end{aligned} \tag{5.4}$$

Replacing $N^{(0)}$ with $N^{(0),\mathrm{RD}}$ has been shown to reduce the covariance Cov $\left(C_L^{\tilde{\phi}\tilde{\phi}}C_{L'}^{\tilde{\phi}\tilde{\phi}}\right)$ signifi-

[*]This is written in the most general form, and can be simplified to $N_L^{(0)}$=2×$\langle C_L^{\widetilde{\phi}\widetilde{\phi}}[\widetilde{\phi}^{(1)}(\bar{S}_i^{\phi_1}\bar{S}_j^{\phi_2})\widetilde{\phi}^{(2)}(\bar{S}_j^{\phi_2}\bar{S}_i^{\phi_1})]\rangle$ for the case of TT, but the simplification can not be made when using asymmetric pairs i.e. $T\dot{E}$, TB, $\dot{E}B$, where E and B are the E and B-mode polarizations.

cantly (Hanson et al., 2011).

The $N^{(1)}$ bias arises from the sensitivity of the four-point correlation (trispectrum) to angular scales that are not of interest for a given configuration (also known as secondary contractions (Kesden et al., 2003; Hanson et al., 2011; Planck Collaboration et al., 2014a)) and can be obtained numerically by using simulated temperature maps with different CMB realizations lensed by the same potential:

$$\begin{aligned} N_L^{(1)} = \Big\langle & C_L^{\widetilde{\phi}\widetilde{\phi}}[\widetilde{\phi}^{(1)}(\bar{S}_i^{\phi_1}\bar{S}_j^{\phi_1})\widetilde{\phi}^{(2)}(\bar{S}_i^{\phi_1}\bar{S}_j^{\phi_1})] \\ & + C_L^{\widetilde{\phi}\widetilde{\phi}}[\widetilde{\phi}^{(1)}(\bar{S}_i^{\phi_1}\bar{S}_j^{\phi_1})\widetilde{\phi}^{(2)}(\bar{S}_j^{\phi_1}\bar{S}_i^{\phi_1})] \\ & - C_L^{\widetilde{\phi}\widetilde{\phi}}[\widetilde{\phi}^{(1)}(\bar{S}_i^{\phi_1}\bar{S}_j^{\phi_2})\widetilde{\phi}^{(2)}(\bar{S}_i^{\phi_1}\bar{S}_j^{\phi_2})] \\ & - C_L^{\widetilde{\phi}\widetilde{\phi}}[\widetilde{\phi}^{(1)}(\bar{S}_i^{\phi_1}\bar{S}_j^{\phi_2})\widetilde{\phi}^{(2)}(\bar{S}_j^{\phi_2}\bar{S}_i^{\phi_1})]\Big\rangle_{i,j}. \end{aligned} \tag{5.5}$$

To accelerate the calculation for the $N^{(1)}$ bias, we use simulations that contain the lensed CMB only.

5.1.2 Results

The measured mean $N^{(0)}$ and $N^{(1)}$ bias subtracted auto-spectrum calculated from simulation realizations is shown in Figure 5.1 to demonstrate that our lensing reconstruction pipeline recovers the input lensing signal starting from lensed CMB maps.

In Figure 5.2, we show the auto-spectra of $\hat{\phi}$ maps reconstructed from SPT-SZ + *Planck* and SPT-SZ only temperature maps. The $\hat{C}_L^{\phi\phi}$ from *Planck* 2015 (Planck Collaboration XV., 2015) is also shown for reference. Band powers in the range of $50 < L < 3000$ are binned logarithmically using 20 bins, and the variance is calculated using the 198 simulation realizations. While the points above $L > 2000$ are likely to be affected by non-Gaussian foreground sources such as the CIB and tSZ from galaxies and low-mass galaxy clusters, the full L range up to $L = 3000$ is shown here for completeness to illustrate the raw spectrum of the lensing map itself. The ratio of the mean-field power and input spectrum is approximately unity at $L = 50$. To ensure that the

mean-field bias is not affecting our analysis, no modes below $L = 50$ are considered. The name "baseline" is assigned to the SPT-SZ + *Planck* sample with $\ell_{\rm max} = 3000$, $\ell_{\rm min} = 100$, (ℓ, m) cut $= [2000, 250]$, clusters with $\mathrm{S/N}_{\rm clus} > 6$ masked, and point sources with $F_{150} > 6.4$ mJy masked prior to the lensing reconstruction process[†]. The "SPT-SZ only" sample is produced using the same masking scheme and calibration, but without the combining step with *Planck* and using $\ell_{\rm min} = 550$ and $m > 250$.

We compare the mean simulated baseline, data baseline, SPT-SZ only and *Planck* lensing auto-spectrum amplitudes relative to our fiducial model assuming diagonal covariance over the range of $50 < L < 3000$. For the simulated baseline, we obtain a best-fit amplitude of $\eta^{\phi\phi} = \hat{C}_L^{\phi\phi}/\hat{C}_{L,\rm fid}^{\phi\phi} = 1.012^{+0.004}_{-0.004}$ with $\chi^2/\nu = 11.9/19$. While the measured mean amplitude is 3σ away from the input value, this bias is smaller than the statistical uncertainty and we therefore treat

[†]In calculating the final spectrum, a stricter mask described in Section 4.2 is used.

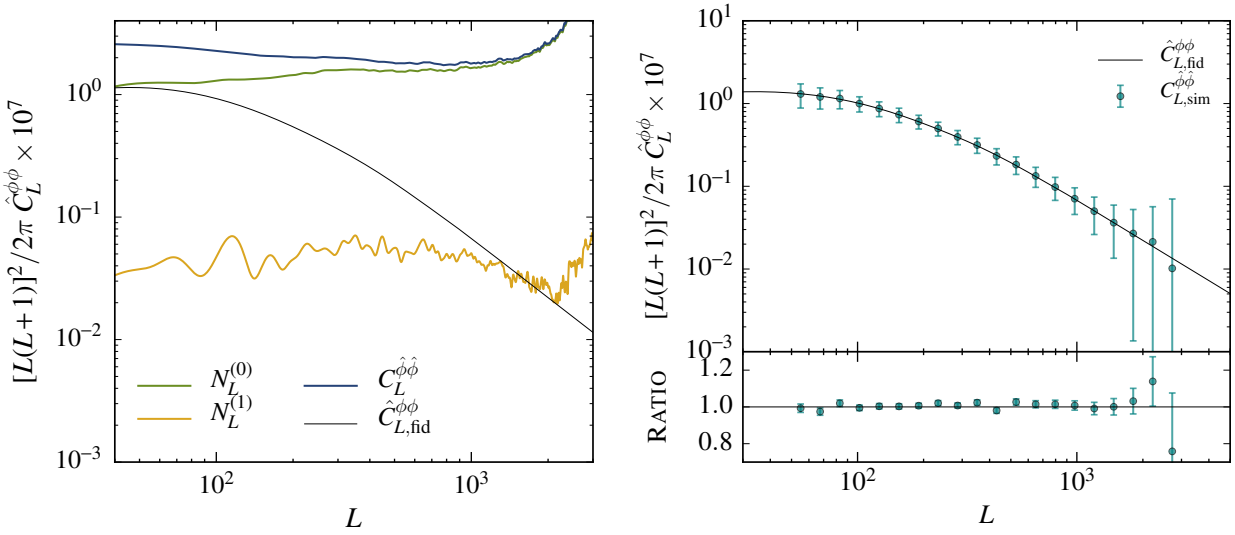

Figure 5.1 Results from simulations. **Left:** amplitudes of $C_L^{\hat{\phi}\hat{\phi}}$, $N_L^{(0)}$ and $N_L^{(1)}$ biases relative to the fiducial input $\hat{C}_{L,\rm fid}^{\phi\phi}$. **Right:** the mean debiased spectrum $\hat{C}_L^{\phi\phi}$=$C_L^{\tilde{\phi}\tilde{\phi}}-N_L^{(0)}-N_L^{(1)}$ calculated from 198 simulation realizations. Errors shown in the upper panel are calculated from 198 realizations, whereas in the lower panel the errors are $\sigma/\sqrt{198}$.

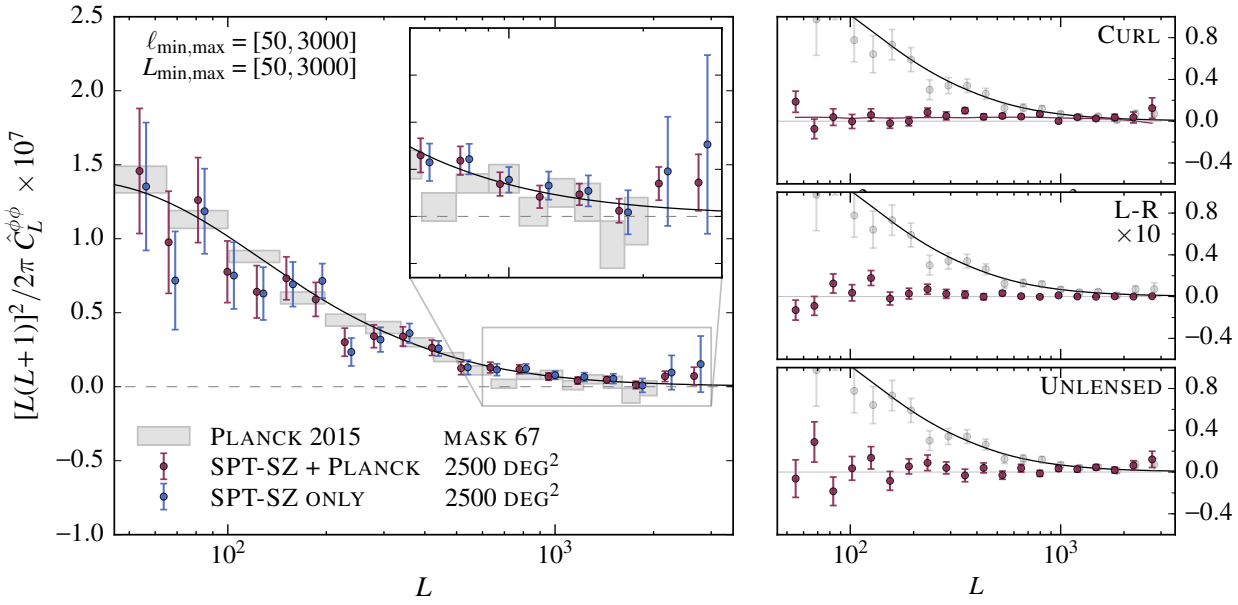

Figure 5.2 Plot showing the consistency between the measured lensing auto-spectrum and the fiducial spectrum, as well as the consistency of the curl, unlensed and L-R spectrum with respect to null. **Left:** $\hat{C}_L^{\phi\phi}$auto-spectrum for SPT-SZ +*Planck* (purple), SPT-SZ only (blue), *Planck* only using 67% of the sky (grey). The solid line is the fiducial $\hat{C}_L^{\phi\phi}$spectrum using a spatially flat ΛCDM *Planck* 2015 cosmology. **Upper right:** the $\hat{C}_L^{\psi\psi}$spectrum calculated from the map. The solid purple line represents the mean of the simulation realizations, which is used to calculate the χ^2 and PTE. **Centre right:** $\hat{C}_L^{\phi\phi}$spectrum from one L-R realization with the amplitude multiplied by a factor of 10. **Lower right:** $\hat{C}_L^{\phi\phi}$spectrum for one unlensed realization. These are similar to the plots published in Omori et al. 2017.

this difference as a systematic uncertainty in the calibration of the simulations[‡].

For the data baseline sample, we obtain a best-fit amplitude of $\eta^{\phi\phi} = 0.92^{+0.06}_{-0.06}(\text{Stat.})^{+0.01}_{-0.01}(\text{Sys.})$ with $\chi^2/\nu = 12.2/19$ (the χ^2/ν is calculated using the statistical uncertainties only). After removing the fractional lensing biases due to foregrounds, we obtain $\eta^{\phi\phi} = \hat{C}_L^{\phi\phi}/\hat{C}_{L,\text{fid}}^{\phi\phi} = 0.95^{+0.06}_{-0.06}(\text{Stat.})^{+0.02}_{-0.02}(\text{Sys.})$ with $\chi^2/\nu = 12.1/19$, where the goodness-of-fit is calculated using the statistical uncertainty only. Using the variance of unlensed simulations, we reject the null hypothesis of no lensing at $\sim 24\sigma$.

For SPT-SZ only, we obtain $\eta^{\phi\phi} = 0.91^{+0.06}_{-0.06}(\text{Stat.})^{+0.01}_{-0.01}(\text{Sys.})$ with $\chi^2/\nu = 16.3/19$ when foreground biases are neglected and $\eta^{\phi\phi} = 0.94^{+0.06}_{-0.06}(\text{Stat.})^{+0.02}_{-0.02}(\text{Sys.})$ with χ^2/ν of 16.2/19, when foreground biases are considered. In comparison, we obtain a best-fit amplitude of $\eta^{\phi\phi} = 0.98^{+0.02}_{-0.02}$ with χ^2/ν of 25.1/18 when *Planck* band powers over $\sim$ 67% of the sky presented in Planck Collaboration XV. 2015 are fit to our fiducial model. The *Planck* lensing map is less affected by foreground biases since (i) it is constructed from foreground-cleaned maps, (ii) it utilizes polarization maps that are less prone to contamination, and (iii) the lower resolution and higher noise level reduce the contribution from small scales where foregrounds have the largest effect.

We find that the SPT-SZ + *Planck* and SPT-SZ only measurements are consistent with each other and with *Planck* over $\sim$ 67% of the sky to within 0.5σ. All the results reported here are summarized in Tables 5.1 and 5.2.

5.2 $\hat{C}_L^{\phi\delta_g}$ Cross-spectrum

5.2.1 Data

One of the scientific uses of the SPT-SZ + *Planck* lensing map is for cross-correlations with external data sets. We calculate the cross-spectrum with the publicly available[§] all-sky *WISE* catalogue (Wright et al., 2010). The *WISE* survey mapped the sky at four wavelengths 3.4, 4.6, 12, and 22 μm ($W1$, $W2$, $W3$, $W4$) with an angular resolution of 6.1, 6.4, 6.5, and 12.0 arcseconds, respectively. We make one single cut in magnitude $15 < W1 < 17$ and remove all the flagged

[‡]In other lensing analyses this is bias is labelled as "MC correction" and is at most a 10% effect. Here, the correction is $\sim$1%.

[§]http://wise2.ipac.caltech.edu/docs/release/allsky/

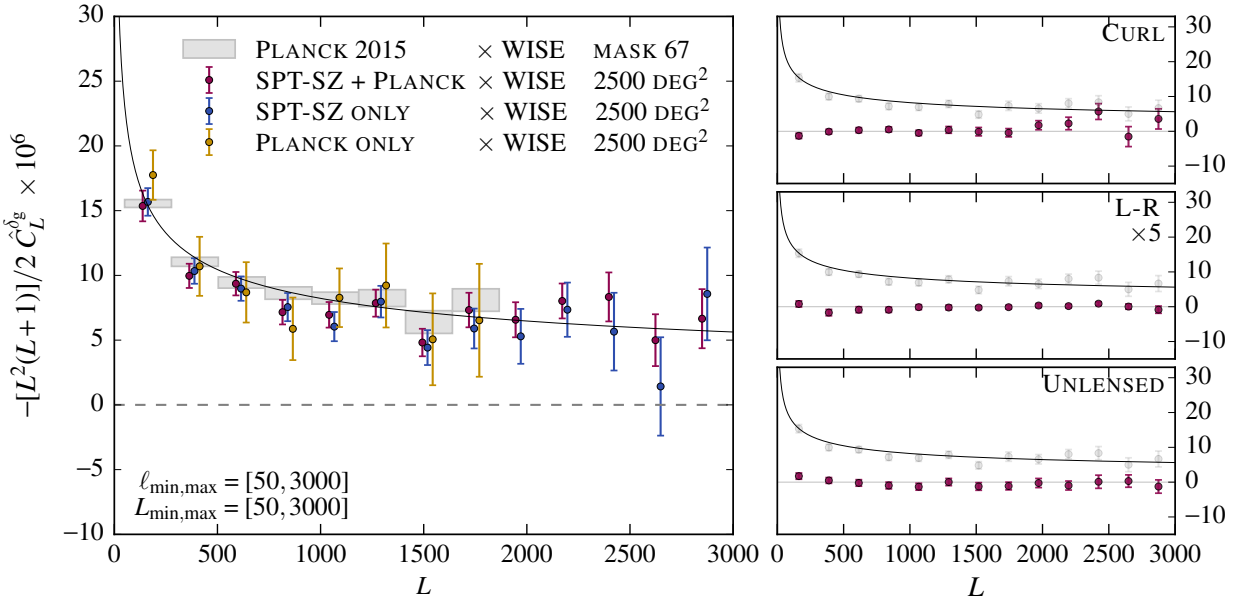

Figure 5.3 Plot showing the consistency between SPT-SZ + *Planck* and *Planck*-only lensing maps, by comparing the cross-correlations with *WISE* galaxies. Cross-correlations between *WISE* and curl, unlensed and L-R maps are also shown to be consistent with null. **Left:** cross-correlation between *WISE* and: SPT-SZ + *Planck* lensing map over 2500 deg^2 (purple), SPT-SZ only over 2500 deg^2 (blue), *Planck* 2015 over 2500 deg^2 (gold), and *Planck* 2015 over the 67% of the sky (grey boxes). **Right:** cross-correlation of the galaxy sample with **upper right:** the data curl-mode map, **centre right:** a single realization of a noise-only reconstructed map, **lower right:** a single realization of an unlensed map. In each of the panels, a power-law fit to the *Planck* result is shown.

sources. The sample contains 2×10^8 sources in total using the mask employed in the *Planck* lensing analysis, and 2×10^7 in sources in the nominal SPT region.

5.2.2 Methods

We make no attempt to estimate the redshift distribution of the galaxies, and hence a theoretical prediction of the cross-correlation amplitude is not computed. Instead, lensing maps reconstructed using various $\ell_{\rm min,max}$, (ℓ, m) cuts, masking, and calibrations are cross-correlated with the galaxies to probe the sensitivity of the reconstructed lensing map to these variations.

Starting with the *WISE* galaxy catalogue, we first project all the galaxies onto a HEALPix

map of $N_{\rm side} = 2048$, apply a simple binary mask (value=1 if there is at least one galaxy in the pixel, otherwise 0)[¶], and compute the mean number of galaxies $\langle n(\hat{\boldsymbol{n}})\rangle$. Using this, the overdensity map is calculated with:

$$\delta_{\rm g}(\hat{\boldsymbol{n}}) = \frac{n(\hat{\boldsymbol{n}}) - \langle n(\hat{\boldsymbol{n}})\rangle}{\langle n(\hat{\boldsymbol{n}})\rangle}. \tag{5.6}$$

We take a spherical harmonic transform of this map to obtain $\delta_{{\rm g},LM}$ and the cross-spectrum is calculated using:

$$\hat{C}_L^{\phi\delta_{\rm g}} = \frac{1}{2L+1}\sum_M (\phi_{LM})^* \delta_{{\rm g},LM}. \tag{5.7}$$

In practice, this is calculated using PolSpice[‖] (Szapudi et al., 2001; Chon et al., 2004), which deconvolves the mask effects from the calculated cross-spectrum $\hat{C}_L^{\phi\delta_{\rm g}}$. We derive the uncertainties by cross-correlating the *WISE* galaxy density map with the 198 simulated $\hat{\phi}$ maps and computing the variance for each bin. This method neglects the common sample variance between ϕ and $\delta_{\rm g}$. To assess the importance of this term, we compare this with errors obtained using the "block jackknife" method (see Section A.1) with 128 equal-area patches. We acquire similar results from this method and conclude that the original estimate is adequate.

5.2.3 Results

Cross-spectra between *WISE* galaxy density and the various $\hat{\phi}$ maps are shown in Figure 5.3. The CMB lensing maps used are: SPT-SZ + *Planck*, SPT-SZ only, *Planck*-only over 2500 deg^2, and *Planck*-only over 67% of the sky. We additionally overplot a power-law of the form $p_L = a(L/L_0)^{-b}$, with parameters $a = 2.15\times10^{-8}$, $b = 1.35$, $L_0 = 490$, which are obtained by performing a least-squares fit to the cross-spectrum between *Planck* and *WISE* over 67% of the sky in the range of $50 < L < 1864$. We then fit this power-law with an amplitude parameter $\eta^{\phi\delta_{\rm g}} = -L(L+1)/2 \times \hat{C}_L^{\phi\delta_{\rm g}}/p_L$ to the other cross-spectra. We obtain best-fit amplitudes of

[¶]Since this mask does not distinguish between the masked pixels and pixels with no galaxies, the mean is likely to be slightly overestimated. However, this shift is small since the mean number of galaxies per pixels is high (6.5 galaxies/pixel), and the pixels with zero galaxies is likely to be a masking effect, not physical.

[‖]http://www2.iap.fr/users/hivon/software/PolSpice

$\eta^{\phi\delta_g} = 0.94^{+0.04}_{-0.04}$ for SPT-SZ + *Planck*, $\eta^{\phi\delta_g} = 0.93^{+0.04}_{-0.04}$ for SPT-SZ only, $\eta^{\phi\delta_g} = 1.00^{+0.02}_{-0.01}$ for *Planck*-only over $\sim 67\%$ of the sky, and $\eta^{\phi\delta_g} = 1.02^{+0.08}_{-0.08}$ for *Planck*-only over 2500 deg^2. Therefore, while the *Planck* lensing map is exceptional for cross-correlations with galaxy surveys that extend beyond the SPT 2500 deg^2 footprint, a better signal-to-noise ratio is obtained using the SPT-SZ + *Planck* map for correlations within the SPT footprint. These results are summarized in Table 5.1.

Results	$\eta^{\phi\phi}$	χ^2 (PTE)	$\eta^{\phi\delta_g}$	χ^2 (PTE)
Baseline	$0.92^{+0.06}_{-0.06}$(Stat.)$^{+0.01}_{-0.01}$(Sys.)	12.2 (0.88)	$0.94^{+0.04}_{-0.04}$	12.0 (0.45)
SPT-SZ only	$0.91^{+0.06}_{-0.06}$(Stat.)$^{+0.01}_{-0.01}$(Sys.)	16.3 (0.63)	$0.93^{+0.04}_{-0.04}$	9.6 (0.65)
Planck-67%	$0.98^{+0.02}_{-0.02}$	25.1 (0.12)	$1.00^{+0.02}_{-0.01}$	6.1 (0.53)
(SPT patch)			$1.02^{+0.08}_{-0.08}$	3.8 (0.80)
Curl		23.4 (0.22)		15.6 (0.27)
L-R		28.6 (0.10)		11.1 (0.60)
Unlensed		18.9 (0.53)		10.3 (0.67)

Table 5.1 Table summarizing the fits to fiducial theory without foreground biases considered, and null tests fitted to zero.

Results	$\eta^{\phi\phi}$	χ^2 (PTE)
Baseline	$0.95^{+0.06}_{-0.06}$(Stat.)$^{+0.02}_{-0.02}$(Sys.)	12.1 (0.88)
SPT-SZ only	$0.94^{+0.06}_{-0.06}$(Stat.)$^{+0.02}_{-0.02}$(Sys.)	16.2 (0.64)

Table 5.2 Table summarizing the fits to fiducial theory with foreground biases considered.

5.3 Cross-correlation with the Cosmic Infrared Background

5.3.1 Data

We calculate the cross-correlation between the SPT-SZ + *Planck* lensing map and the 545 GHz channel from *Planck*[**], which traces the CIB emission (in addition to galactic thermal dust). The CIB mainly consists of dusty star forming galaxies at high redshifts ($1 < z < 3$). We expect a

[**] HFI_SkyMap_545_2048_R2.02_full.fits

strong correlation between CMB lensing and CIB since the signal from these probes peak at similar redshifts, and a 42σ detection has already been made by Planck Collaboration et al. 2014c by cross-correlating the CMB lensing map presented in Planck Collaboration et al. 2014a and the 545 GHz channel. We repeat this measurement using the SPT-SZ + *Planck* lensing map and verify that we obtain a consistent correlation amplitude.

In 2016, *Planck* released a CIB map produced by utilizing the generalized needlet internal linear combination (GNILC) technique. The algorithm uses spatial information to disentangle the emission from galactic thermal dust and the CIB (Planck Collaboration et al., 2016b). This map is used to estimate the residual contamination from the non-Gaussianity of the CIB emission in the SPT-SZ + *Planck* lensing map.

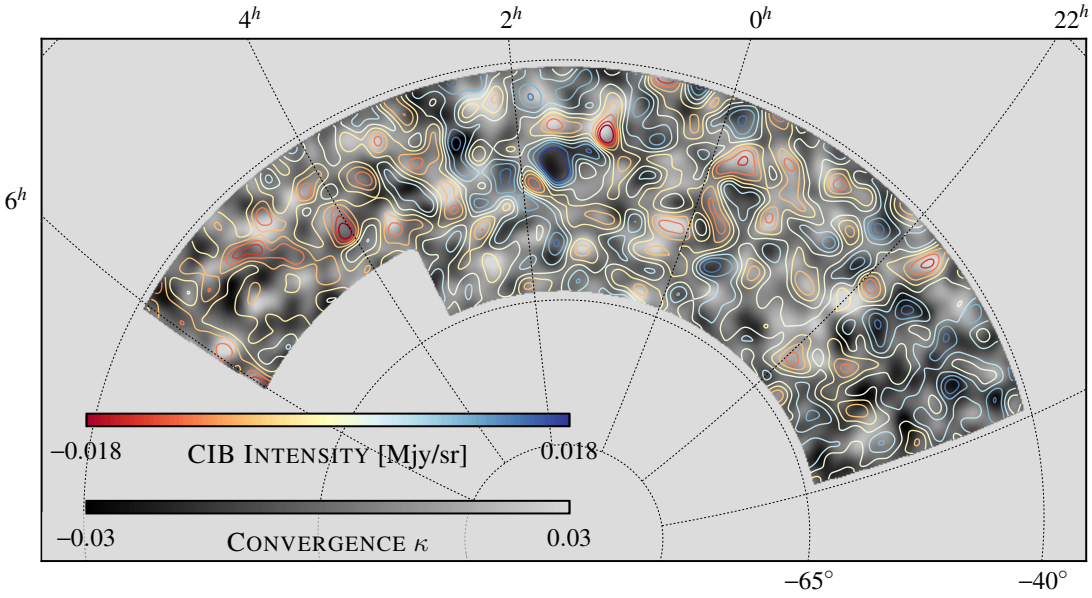

Figure 5.4 Contours of GNILC 545 GHz CIB map over the SPT-SZ + *Planck* convergence map smoothed with a FWHM=2° Gaussian beam. The lower left corner is masked additionally to remove the masked region in the GNILC map.

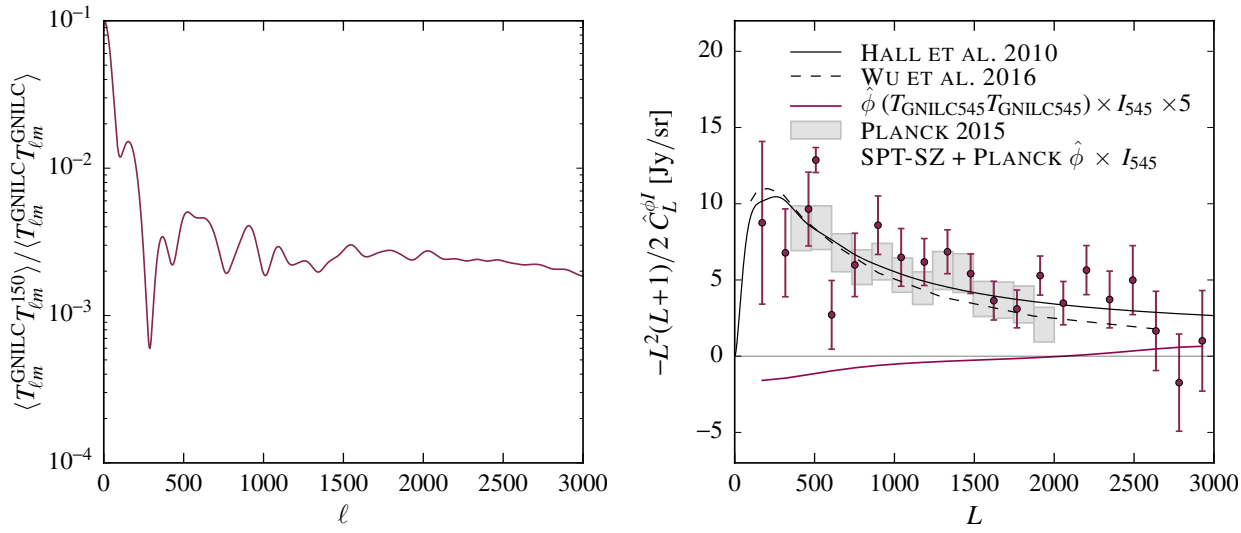

Figure 5.5 **Left:** ratio of the cross-correlation between the combined SPT-SZ +*Planck* temperature map × GNILC CIB 545 GHz map over the auto-spectrum of GNILC CIB 545 GHz map, which is the scaling to be applied to the GNILC CIB 545 GHz map. **Right:** correlation between the SPT-SZ +*Planck* lensing map and the *Planck* 545 GHz channel, which is predominantly composed of the CIB. We observe a strong correlation between $\hat{\phi}$ and the 545 GHz map that is consistent with a theoretical model constructed using a modified black body and employing a single spectral energy distribution model given in (Hall et al., 2010). The purple line corresponds to the $\hat{\phi}(T_{\rm GNILC150}, T_{\rm GNILC150}) \times I_{545}$ bispectrum calculated from the GNILC 545 GHz and *Planck* 545 GHz maps.

5.3.2 Methods

The cross-correlation between the SPT-SZ + *Planck* lensing map and *Planck* 545 GHz is calculated in a standard way by taking the angular power spectrum after deconvolving the beam from the *Planck* 545 GHz map.

To estimate the level of CIB contamination, we first calculate the cross-correlation between the SPT-SZ + *Planck* 150 GHz temperature and GNILC 545 GHz temperature maps[††]. The amplitude of this correlation indicates the amount of CIB emission in the 150 GHz data. The GNILC 545 GHz map is then multiplied by an ℓ dependent scaling function (shown in Figure 5.5), such

[††] http://irsa.ipac.caltech.edu/data/Planck/release_2/all-sky-maps/maps/component-maps/foregrounds/COM_CompMap_CIB-GNILC-F545_2048_R2.00.fits

that the CIB map matches in amplitude with the residual amplitude. The quadratic estimator technique is applied to this map to produce a $\hat{\phi}(T_{\rm GNILC150}, T_{\rm GNILC150})$ map, where the subscript GNILC150 denotes the residual GNILC 545 GHz emission at 150 GHz. The lensing map is reconstructed using the same masking and filtering as done in the making of $\hat{\phi}(T_{150}, T_{150})$, and this is cross-correlated with the *Planck* 545 GHz channel map.

5.3.3 Results

The two cross-correlations are shown in Figure 5.5, and the $\hat{\phi} \times$ CIB measurement made by *Planck* (Planck Collaboration et al., 2014c) is also presented as a reference. We observe a strong correlation between SPT-SZ + *Planck* lensing and the *Planck* 545 GHz maps that is consistent with a theoretical model constructed using a modified blackbody and employing a single spectral energy distribution model as demonstrated in (Planck Collaboration XV., 2015). The $\hat{\phi}(T_{\rm GNILC150}, T_{\rm GNILC150}) \times$ *Planck* 545 GHz correlation is found to be negative at angular multipoles $L < 2000$ and positive $L > 2000$, with a fractional amplitude ranging from 2% to 10% in the range of $50 < L < 3000$.

5.4 Gains from Adding Planck

By comparing the SPT-SZ + *Planck* and SPT-SZ only band powers shown in Figures 5.2 and 5.3, it can be seen that the signal in the combined map is dominantly from SPT-SZ. Nonetheless, the addition of *Planck* reduces the scatter for modes $L > 1500$. In particular, the scatter in the cross-correlation for the angular bin $2762 < L < 3000$ is reduced by a factor of ~ 2. Characterizing the lensing map at high L is important, especially for cross-correlation studies, since we could potentially probe astrophysical effects at these scales. The improvement is the result of additional mode pairs in the $\hat{\phi}$ reconstruction process; for a particular lensing mode of interest L, the number of temperature mode pairs ℓ_1, ℓ_2 that can be used increases[‡‡] and the statistical uncertainty

[‡‡]More specifically, the sum in Equation 4.17 is restricted by the selection rule $|\ell_1 - \ell_2| < L < \ell_1 + \ell_2$ of the Wigner-3j symbol. By introducing low-ℓ modes, the number of valid high-ℓ+low-ℓ mode pairs increases.

of a particular L mode is reduced.

5.5 Validations

The auto-spectrum of a map produced by passing an unlensed CMB temperature map through the lensing reconstruction process should be consistent with $\eta^{\phi\phi} = 0$. This could potentially fail if the reconstruction process creates spurious temperature correlations that lead to false lensing signals. We therefore apply lensing reconstruction on temperature maps that we expect to have zero signal (curl, unlensed, and L-R maps), and verify that the resulting spectra are consistent with the null hypothesis.

Additionally, we also probe the robustness of the map by varying ℓ, m cuts, masking, calibration, beams and the normalization method to verify that the map is insensitive to any processing choices that we make.

5.5.1 Null Tests

5.5.1.1 Curl

In estimating the lensing potential, we have so far used the gradient component as described in Equation 4.1. It is instead possible to estimate the contribution from the curl-mode lensing field $\hat{\psi}$, by exchanging the weight function with:

$$\begin{aligned} W^{\psi}_{\ell_1\ell_2 L} &= -\sqrt{\frac{(2\ell_1+1)(2\ell_2+1)(2L+1)}{4\pi}} \\ &\times C^{TT}_{\ell_1}\left(\frac{1-(-1)^{\ell_1+\ell_2+L}}{2}\right)\begin{pmatrix} \ell_1 & \ell_2 & L \\ 1 & 0 & -1 \end{pmatrix} \\ &\times \sqrt{L(L+1)\ell_1(\ell_1+1)} + (\ell_1 \leftrightarrow \ell_2). \end{aligned} \tag{5.8}$$

Systematic contaminations introduce non-Gaussianities in the CMB temperature maps, which get decomposed into gradient and curl components. Since we expect the amplitude of the curl modes to be small relative to the gradient mode for a systematics-free map, a significant detection of

it is an indication of a systematic bias. The $\hat{\psi}$ map is reconstructed using the same masking, filtering and response function as $\hat{\phi}$. The auto-spectrum is also calculated in a similar fashion by subtracting off $N_L^{(0),\mathrm{RD}}$ calculated from data and simulated $\hat{\psi}$ maps. As noted in Planck Collaboration XV. (2015); Kesden et al. (2003); van Engelen et al. (2012); Benoit-Lévy et al. (2013), the curl mode also includes a $N^{(1)}$ type bias. In our analysis, instead of removing this term, we compare with the mean curl-mode spectrum from the simulations, which includes the $N_L^{(1)}$ bias. From this, we obtain $\chi^2/\nu = 23.4/19$, giving a probability to exceed (PTE) of 0.22 for the null hypothesis of no contamination. From correlating the $\hat{\psi}$ map with the *WISE* galaxy sample, we obtain a correlation that is consistent with respect to null with $\chi^2 = 15.6$ for 13 degrees of freedom giving a PTE of 0.27. The results are shown in the upper right panels of both Figures 5.2 and 5.3.

5.5.1.2 L-R Reconstruction

Many potential sources of systematic contamination are coupled to the telescope scanning strategy. We perform a test of reconstructing ϕ from a noise map formed by differencing left-going (L) from right-going (R) scans. We first combine the SPT-SZ L-R map with a noise realization of *Planck* (since no L-R map exist for *Planck*). We then pass this combined map through the lensing pipeline using the same filtering and response function as the standard $\hat{\phi}$ reconstruction case. From this, we obtain a $\chi^2/\nu = 28.6/20$ for the auto, and 11.1/13 for the cross-spectrum giving a PTE of 0.10 and 0.60 respectively. The results are shown in the centre right panel of both Figures 5.2 and 5.3.

5.5.1.3 Unlensed Maps

Lensing reconstruction relies on the non-Gaussian statistical properties that lensing imprints on the observed CMB. In the absence of lensing, the reconstructed map will be purely noise, and therefore, should be consistent with zero-signal. We simply test this by (i) replacing the lensed CMB with an unlensed CMB, (ii) producing both SPT-SZ and *Planck* simulated skies, (iii) com-

bining SPT-SZ and *Planck*, (iv) running the lensing estimator in the same manner as a lensed realization, and (v) finally using the response function for the lensed case to produce a map. Since this makes use of simulations only, this is purely a test of the reconstruction pipeline. We compute both the auto and cross-spectrum with *WISE* using this map, and we see no evidence of inconsistency with respect to null. Measuring χ^2/ν, we obtain 18.9/20 for auto, and 10.33/13 for the cross-spectrum giving a PTE of 0.53 and 0.67 respectively. Maps reconstructed this way are used to calculate the significance of the no-lensing hypothesis, as well as estimating the lensing reconstruction noise, which is used for forecasting and covariance estimation. The results are shown in the lower right panel of both Figures 5.2 and 5.3.

5.5.2 Systematic Error Tests

In this section, we modify certain aspects of the lensing reconstruction pipeline to test for possible sources of systematic errors in the data. We quantify the effects by quoting the maximum deviation defined as $\max\{(\hat{C}_{L,\mathrm{modified}} - \hat{C}_{L,\mathrm{baseline}})/\sigma(\hat{C}_{L,\mathrm{baseline}})\}$ across all the bins in each systematics test relative to the statistical uncertainty. For auto-spectra, we additionally quantify the deviation of the systematically modified results from the baseline results by calculating the χ^2 and corresponding PTE relative to zero, which are summarized in Table 5.3. The same measurement is not carried out for cross-spectra since our method of cross-correlating the galaxy map with different $\hat{\phi}$ realizations under-estimates the variance in $(\hat{C}^{\phi\delta_\mathrm{g}}_{L,\mathrm{sim}} - \hat{C}^{\phi\delta_\mathrm{g}}_{L,\mathrm{sim,modified}})$, which are the error bars shown in Figure 5.7. Nonetheless, the goal of this section is to illustrate that systematic variations lead to small changes in the resulting map, in comparison to the statistical uncertainty.

5.5.2.1 ℓ_{max}, ℓ_{min} Cut

Although including temperature modes out to higher ℓ increases the total number of modes one can use in the lensing reconstruction, these modes are more likely to include contributions from extragalactic foregrounds (point sources, tSZ, CIB; see Figure 3.1). We therefore apply a cut-off

in the maximum ℓ used, to minimize the bias in the lensing map.

As described in Section 5.1.2, we use the ℓ range of $50 < \ell < 3000$ in our baseline analysis. Two alternative cuts at $\ell_{\rm max} = 2500$ and 3500 are also made to verify that the maps we obtain are not highly contaminated by foregrounds. We observe that changing $\ell_{\rm max}$ does affect the scatter, and the biggest change in any bin is seen when $\ell_{\rm max}$ is reduced to 2500 (maximum deviation of 1.4σ for the auto and 2.1σ for the cross). When varying $\ell_{\rm min}$ from 100 to 50, we see negligible shifts (maximum deviation of 0.027σ for $\hat{C}_L^{\phi\phi}$ and 0.10σ for $\hat{C}_L^{\phi\delta_{\rm g}}$). The results are shown in the first panel of both Figures 5.6 and 5.7.

5.5.2.2 ℓ, m Cuts

High ℓ, low m modes of the combined temperature map are dominated by noise since both SPT-SZ and *Planck* are noisy for those modes. To remove the high noise modes, we apply cuts on the (ℓ, m) grid, and test the sensitivity of the reconstructed $\hat{\phi}$ map to this adopted cut. In calculating $\hat{C}_L^{\phi\phi}$, we calculate all the bias terms including $N_L^{(1)}$, using the same (ℓ, m) cuts. We test three cuts: (i) $\ell > 2000$ *and* $m < 350$, (ii) $\ell > 1200$ *and* $m < 350$ and (iii) $\ell > 2200$ *and* $m < 150$. The comparison between the baseline sample and (i) demonstrates whether we are including excessive noise from SPT-SZ at low m. (ii) is a conservative cut in ℓ, m, effectively removing noisy modes from *both* SPT-SZ and *Planck*. (iii) is the least conservative cut extending to higher ℓ and lower m. It should be noted that including slightly noisier temperature modes does not necessarily translate to noise bias since the filtering downweights these modes. Sample (ii) shows the biggest deviation from the baseline sample with 0.82σ in $\hat{C}_L^{\phi\phi}$ and 0.83σ in $\hat{C}_L^{\phi\delta_{\rm g}}$. The results are shown in the second panel of both Figures 5.6 and 5.7.

5.5.2.3 Cluster Masking

One of the main concerns of temperature-based single-frequency lensing reconstruction is the contamination from the tSZ effect produced by clusters and galaxies. $\hat{\phi}$ maps reconstructed using temperature maps that contain tSZ power will be biased. The measured $\hat{C}_L^{\phi\phi}$ will include

terms proportional to the tSZ 4-point function $\phi(T_{\rm tSZ}T_{\rm tSZ}) \times \phi(T_{\rm tSZ}T_{\rm tSZ})$ and the $\phi-$tSZ correlation $\phi(T_{\rm CMB}T_{\rm CMB}) \times \phi(T_{\rm tSZ}T_{\rm tSZ})$ (van Engelen et al., 2014). This bias will also result in a $\phi(T_{\rm tSZ}T_{\rm tSZ}) \times \delta_{\rm g}$ bispectrum when calculating cross-spectra with galaxies. These biases are dominantly due to the massive clusters, which we mask in our analysis. We vary the masking radii and cluster selection to investigate the optimal masking to mitigate the contamination, while minimizing the sky area lost by the masking.

We make variations in the radius used to mask the locations of clusters in the reconstructed $\hat{\phi}$ map. We tested using masks of larger radii for clusters with $\mathrm{S/N}_{\rm clus} > 6$ and $4.5 < \mathrm{S/N}_{\rm clus} < 6$, using $R_{\mathrm{S/N}_{\rm clus}>6} = 10', 15'$ and $R_{4.5<\mathrm{S/N}_{\rm clus}<6} = 5', 10'$. We found a maximum difference of only ~ 0.5 and $\sim 0.7\sigma$ discrepancies between our baseline auto and cross-spectrum respectively.

For the "baseline" sample, we mask clusters listed in Bleem et al. (2015) with $\mathrm{S/N}_{\rm clus} > 6$ prior to running the quadratic estimator, and mask down further to $\mathrm{S/N}_{\rm clus} > 4.5$ when calculating $\hat{C}_L^{\phi\phi}$ and $\hat{C}_L^{\phi\delta_{\rm g}}$. Tests in reconstructing $\hat{\phi}$ maps with less strict cuts using $\mathrm{S/N}_{\rm clus} = 10,\ 20$ are also made, and the results show that the $\hat{C}_L^{\phi\phi}$ amplitude for both cases are consistent with the $\mathrm{S/N} > 6$ cut sample with a maximum difference of 0.56σ for $\hat{C}_L^{\phi\phi}$ and 0.56σ for $\hat{C}_L^{\phi\delta_{\rm g}}$. In calculating these spectra, a common mask that removes clusters above $\mathrm{S/N}_{\rm clus} > 4.5$ is applied to all maps. This test illustrates the amount of tSZ power that gets spread out to the unmasked regions during the reconstruction process. The results are shown in the fourth panel of both Figures 5.6 and 5.7.

5.5.2.4 Response Function Smoothing

Due to the large scatter at high L, the response function is smoothed to prevent the scatter appearing in $\hat{C}_L^{\phi\phi}$and $\hat{C}_L^{\phi\delta_{\rm g}}$. The smoothed response function is shown in Figure 4.1 and the results of varying the smoothing length is shown in the fifth panel of both Figures 5.6 and 5.7. In both auto- and cross-spectra, the variations show negligible differences, with a maximum discrepancy of 0.3σ when using a 1D response function.

Table 5.3. Table summarizing $\hat{C}_L^{\phi\phi}$ systematic test fits

Systematic change	χ^2/ν	PTE
$\ell_{\rm max} = 3500$	15.3/20	0.76
$\ell_{\rm max} = 2500$	10.5/19	0.94
$\ell_{\rm min} = 50$	14.6/20	0.80
Cut=$[2000, 350]$	15.6/20	0.74
Cut=$[1200, 250]$	19.6/20	0.48
Cut=$[2200, 150]$	31.5/20	0.05
$R_{\rm clus} = [10', 5']$	27.8/20	0.11
$R_{\rm clus} = [15', 10']$	12.3/20	0.90
$\mathrm{S/N}_{\rm clus} > 10$	16.1/20	0.71
$\mathrm{S/N}_{\rm clus} > 20$	22.8/20	0.30
$\lambda = L/10$	15.0/20	0.77
$\lambda = L/40$	14.1/20	0.82
$\lambda = \infty (1D)$	11.5/20	0.93

Note. — χ^2 and corresponding PTE relative to zero for the deviation of the systematically modified $\hat{C}_L^{\phi\phi}$ from the baseline $\hat{C}_L^{\phi\phi}$.

5.5.2.5 SPT-SZ Beam Error

Due to the modifications made to the telescope between the observing years, each field has a slightly different beam. In the baseline analysis, we deconvolve each field with a specific year beam, and convolve with a common Gaussian beam of FWHM=1.75′. We also test the lensing reconstruction using (i) the four single year beams for all the fields (e.g. incorrectly applying the 2008 beam to observations from all four years) and (ii) the average of the year beams for all the fields. This effectively probes the sensitivity of the resulting map to the uncertainty of the beam, which is smaller than the variations between the different years.

The effect of the beam is most prominently seen in $\hat{C}_L^{\phi\delta_g}$ with a maximum deviation of 0.41σ when assuming the 2008 beam to all the fields. Deconvolving all the fields with a mean beam produces a maximum deviation of 0.021σ and 0.029σ for $\hat{C}_L^{\phi\phi}$ and $\hat{C}_L^{\phi\delta_g}$ respectively, suggesting that it is a good approximation of the baseline method. The results are shown in the sixth panel of both Figures 5.6 and 5.7.

5.5.2.6 SPT-SZ Calibration Error

The CMB power as measured by SPT-SZ is calibrated to align with the measurements made by *Planck* in the same patch of sky to an accuracy of ∼0.3% (Hou et al., 2017). The results of varying this calibration parameter by ±1% (which is purposely set larger than the actual uncertainty we have to amplify the effect), is shown in the bottom panel of Figures 5.6 and 5.7. The resulting $\hat{C}_L^{\phi\phi}$ and $\hat{C}_L^{\phi\delta_g}$ vary by at most 0.20σ and 0.16σ, respectively, through this variation.

5.5.2.7 Biases Due To Faint Foreground Sources

Temperature-based lensing reconstruction is fractionally biased due to correlations with foreground components. We therefore consider the fractional lensing biases due to tSZ-4 point ($\phi(T_{\rm tSZ}, T_{\rm tSZ})\times\phi(T_{\rm tSZ}, T_{\rm tSZ})$), CIB-4 point ($\phi(T_{\rm CIB}, T_{\rm CIB})\times\phi(T_{\rm CIB}, T_{\rm CIB})$), tSZ^2-$\phi$ ($\phi(T_{\rm tSZ}, T_{\rm tSZ})\times\phi(T_{\rm CMB}, T_{\rm CMB})$) and CIB^2-$\phi$ ($\phi(T_{\rm CIB}, T_{\rm CIB})\times\phi(T_{\rm CMB}, T_{\rm CMB})$) correlations for sources that are unmasked in the analysis. We interpolate the results presented in van Engelen et al. 2014 using the four compo-

nents as a function of L, and apply it to the fiducial model when calculating the best-fit amplitudes. The results are summarized in Table 5.2, and it can be seen that the amplitude fits increase by $\sim 0.5\sigma$.

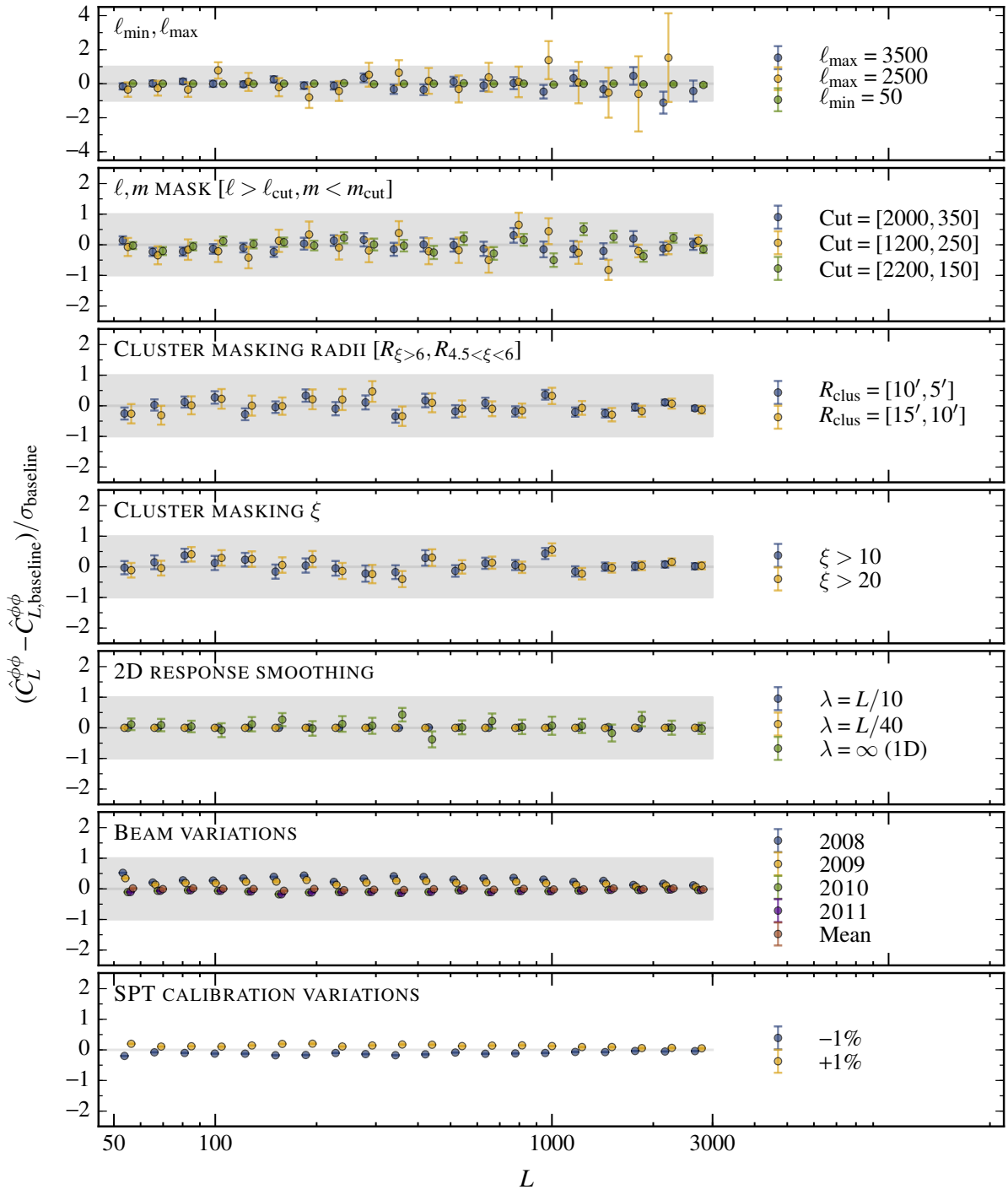

Figure 5.6 Systematic tests for the lensing power spectrum $\hat{C}_L^{\phi\phi}$. Ratio of measured $\hat{C}_L^{\phi\phi}$ with variations made against input baseline $\hat{C}_L^{\phi\phi}$, where baseline $\hat{C}_L^{\phi\phi}$ is calculated using $\ell_{\rm min} = 100$, $\ell_{\rm max} = 3000$, (ℓ, m) cut at $[2000, 250]$, $R_{\rm clus} = [5', 5']$, $\sigma = L/20$ and beams appropriate for each SPT field (grey band). The error bars shown are the standard deviations of the *change* in $\hat{C}_L^{\phi\phi}$ over a set of simulations.

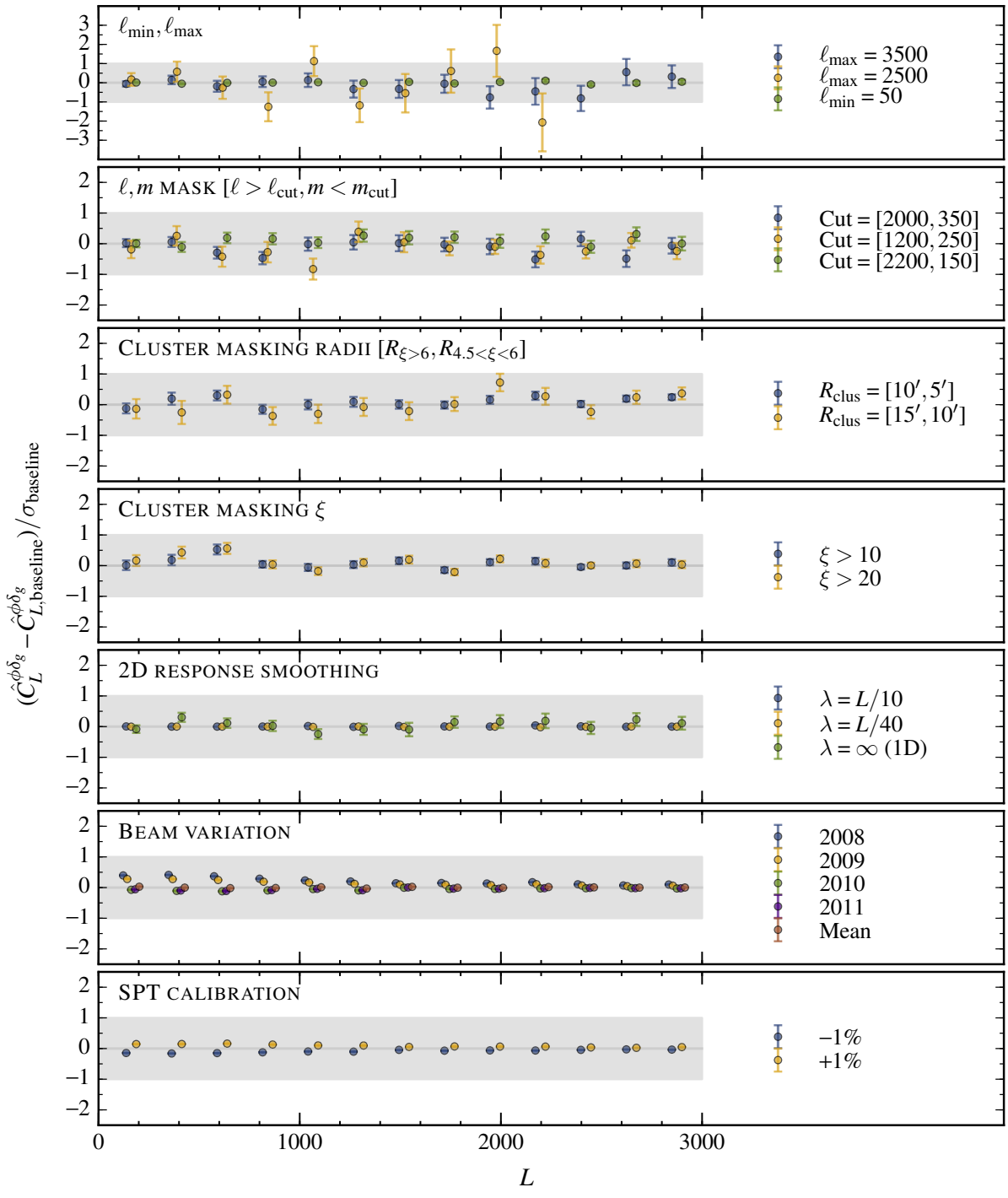

Figure 5.7 Systematic tests for the CMB lensing-galaxy density cross-spectrum. Ratio of measured $\hat{C}_L^{\phi\delta_g}$ with variations made against baseline $\hat{C}_L^{\phi\delta_g}$.

6

Cross-correlation theory

6.1 Theory

The dominant constituent of the total mass in the universe is dark matter. Unlike baryonic matter, dark matter does not emit electromagnetic radiation (although theories of gamma-ray emission through self-annihilation of dark matter exist), and therefore its distribution can not be mapped using a standard telescope. Therefore, this is achieved by either (i) studying the distribution, clustering and kinematics of galaxies to infer the amount of underlying dark matter, or by (ii) using distortions in the background image such as high redshift galaxies or the CMB to infer the location and amount of matter. Since all of these observables are related to the underlying mass distribution, the galaxy and CMB weak lensing fields are statistically correlated with each other.

In Chapter 2, it was shown that the projected convergence in a given direction is:

$$\kappa(\vec{\theta}) = \frac{3H_0^2\Omega_{\mathrm{m},0}}{2c^2}\int_0^{\chi_*} d\chi W(\chi) f_K(\chi)\frac{\delta[f_K(\chi)\vec{\theta},\chi]}{a(\chi)} \tag{6.1}$$

where $W(\chi)$ is defined as:

$$W(\chi) = \int_{\chi}^{\chi_*} d\chi' n^{\mathrm{s}}(\chi)\frac{f_K(\chi^{\mathrm{s}}-\chi)}{f_K(\chi^{\mathrm{s}})}, \tag{6.2}$$

with n_{s} being the source galaxy redshift distribution, which for the CMB is taken to be a delta function at $\chi = \chi_{\mathrm{CMB}}$. We will denote CMB convergence as κ_{CMB} and galaxy weak lensing convergence as κ_{E}. From this point on, we will assume a flat universe, which sets $f_K(\chi) = \chi$ using Equation 2.4. The convergence is related to the projected gravitational potential ϕ by $\kappa(\vec{\theta}) = \frac{1}{2}\nabla^2\phi(\vec{\theta})$ in position-space or $\kappa_{LM} = -\frac{1}{2}L(L+1)\phi_{LM}$ in harmonic-space.

A galaxy survey with a redshift distribution dn^l/dz that extends up to $z = z^l$ gives a projected over-density

$$\delta_{\mathrm{g}}(\vec{\theta}) = \int_0^{\chi(z^l)} d\chi b(\chi)\frac{dn^l(\chi)}{dz}\frac{dz}{d\chi}\delta_{\mathrm{m}}(\chi\vec{\theta},\chi), \tag{6.3}$$

in a given direction, where $b(z)$ is the galaxy bias defined as the ratio of galaxy and dark matter clustering, and $\delta_{\mathrm{m}}(\chi\vec{\theta},\chi)$ is the underlying matter fluctuation at a given comoving distance in a given direction. In Equation 6.3, we have explicitly added the subscript n^l to denote the redshift distribution of *lens* galaxies, which are different from the *source* galaxies used for weak lensing measurements denoted by n^{s}.

The auto/cross-angular power spectra (using the Limber approximation) relevant to this work are:

$$C_L^{\delta_{\mathrm{g}}\delta_{\mathrm{g}}} = \int d\chi \frac{1}{\chi^2} W^{\delta_{\mathrm{g}}}(\chi) W^{\delta_{\mathrm{g}}}(\chi) P(k = L/\chi, \chi(z)), \tag{6.4}$$

$$C_L^{\kappa_{\mathrm{CMB}}\delta_{\mathrm{g}}} = \int d\chi \frac{1}{\chi^2} W^{\kappa_{\mathrm{CMB}}}(\chi) W^{\delta_{\mathrm{g}}}(\chi) P(k = L/\chi, \chi(z)), \tag{6.5}$$

$$C_L^{\kappa_{\mathrm{CMB}}\kappa_{\mathrm{E}}} = \int d\chi \frac{1}{\chi^2} W^{\kappa_{\mathrm{CMB}}}(\chi) W^{\kappa_{\mathrm{E}}}(\chi) P(k = L/\chi, \chi(z)), \tag{6.6}$$

where $P(k, \chi(z))$ is the non-linear matter power spectrum at a given comoving distance, and

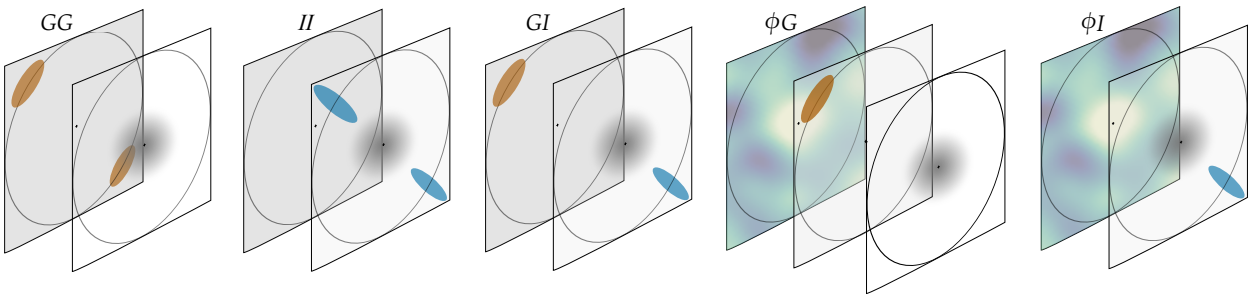

Figure 6.1 Schematic drawings of various lensing effects from left to right: GG, II, GI, ϕG, ϕI. In each case, the planes represent different redshift slices and the central grey haze represents a massive structure. Orange ellipses represent galaxy images that are distorted through the weak lensing effect, whereas the blue ellipses represent galaxies that are stretched or rotated due to tidal forces. The coloured planes on the right panels represent the CMB lensing map.

$W^{\kappa_{\rm CMB}}(\chi)$, $W^{\delta_{\rm g}}(\chi)$, $W^{\kappa_{\rm E}}(\chi)$ are the CMB lensing, galaxy density and galaxy weak lensing kernels defined as:

$$W^{\kappa_{\rm CMB}}(\chi) = \frac{3H_0^2\Omega_{\rm m}}{2c^2}\frac{\chi}{a(\chi)}\frac{\chi_{\rm CMB}-\chi}{\chi_{\rm CMB}} \tag{6.7}$$

$$W^{\delta_{\rm g}}(\chi) = b(\chi)\frac{dn^l(\chi)}{dz}\frac{dz}{d\chi} \tag{6.8}$$

$$W^{\kappa_{\rm E}}(\chi) = \frac{3H_0^2\Omega_{\rm m}}{2c^2}\frac{\chi}{a(\chi)}\int_0^{\chi_*} d\chi' \frac{dn^{\rm s}}{dz}\frac{dz}{d\chi}\frac{\chi'-\chi}{\chi'}. \tag{6.9}$$

6.1.1 Intrinsic Alignment

In making a galaxy weak lensing measurement, the fundamental assumption is that the source galaxies are oriented randomly for a sufficiently large sample. Lensing induces a coherent distortion in a galaxy image, which we statistically infer as the lensing signal. However, due to tidal torquing, galaxies may not be randomly oriented. This effect aligns galaxies in such a way that the projected semi-major axis becomes aligned with the tidal field of a structure, which introduces a bias in the measurement of weak lensing (Joachimi et al., 2015). This effect, known as intrinsic alignment (IA), has different configurations, and the various types are illustrated in Figure

6.1. GG (galaxy-galaxy) type correlation is the desired signal in galaxy weak lensing two-point correlation measurements, whereas II (intrinsic-intrinsic) and GI (galaxy-intrinsic) type correlations are contaminations to the GG measurement since it creates false signal. In the case of CMB weak lensing - galaxy weak lensing cross-correlations, the desired signal is ϕG correlation, whereas ϕI correlation is a contamination term. The effect of IA can be modelled using Equation 6.6 but by replacing the galaxy lensing kernel with that of IA assuming a non-linear alignment (NLA) model (Hirata & Seljak, 2004; Bridle & King, 2007):

$$W^I(\chi) = -C_1 \rho_{\rm crit,0} \frac{\Omega_{\rm m}}{D(\chi)} n^{\rm s}(\chi) \tag{6.10}$$

where $\rho_{\rm crit,0} = 3H_0^2/8\pi G$ is the critical density at $z = 0$, $C_1 = 5 \times 10^{-14} h^{-2} M_\odot^{-1} {\rm Mpc}^3$ is a normalization constant that is scaled to match the observed amplitude from SuperCOSMOS at low redshift (Brown et al., 2002) and $D(\chi)$ is a linear growth function normalized at z=0. This introduces an additional term in the cross-correlation:

$$C_{L,\rm obs}^{\kappa_{\rm CMB}\kappa_{\rm E}} = C_{L,\rm true}^{\kappa_{\rm CMB}\kappa_{\rm E}} + C_L^{\kappa_{\rm CMB} I}. \tag{6.11}$$

6.1.2 Tangential Shear

An alternative widely utilized method to extract the weak lensing signal is using tangential shear, which uses galaxy shapes directly to measure the excess projected mass within an aperture (Miralda-Escude, 1991; Squires & Kaiser, 1996). Following the derivation given in Kilbinger 2015, the mean convergence $\bar{\kappa}$ within radius θ is:

$$\bar{\kappa}(\leq \theta) = \frac{1}{\pi\theta^2} \int_0^\theta \int_0^{2\pi} \kappa(\theta', \varphi) \theta' d\theta' d\varphi \tag{6.12}$$

$$= \frac{2}{\theta^2} \int_0^\theta d\theta' \theta' \langle \kappa(\theta') \rangle_\varphi, \tag{6.13}$$

where we have used $\langle\kappa(\theta')\rangle_\varphi = (2\pi)^{-1}\int_0^{2\pi} d\varphi\ \kappa(\theta',\varphi)$. We can compute the derivative of this and obtain:

$$\frac{\partial[\theta\bar{\kappa}(\leq\theta)]}{\partial\theta} = -\bar{\kappa}(\leq\theta) + 2\langle\kappa(\theta)\rangle_\varphi. \tag{6.14}$$

Alternatively, we can apply the divergence theorem on Equation 6.12 (and using $\kappa = \frac{1}{2}\nabla\cdot\nabla\phi$):

$$\begin{aligned}\bar{\kappa}(\leq\theta) =& \frac{1}{\pi\theta^2}\int_0^\theta\int_0^{2\pi}\kappa(\theta',\varphi)\theta' d\theta' d\varphi \\ =& \frac{1}{\pi\theta^2}\int_0^{2\pi}\frac{1}{2}\partial_\theta\phi(\theta,\varphi)\ \theta d\varphi \\ =& \frac{1}{2\pi\theta}\int_0^{2\pi}\partial_\theta\phi(\theta,\varphi)d\varphi.\end{aligned} \tag{6.15}$$

Taking a derivative in the radial direction gives:

$$\frac{\partial[\theta\bar{\kappa}(\leq\theta)]}{\partial\theta} = \int_0^{2\pi}\frac{d\varphi}{2\pi}\partial_\theta\partial_\theta\phi(\theta,\varphi) = \langle\kappa(\theta)\rangle_\varphi - \langle\gamma_{\rm t}(\theta)\rangle_\varphi. \tag{6.16}$$

Equating this expression with Equation 6.14, we obtain:

$$\langle\gamma_{\rm t}(\theta)\rangle_\varphi = \bar{\kappa}(\leq\theta) - \langle\kappa(\theta)\rangle_\varphi, \tag{6.17}$$

and therefore the mean tangential shear at radius θ is the difference between the total projected mass within θ and the mean convergence at radius θ.

Tangential shear is equivalently the real part of the complex shear $\gamma = \gamma_1 + i\gamma_2$ and can be written as:

$$\gamma_{\rm t} = -{\rm Re}\{\gamma e^{-2i\varphi}\} \tag{6.18}$$

where the minus is a sign convention to ensure positive $\gamma_{\rm t}$ around over-densities and negative $\gamma_{\rm t}$ around under densities. The imaginary part is referred to as the cross-shear component:

$$\gamma_\times = -{\rm Im}\{\gamma e^{-2i\varphi}\}. \tag{6.19}$$

Using these, two-point correlations between γ_t and $\gamma_\times$ can be calculated. While $\langle\gamma_t\gamma_t\rangle$ and $\langle\gamma_\times\gamma_\times\rangle$ are non-zero, $\langle\gamma_t\gamma_\times\rangle$ is expected to vanish in a parity symmetric universe (Kilbinger, 2015). The non-zero two point correlation functions are combined to form two cosmic shear measurements :

$$\xi_+ = \langle\gamma\gamma^*(\theta)\rangle_\varphi \qquad = \langle\gamma_t\gamma_t(\theta)\rangle_\varphi + \langle\gamma_\times\gamma_\times(\theta)\rangle_\varphi \tag{6.20}$$

$$\xi_- = \mathrm{Re}\left[\langle\gamma\gamma^*(\theta)\rangle_\varphi e^{-4i\varphi}\right] = \langle\gamma_t\gamma_t(\theta)\rangle_\varphi - \langle\gamma_\times\gamma_\times(\theta)\rangle_\varphi. \tag{6.21}$$

While these cosmic shear measurements are not explicitly presented in this thesis, it is part of the covariance matrix that is used in Chapter 8 to constrain cosmological parameters.

6.1.3 Power Spectra and Correlation Functions

We work in both harmonic-space using angular power spectra C_L and in position-space using angular correlation functions ξ_θ, depending on the application. The two are related by the transformations (Peacock, 1999; Ansari & Magneville, 2010):

$$\xi_\theta^{\alpha\beta} = \sum_{L=0}^{L=\infty}\left(\frac{2L+1}{4\pi}\right)P_L(\cos(\theta))C_L^{\alpha\beta} \tag{6.22}$$

$$C_L^{\alpha\beta} = 2\pi\int_{-1}^{+1}\xi_\theta^{\alpha\beta}P_L(\cos(\theta))d(\cos(\theta)), \tag{6.23}$$

where $\alpha,\beta = \{\kappa_{\rm CMB},\delta_g,\kappa_E\}$, and P_L are the Legendre polynomials. The theoretical spectrum of $\kappa_{\rm CMB}\times\gamma_t$ correlation is computed by calculating $C_L^{\kappa_{\rm CMB}\kappa_E}$ first, and converting to position-space via (Harnois-Déraps et al., 2017):

$$\xi_\theta^{\kappa_{\rm CMB}\gamma_t} = \frac{1}{2\pi}\int_0^\infty dLLC_L^{\kappa_{\rm CMB}\kappa_{\rm gal}}J_2(L\theta), \tag{6.24}$$

where J_2 is the Bessel function of the first kind of order 2.

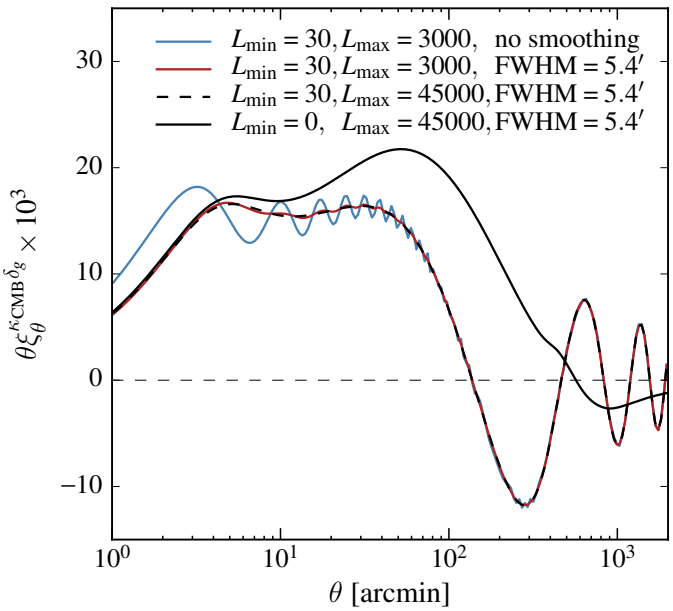

Figure 6.2 Comparison of theory spectra calculated with $L_{\rm min}$=0, 30, $L_{\rm max}$=3000, 45000 and with and without Gaussian smoothing of FWHM = 5.4′. We observe that comparing our measurements with a theoretical spectrum that assumes a different $L_{\rm min}$ will underestimate our amplitude.

6.1.4 Scale Cuts

The CMB convergence map is primarily reconstructed in harmonic-space, resulting in harmonic coefficients of the convergence map κ_{LM}. However, not all of the modes are useful since the low-L modes are not accurately measured due to our finite sky area. These modes are often removed from the analysis, and the same treatment must be made in calculating the theory spectrum. Figure 6.2 shows the difference in the theory calculation with and without the $L_{\rm min}$ cut, suggesting that omitting this consideration will bias the amplitude significantly. On the other hand, applying a sharp $L_{\rm max}$ cut introduces oscillations in the calculated spectrum (due to the limit on the sum in Equation 6.22). This effect is reduced when a FWHM = 5.4′ Gaussian beam (i.e. a smooth transition to zero) is applied.

6.2 Flask Simulations

In the standard paradigm of gravitational structure growth, the initial density field is assumed to be Gaussian. As structures grow, the over-densities and under-densities evolve differently*. When the universe expands, background matter gets displaced somewhat less near over-densities, which allows for a quicker gravitational turn-around (where gravitational collapse dominates over the expansion), and will therefore have more time to accumulate mass. The statistics of the evolved density field is difficult to describe analytically down to galactic scales due to non-linear gravitational evolution that affects cosmic structures in an intricate way.

One model that can be used to approximate the evolved density field is the lognormal distribution. As the name suggests, a lognormal distribution is a distribution where the logarithm of a random variable is normally distributed. It is guaranteed to have a density $\rho > 0$ and is arbitrarily close to a Gaussian field at early times (Coles & Jones, 1991). Furthermore, it was recently verified that the convergence measured from the DES galaxies can be well-approximated by a lognormal distribution (Clerkin et al., 2017).

The lognormal characteristic is naturally embedded in N-body simulations, which are therefore ideal in producing mock data. However, generating multiple N-body realizations is a computationally intensive task. Although the DES collaboration is producing $\mathcal{O}(10)$ realizations for Y1-data analysis, we take a slightly different approach here and produce lognormal fields using the publicly available code Full-sky Lognormal Astro-fields Simulation Kit (Flask, Xavier et al. 2016), which is capable of producing multiple correlated Gaussian or lognormal fields on a sphere.

We run Flask in lognormal mode, and use theoretical angular power spectra C_L^{ij} where $i, j \in \{\delta_g^1, \delta_g^2, \delta_g^3, \delta_g^4, \delta_g^5, \gamma^1, \gamma^2, \gamma^3, \gamma^4, \kappa_{\rm CMB}\}$, where $\delta_{\rm g}$ is the galaxy density field, γ is the galaxy weak lensing field and the superscript denotes the redshift bin (summarized in Table 6.1). $\kappa_{\rm CMB}$ is taken to be the convergence field at $z = 1089$. In total, we use 55 angular power spectra to pro-

*Taking the definition of $\delta = (\rho - \langle\rho\rangle)/\langle\rho\rangle$, there is a restriction on the value that underdensities can reach ($\delta = -1$, when $\rho = 0$), whereas there are no limits on overdensities. In linear-theory, where $|\delta| \ll 1$, underdensities are similar to overdensities.

duce 10 maps, all of which are correlated with each other according to the set of spectra that we provide to the code. The input spectra are produced using the cosmology chosen by the DES collaboration ($\Omega_{\rm m} = 0.295$, $\Omega_\Lambda = 0.705$, $\Omega_{\rm b} = 0.0468$, $\sigma_8 = 0.834$, $A_{\rm s} = 2.26 \times 10^{-9}$, $\Omega_{\rm k} = 0$, $h = 0.688$, $n_{\rm s} = 0.968$, $w = -1$, $\Omega_\nu h^2 = 0.0006$). For the lens galaxies (making up the $\delta_{\rm g}$ fields), the redshift distributions of REDMAGIC samples are used, number densities are set to $\bar{n}^l = [0.013, 0.034, 0.051, 0.030, 0.009]$ gal/arcmin^2 and the galaxy biases are set to $b = [1.45, 1.55, 1.65, 1.80, 2.00]$. For the source galaxies (making up the γ fields) we set the shape noise to $\sigma_\gamma = [0.37, 0.42, 0.39, 0.40]$, and number densities to $\bar{n}^{\rm s} = [1.50, 1.52, 1.59, 0.79]$ gal/arcmin^2 (Troxel et al., 2017) and the redshift distributions of the METACALIBRATION samples (Sheldon & Huff 2017; described in Section 7.4) are used. The maps are produced at a HEALPIX resolution of $N_{\rm side} = 4096$ with a maximum multipole of $L = 4096$. The lens galaxy catalogues are generated by drawing from a Poisson distribution with an expectation value of $\bar{n}(1 + \delta_{\rm g})$ for a given pixel, where $\bar{n}$ is the average number of galaxies, and $\delta_{\rm g}$ is the density field produced by FLASK. For the source galaxy catalogue, γ_1 and γ_2 values are taken from each pixel of the shear maps produced by FLASK and a noise component $\sigma_\gamma/\sqrt{2} \times \mathcal{N}(0, 1)$ (where σ^2_γ=$\sigma^2_{\gamma,1}$+$\sigma^2_{\gamma,2}$ and $\mathcal{N}$ is a normal distribution with $\mu = 0$, $\sigma = 1$) is added.

For the CMB convergence field, Gaussian realizations of the noise maps produced from the $N_L^{(0)}$ noise spectrum are added to the noiseless convergence maps from FLASK to produce realistic $\kappa_{\rm CMB}$ maps. We apply the same mask used in the lensing reconstruction where the mask is a combination of SPT boundary mask that is apodized with FWHM $= 30'$, and a mask that removes point sources detected above 50 mJy and clusters above $\mathrm{S/N}_{\rm clus} > 6$ using an aperture of $R = 5'$. We then transform to harmonic-space, remove modes in the ranges $L < 30$ and $L > 3000$, and transform back to position-space to apply a Gaussian smoothing of FWHM $= 5.4'$, which are the same procedures applied to the data map.

Overall, these simulations are produced to resemble the data as closely as possible. However, some systematics that are present in the data are not in the simulations (e.g. atmospheric effects, PSF shapes that deteriorate shape measurements and extragalactic foregrounds such as tSZ/CIB

Table 6.1. Table summarizing the FLASK simulation inputs.

SAMPLE		
GALAXY DENSITY FIELD	$\bar{n}^l$ [gal/arcmin^2]	b
$0.15 < z < 0.30$	0.013	1.45
$0.30 < z < 0.45$	0.034	1.55
$0.45 < z < 0.60$	0.051	1.65
$0.60 < z < 0.75$	0.030	1.80
$0.75 < z < 0.90$	0.009	2.00
GALAXY WEAK LENSING FIELD	$\bar{n}^s$ [gal/arcmin^2]	σ_γ
$0.20 < z < 0.43$	1.50	0.37
$0.43 < z < 0.60$	1.52	0.42
$0.60 < z < 0.90$	1.59	0.39
$0.90 < z < 1.30$	0.79	0.40
$\kappa_{\rm CMB}$ FIELD		
$z = 1089$		

that affect the CMB lensing map).

7

CMB lensing cross-correlations with the Dark Energy Survey

7.1 Overview

The Dark Energy Survey (DES) is an optical survey that covers 5000 deg^2 of the sky. The survey is conducted using the 570 Megapixel DECam instrument (Honscheid et al., 2008; Flaugher et al., 2015) mounted on the Cerro Tololo Inter-American Observatory (CTIO) 4-meter Victor Manuel Blanco telescope located in Chile. The goal of the survey is to shed light on the nature of dark energy as well as other cosmological parameters using galaxy clustering, galaxy weak lensing, galaxy clusters and supernovae (The Dark Energy Survey Collaboration, 2005).

To test the performance of DECam and the data reduction pipeline, the DES collaboration first conducted the science verification (SV) survey. The SV observations were taken between

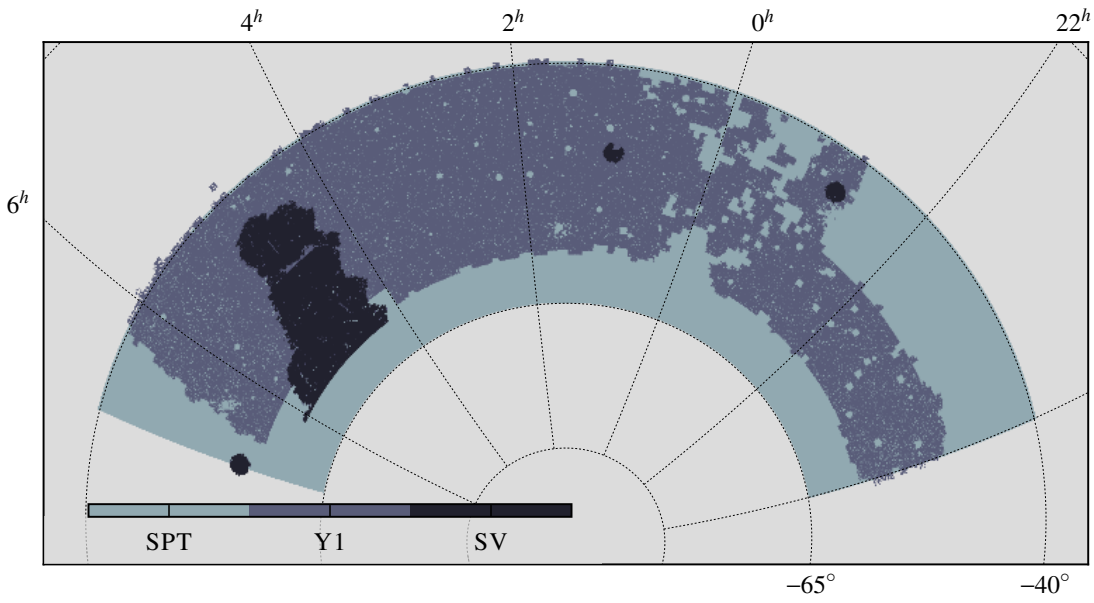

Figure 7.1 Comparison of SPT nominal, DES-Y1 shear (SPT patch only) and DES-SV shear footprints. The area covered are approximately 2500 deg^2, 1100 deg^2 and 140 deg^2 for SPT, DES-Y1 and DES-SV respectively.

November 2012 and February 2013, and were conducted on a ∼140 deg^2 patch that lies within the SPT footprint. The survey used ten exposures to mimic the depth of the full 5-year survey, but achieved a shallower effective depth due to variable weather and early operational difficulties. Results of various analyses including galaxy clustering (Crocce et al., 2016), galaxy-galaxy lensing (Prat et al., 2016; Clampitt et al., 2017), cosmic shear (Becker et al., 2016) and cross-correlations with CMB lensing maps from SPT-SZ and *Planck* (Giannantonio et al., 2016; Kirk et al., 2016) were published in 2015/2016, and the galaxy catalogue, photometric redshifts and shape measurements are now publicly available[*]. We include the published results from Kirk et al. 2016 et al. in this thesis.

The DES year-1 (Y1) data were taken between August 2013 to February 2014 and covers ∼1300 deg^2 but to a shallower depth compared to DES-SV (four exposures instead of ten). The SPT, SV and Y1 footprints are shown in Figure 7.1. The Y1 footprint additionally overlaps with

[*]https://des.ncsa.illinois.edu/releases/sva1

the Sloan Sky Digital Sky Survey (SDSS; Eisenstein et al. 2011) stripe-82 region where spectroscopic redshift data exist, which are used to calibrate photometric redshifts of galaxies. Analysis of the Y1 data is currently being conducted and will be completed towards the end of 2017. Due to the blinding strategy taken, the results for DES-Y1 cross-correlations are not permitted to be presented as official results. Therefore, in this thesis, we present the results based on FLASK simulations, and treat the results as a forecast.

The first measurement of the CMB weak lensing effect was achieved (Smith et al., 2007) by cross-correlating CMB lensing derived from *WMAP* (Bennett et al., 2003c) with the overdensities of radio galaxies in the NRAO VLA Sky Survey (Condon et al., 1998). More recently, a (42σ) detection has been achieved by cross-correlating CMB lensing and CIB maps from *Planck* (Planck Collaboration et al., 2014c). Higher resolution ground based CMB experiments such as SPT (Bleem et al., 2012; Giannantonio et al., 2016) and ACT (Allison et al., 2015) have also measured cross-correlations with galaxies. Additionally, initial measurements of the galaxy weak lensing - CMB weak lensing correlation have been made using CMB experiments such as SPT, ACT, *Planck*, and galaxy weak lensing surveys such as CFHTLenS, RCSLenS and KiDS-450 (Hand et al., 2015; Liu & Hill, 2015; Harnois-Déraps et al., 2016, 2017).

This chapter is organized as follows. The data, methodology used, and the results of the cross-correlation between DES-SV galaxy weak lensing and SPT-SZ CMB weak lensing are presented in Section 7.2. Descriptions of the Y1 data and simulations are presented in Sections 7.3 and 7.4. Finally, a discussion of biases in the cross-correlation measurements due to extragalactic foregrounds are given in Section 7.5.

7.2 DES-SV Galaxy Weak Lensing

7.2.1 Data

The DES-SV weak lensing data covers $\sim$140 deg^2, and this is cross-correlated with the SPT-SZ CMB lensing map. Descriptions of the DES-SV shear catalogues can be found in Jarvis et al. 2016, and shapes measured by two independent pipelines NGMIX (Sheldon, 2014) and IM3SHAPE

(Zuntz et al., 2013) are used in the analysis. Shape measurements were tested against systematic errors and were shown to be robust, and the catalogues are used to measure different cosmological probes (see e.g. Becker et al. 2016; Prat et al. 2016; Clampitt et al. 2017). In this study, NGMIX is chosen for the main analysis since the source galaxy number density is slightly higher (5.7 galaxies/arcmin^2) compared to IM3SHAPE (3.7 galaxies/arcmin^2). We project the calibrated shear components γ_1 and γ_2 onto a HEALPIX map of $N_{\rm side} = 2048$. This corresponds to a maximum resolution of $\sim 1.7'$ or $L \sim 6000$ although we do not attempt to reach these scales due to the noise in the CMB lensing map.

The lensing map used for SV analysis is based on the SPT-SZ 150 GHz data alone. While the same 150 GHz data are used for the lensing map reconstruction described in Chapters 3-5, the two lensing maps are reconstructed using independent pipelines, and are therefore, similar but different maps. In particular, the lensing map used in the SV analysis is reconstructed under the flat-sky approximation, using temperature modes of $\ell < 4000$, and $\ell_x > 500$. Point sources detected by SPT-SZ above $>15\sigma$ and clusters above $\mathrm{S/N}_{\rm clus} > 6$ were removed by applying a mask of $16' \times 16'$ at their locations, and the final map is provided as a HEALPIX map of $N_{\rm side} = 2048$.

In addition to the SPT-SZ lensing map, the DES-SV weak lensing data are correlated with the publicly available[†] *Planck* 2015 lensing map (Planck Collaboration XV., 2015). This lensing map was produced by taking a linear combination of temperature and polarization data from different frequency bands (ranging from 30-353 GHz) from the *Planck* satellite using the Spectral Matching Independent Component Analysis (SMICA; Cardoso et al. 2008). The lensing potential map $\hat{\phi}$ is produced by applying the standard quadratic estimator technique (Okamoto & Hu, 2003). All the possible combinations between temperature and polarizations $\{\phi^{TT}, \phi^{EE}, \phi^{TE}, \phi^{TB}, \phi^{EB}\}$ were used to construct an estimate of ϕ, and these were combined to form a minimum variance estimate of the lensing potential ϕ^{MV}.

[†]http://irsa.ipac.caltech.edu/data/Planck/release_2/all-sky-maps/maps/component-maps/lensing/COM_CompMap_Lensing_2048_R2.00.tar

7.2.2 Methods

Galaxy shear is intrinsically a spin-2 quantity since rotations of ellipses by 180° give the same shape. We can convert the raw ellipticity measurements into convergence (spin-0/scalar quantity) using two methods. The first method is the traditional flat-sky Kaiser-Squires reconstruction (Kaiser & Squires, 1993) of producing a convergence map from galaxy shear measurements. A rotation of the form:

$$\gamma_1 = \cos(2\varphi)\gamma_1^{\rm cat} - \sin(2\varphi)\gamma_2^{\rm cat} \tag{7.1}$$

$$\gamma_2 = \sin(2\varphi)\gamma_1^{\rm cat} + \cos(2\varphi)\gamma_2^{\rm cat}, \tag{7.2}$$

is first applied to the shear measurement listed in the catalogue, which is measured with respect to lines of equal right ascension and declination. The transformation rotates the shear measurement with respect to the image coordinates. The γ_1, γ_2 maps are converted into $\kappa_{\rm E}$ by Fourier transforming γ_1, γ_2 using (see A.5 for derivation):

$$\kappa_{\rm E}(\ell_x, \ell_y) = \gamma_1(\ell_x, \ell_y)\frac{\ell_x^2 - \ell_y^2}{\ell_x^2 + \ell_y^2} + \gamma_2(\ell_x, \ell_y)\frac{2\ell_x^2\ell_y^2}{\ell_x^2 + \ell_y^2}, \tag{7.3}$$

where $\ell_x = 1/\theta_x$ and $\ell_y = 1/\theta_y$. Similarly, its counterpart, $\kappa_{\rm B}$ is written as:

$$\kappa_{\rm B}(\ell_x, \ell_y) = \gamma_1(\ell_x, \ell_y)\frac{\ell_x^2 - \ell_y^2}{\ell_x^2 + \ell_y^2} - \gamma_2(\ell_x, \ell_y)\frac{2\ell_x^2\ell_y^2}{\ell_x^2 + \ell_y^2}, \tag{7.4}$$

and these can be correlated with $\kappa_{\rm CMB}(\ell_x, \ell_y)$.

The second method is decomposing the spin-2 field from galaxy shape measurements using spin-weighted spherical harmonics (Bartelmann, 2010):

$${}_{\pm2}p = \frac{1}{2}(\gamma_1 \mp i\gamma_2) = \sum_{LM} {}_{\pm2}p_{LM}\ {}_{\pm2}Y_{LM}. \tag{7.5}$$

This procedure is commonly used in decomposing the linear polarization of the CMB, however

with $\gamma_1 \to Q$ and $\gamma_2 \to -U$, where Q and U are the Stokes parameters. The linear combinations of these spin-weighted spherical harmonic coefficients can be used to decompose the fields into scalar (spin-0) fields (Bartelmann, 2010):

$$\kappa_{\mathrm{E},LM} = -(p_{2,LM} + p_{-2,LM}) \tag{7.6}$$

$$\kappa_{\mathrm{B},LM} = -i(p_{2,LM} - p_{-2,LM}). \tag{7.7}$$

It can be shown that this reduces to the Kaiser-Squires reconstruction in the flat-sky limit. The cross-correlation between κ_{CMB} and $\kappa_{\mathrm{E},LM}/\kappa_{\mathrm{B},LM}$ is analogous to computing correlations between the temperature and polarization in the CMB literature, and there are numerous tools that are capable of computing this efficiently. We use the public code PolSpice (Chon et al., 2004; Szapudi et al., 2001) to compute this cross-correlation, where the triplet $\{\kappa_{\mathrm{CMB}}, \gamma_1, \gamma_2\}$ is used as input. The advantage of using this method is that the code processes the mode-couplings due to the masks, which we must manually compute otherwise (See Section A.4).

7.2.3 Results

The results of measurements using the full-sky estimator are shown in Figure 7.2. The measurements are made over the multipole range of $64 < L < 1600$ using 16 bins. These results are compared with the theory spectrum calculated using Equation 6.6. We vary the amplitude of this theory spectrum by multiplying by a single multiplicative scaling constant A, and compute the χ^2 using:

$$\chi^2 = \sum_L \frac{(C^{\kappa_{\mathrm{CMB}}\kappa_{\mathrm{E}}}_{L,\mathrm{obs}} - AC^{\kappa_{\mathrm{CMB}}\kappa_{\mathrm{E}}}_{L,\mathrm{theory}})^2}{(\sigma^{\kappa_{\mathrm{CMB}}\kappa_{\mathrm{E}}})^2}, \tag{7.8}$$

where we have assumed a diagonal covariance. We obtain a best-fit amplitude of $A = 0.88 \pm 0.30$ for DES-SV $\times$ SPT-SZ and $A = 0.86 \pm 0.39$ for DES-SV $\times$ *Planck*, which corresponds to a signal of 2.9 and 2.2σ respectively. As a consistency check, we also check the amplitude using the flat-sky Kaiser-Squires reconstruction and obtain an amplitude of $A = 0.92 \pm 0.30$ for DES-SV $\times$ SPT-SZ and $A = 0.91 \pm 0.39$ for DES-SV $\times$ *Planck*, with χ^2/dof of 1.18 and 1.17, which is consistent

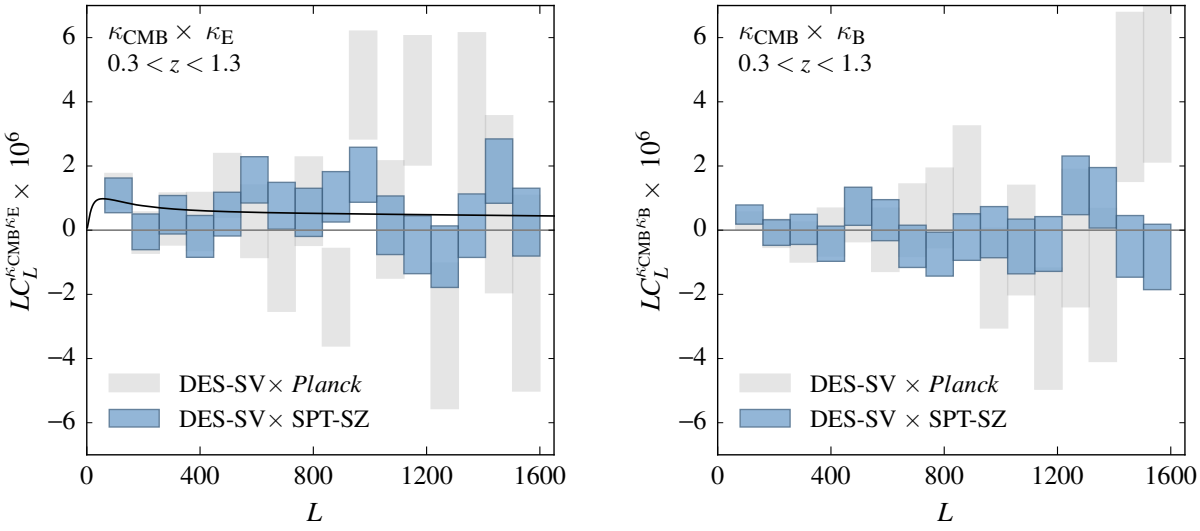

Figure 7.2 Cross-correlation between $\kappa_{\rm CMB}$ and $\kappa_{\rm E}, \kappa_{\rm B}$. Shown in blue are the correlation band powers for SPT-SZ and in grey are for *Planck*. These are similar to the plots published in Kirk et al. 2016.

with the full-sky method.

7.2.4 Systematics

In this section, we investigate whether our measurements are significantly affected by systematic effects, and verify that these effects are not dominating the measurement.

7.2.4.1 B-mode

Galaxy weak lensing signal can be decomposed into curl-free (E) and divergence-free (B) modes (Bartelmann, 2010). To first order, true physical weak lensing signals produce curl-free modes only. Therefore, the presence of B-modes is an indication of a systematic error present in the reconstruction process, which could either be astrophysical (e.g. intrinsic alignment (IA) of galaxies, source redshift clustering (Schneider et al., 2002)) or non-astrophysical (e.g. miscalibration of the point spread function, atmospheric fluctuations, shape calibration bias). We measure the

cross-correlation between $\kappa_{\rm CMB}$ and $\kappa_{\rm B}$, and obtain best-fit amplitudes of $A_{\rm B} = 0.18 \pm 0.21$ ($\chi^2/dof = 0.79$) and $A_{\rm B} = 0.17 \pm 0.25$ ($\chi^2/dof = 0.92$) for DES-SV $\times$ SPT-SZ and DES-SV $\times$ *Planck* respectively. Additionally, we compute the fit with respect to $A_{\rm E} = 0$, and obtain $\chi^2/dof = 0.83$ and 0.95 for DES-SV $\times$ SPT-SZ and DES-SV $\times$ *Planck* respectively. This confirms that the amplitude is consistent with $A_{\rm E} = 0$.

7.2.4.2 PHOTO-z UNCERTAINTIES

The uncertainty in the redshift distribution affects the amplitude of the theoretical spectrum. The results in the main analysis are based on a theory spectrum calculated using photo-z from the SkyNet2 code (Graff et al., 2014). Here, theoretical spectra calculated using three other photo-z codes BPZ2 (Benítez, 2000), ANNz2 (Sadeh et al., 2016) and TPZ (Carrasco Kind & Brunner, 2013) are compared. Detailed descriptions of these codes and validation tests can be found in Bonnett et al. 2016. We take the redshift distribution $n(z)$ from different photo-z codes, compute the theoretical prediction for $C_L^{\kappa_{\rm CMB}\kappa_{\rm E}}$ given in Equation 6.6, and compare the results with the spectrum for SkyNet2. The results are shown in Figure 7.3, and it can be seen that the scatter between the different photo-z codes is much smaller than the statistical uncertainty from our cross-correlation measurement.

7.2.4.3 Intrinsic Alignments

Galaxy weak lensing measurements are contaminated by the non-random galaxy orientations due to gravitational forces during the galaxy formation. We model this effect using the non-linear alignment model (Equation 6.10) and the estimated IA spectrum is shown in the right panel of Figure 7.3. From taking the ratio between between $\kappa_{\rm CMB}\kappa_{\rm E}$ and $\kappa_{\rm CMB}\kappa_{\rm E} + \kappa_{\rm CMB}\kappa_{\rm I}$, we infer that the effect can be as large as 23%, when the redshift distribution from SkyNet2 is assumed. Including such an effect in the theoretical modelling of the cross-correlation shifts our best-fit amplitude for DES-SV $\times$ SPT-SZ from $A_{\rm E,no\ IA} = 0.88 \pm 0.30$ to $A_{\rm E,with\ IA} = 1.08 \pm 0.36$.

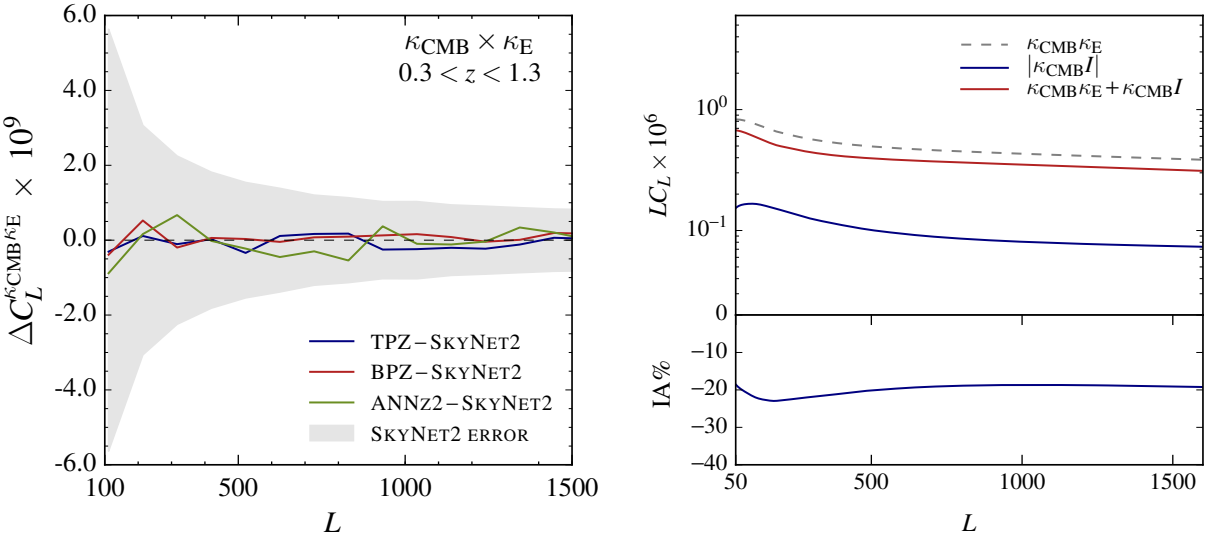

Figure 7.3 **Left:** Difference in the theory spectrum $\Delta C_L^{\kappa_{\rm CMB}\kappa_{\rm E}} = C_{L,{\rm alt}-z}^{\kappa_{\rm CMB}\kappa_{\rm E}} - C_{L,{\rm SkyNet2}}^{\kappa_{\rm CMB}\kappa_{\rm E}}$, where alt-$z$ refers to an alternative photo-z estimating pipeline. Plotted in grey are the 1σ statistical uncertainties of the measurement. **Right:** Amplitude of $\kappa_{\rm CMB}\kappa_{\rm E}$ (black dashed), $\kappa_{\rm CMB} I$ correlations (blue) and the sum of the two (red). These are also similar to the plots published in Kirk et al. 2016.

7.2.4.4 Systematics in the CMB Lensing Map

In addition to the systematic uncertainties in the galaxy shear catalogue, we test for any systematic errors in the SPT-SZ lensing map. One of the key contaminations in a temperature based CMB lensing map is the tSZ effect. While we make no attempt to evaluate how the masking of the temperature map affects the reconstructed lensing map in the analysis, we conduct a simple test of applying a stronger mask post reconstruction. For the stronger mask, clusters with lower detection significances ($4.5 < {\rm S/N}_{\rm clus} < 6$) are masked in addition to the fiducial mask, which removes a $16' \times 16'$ patch around clusters detected with ${\rm S/N}_{\rm clus} > 6$. We also additionally mask point sources between $5 < {\rm S/N} < 15$ using a $2'$ radius circular aperture, in addition to the $16' \times 16'$ mask applied to sources detected with greater than ${\rm S/N} > 15$ in the main mask. With this mask applied, we obtain a best-fit amplitude of $A_{\rm E} = 0.88 \pm 0.30$ with χ^2/dof=0.98, which is

highly consistent with the fiducial results.

7.3 DES-Y1 Galaxy Density

Galaxies are useful in studying the large-scale structure since they are both abundant and sufficiently bright to be observed over cosmological distances (Mo et al., 2010). While galaxies are not perfect tracers of the underlying mass distribution, it is believed that the clustering of galaxies is linked to the clustering of underlying mass by a simple relationship given in Equation 6.3 for scales larger than the non-linear regime.

The cross-correlation between DES-SV galaxy density (using a wide redshift bin $0.2 < z < 1.2$) and SPT-SZ CMB lensing was measured in Giannantonio et al. 2016, and was detected at 6σ. Additionally, the data were divided into five redshift bins and each of the bins were correlated with CMB lensing, from which $> 2\sigma$ measurements were made for all the bins.

In this section, we conduct a similar tomographic analysis using *DES-Y1-like simulations*, and the results will be used as part of the Y1 multi-probe analysis forecast discussed in Chapter 8.

7.3.1 Data

The Y1 observations were taken between August 2013 and February 2014 (Dark Energy Survey Collaboration et al., 2016). The depth and area makes it a valuable data set to carry out tomographic lensing analyses. The Y1 footprint covers approximately 1300 deg^2 including weights, and extends beyond the SPT-SZ only lensing map that was used for cross-correlations with DES-SV data. We therefore, correlate the galaxy data with the SPT-SZ + *Planck* CMB weak lensing map presented in Chapter 4, which is a refined data product specifically produced for this purpose.

In the SV analysis, galaxies in the "benchmark" sample (see Giannantonio et al. 2016 for the full description) with magnitudes $18.0 < i_{\rm mag} < 22.5$ were used for analysis. For Y1, we use the redMaGiC galaxy sample to stay consistent with the 3×2pt project that is described in Chapter 8. redMaGiC (Rozo et al., 2016) is an algorithm that selects Luminous Red Galaxies

(LRGs) while minimizing the uncertainties in the photometric redshifts. The selection is based on how well the photometry of the galaxy matches with the red-sequence template. There are three REDMAGIC catalogues that are used in the Y1 analysis. The first catalogue is the "high-density" catalogue that covers the redshift range of $0.1 < z_{\rm redMaGiC} < 0.7$ with galaxies brighter than $L/L^* > 0.5$, where L^* is the characteristic luminosity (calculated using SDSS REDMAGIC galaxies at $z = 0.1$). The density of this catalogue is $\sim 10^{-3}$ $(h^{-1}{\rm Mpc})^{-3}$, and is primarily used as lenses in galaxy-galaxy lensing analyses. The second catalogue is the high luminosity catalogue that has a higher cut-off in $z_{\rm redMaGic}$ at 0.95 and includes galaxies that are brighter than $L/L^* > 1$. The density of this catalogue is $\sim 4 \times 10^{-4}$ $(h^{-1}{\rm Mpc})^{-3}$, and is mainly used for large-scale structure and baryonic acoustic oscillation analyses. The third catalogue is the "higher luminosity" catalogue that includes galaxies brighter than $L/L^* > 1.5$ and has a density of 1×10^{-4} $(h^{-1}{\rm Mpc})^{-3}$. We use REDMAGIC galaxies in the redshift range of $0.15 < z < 0.90$, with five tomographic bins. The first three z-bins ($0.15 < z < 0.30,\ 0.30 < z < 0.45,\ 0.45 < z < 0.60$) use the high-density sample, the fourth z-bin ($0.60 < z < 0.75$) uses the high-luminosity sample and the fifth z-bin ($0.75 < z < 0.90$) uses the higher-luminosity sample (Elvin-Poole et al., 2017). The redshift distributions of the five samples are shown in Figure 7.4. These REDMAGIC samples have redshift uncertainties of $\sigma_z = [0.014, 0.025, 0.022, 0.033, 0.028]$.

7.3.2 METHODS

We calculate the galaxy density × galaxy density ($\delta_{\rm g} \times \delta_{\rm g}$) and CMB lensing × galaxy density ($\kappa_{\rm CMB} \times \delta_{\rm g}$) two-point correlation functions using the TREECORR (Jarvis et al., 2004; Jarvis, 2015) package. For $\delta_{\rm g} \times \delta_{\rm g}$, the code calculates the Landy-Szalay estimator (Landy & Szalay, 1993):

$$\xi_\theta^{\delta_{\rm g}\delta_{\rm g}} = \frac{\left(\frac{1}{N^{DD}_{\theta_{ij}}} \sum_i \sum_j \mathcal{B}_{\theta_{ij}} - \frac{2}{N^{DR}_{\theta_{ij}}} \sum_i \sum_j \mathcal{B}_{\theta_{ij}} + \frac{1}{N^{RR}_{\theta_{ij}}} \sum_i \sum_j \mathcal{B}_{\theta_{ij}} \right)}{\frac{1}{N^{RR}_{\theta_{ij}}} \sum_i \sum_j \mathcal{B}_{\theta_{ij}}}, \tag{7.9}$$

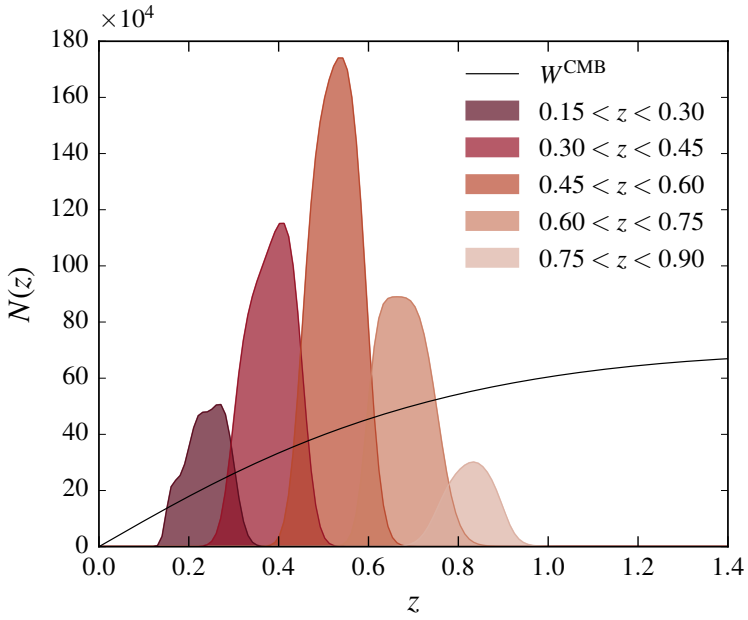

Figure 7.4 Redshift distributions of REDMAGIC lens galaxy samples. The CMB lensing kernel is also shown to illustrate the lensing efficiency as a function of redshift.

where i, j are indices that loop though the entries of the catalogues, $\mathcal{B}_{\theta_{ij}}$ is the binning function which equals 1 when the i-th and j-th galaxies are separated by $\theta + \delta\theta$ and 0 otherwise. N_θ is the number of galaxy pairs that are separated by $\theta + \delta\theta$. The superscript denotes the catalogue type that are being correlated, where D and R represent the data and random catalogues respectively. Random catalogues are generated by placing ten times the number of galaxies in the data catalogue, at random locations within the survey mask.

For $\delta_g \times \kappa_{CMB}$, TREECORR calculates:

$$\xi_\theta^{\kappa_{CMB}\delta_g} = \frac{1}{N_{\theta_{xi}}^{\kappa_{CMB}D}} \sum_x \sum_i w_x^\kappa \kappa_x \mathcal{B}_{\theta_{xi}} - \frac{1}{N_{\theta_{xi}}^{\kappa_{CMB}R}} \sum_x \sum_i w_x^\kappa \kappa_x \mathcal{B}_{\theta_{xi}} \tag{7.10}$$

where $\mathcal{B}_{\theta_{xi}}$ is now the binning function that equals 1 when the i-th galaxy and x-th *pixel coordinates* in the κ_{CMB} map are separated by $\theta + \delta\theta$ and 0 otherwise.

We compare the auto and cross-correlation measurements with our fiducial model calculated

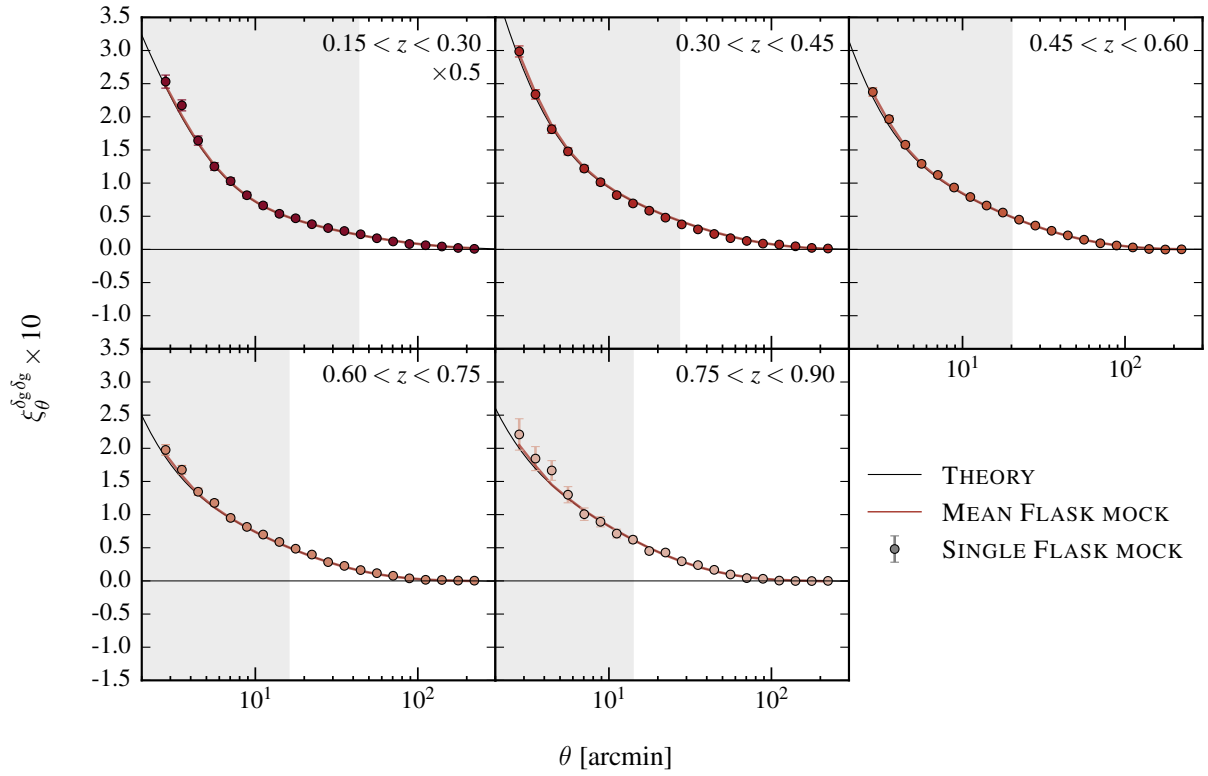

Figure 7.5 The angular auto-correlation measurement of FLASK Y1-mock REDMAGIC-like galaxies for the five individual redshift bins $0.15 < z < 0.30$, $0.30 < z < 0.45$, $0.45 < z < 0.60$, $0.60 < z < 0.75$, $0.75 < z < 0.90$. In each panel, the mean of 1200 realizations is shown as a red line, and the points are for a *single* realization. The angular scales filled in grey are excluded in the combined analysis discussed in the next chapter.

using Equations 6.4, 6.5 and 6.22:

$$\xi^{\delta_g\delta_g}_{\theta,\mathrm{fid}} = \xi^{\delta_g\delta_g}_{\theta}(b^2), \tag{7.11}$$

$$\xi^{\kappa_{\mathrm{CMB}}\delta_g}_{\theta,\mathrm{fid}} = A_{\mathrm{lens}}\xi^{\kappa_{\mathrm{CMB}}\delta_g}_{\theta}(b), \tag{7.12}$$

and search for the best-fit amplitude parameter $A^{\delta_g\delta_g} = b^2$ and $A^{\kappa_{\mathrm{CMB}}\delta_g} = bA_{\mathrm{lens}}$. We estimate the covariance matrix using 1200 lognormal FLASK realizations, and compute the best-fit ampli-

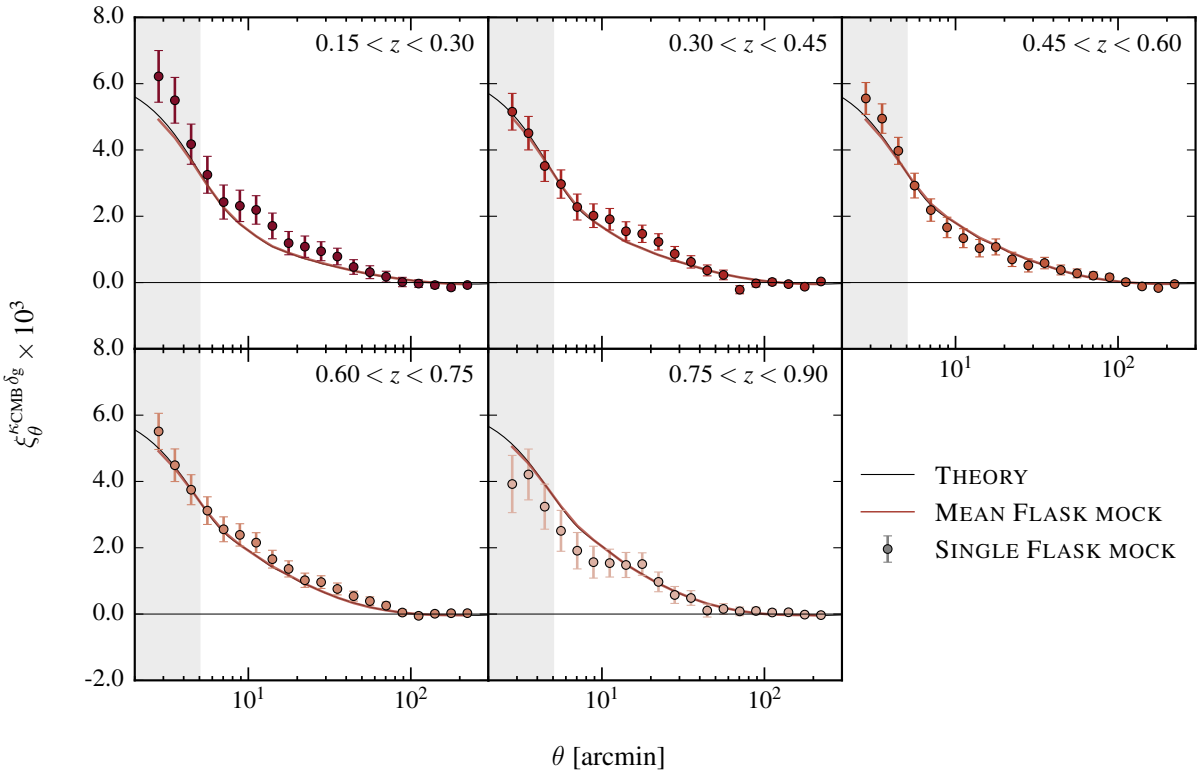

Figure 7.6 The angular cross-correlation measurement between galaxy density δ_g and CMB convergence κ_{CMB} for the five individual redshift bins.

tudes for the parameters b and $A^{\kappa_{CMB}\delta_g}$ over the tomographic bins:

$$\chi^2 = \sum_{ij} (\xi^{\alpha}_{i,\mathrm{obs}} - \xi^{\alpha}_{i,\mathrm{fid}}) \mathcal{C}^{-1}_{ij} (\xi^{\alpha}_{j,\mathrm{obs}} - \xi^{\alpha}_{j,\mathrm{fid}}), \tag{7.13}$$

where $\alpha = \{\delta_g\delta_g, \delta_g\kappa_{CMB}\}$.

7.3.3 RESULTS

The angular auto-correlation measurements made on the DES-Y1-like simulations are shown in Figure 7.5. The corresponding cross-correlation measurements are shown in Figure 7.6. The mean of the best-fit amplitudes for 1200 simulation realizations and for a single realization are summarized in Table 7.1 and the distributions of the best-fit amplitudes relative to the input values are shown in Figure 7.7. While there is scatter between the simulation realizations, the

average of 1200 simulations recover the input auto- and cross-correlation amplitudes well, deviating away by at most 1%. We obtain a signal-to-noise ratio ranging from 13σ and 37σ for the auto-correlations and between 8σ and 14σ for the cross-correlations, and expect to see similar detection significances when repeating the same measurement on the true data.

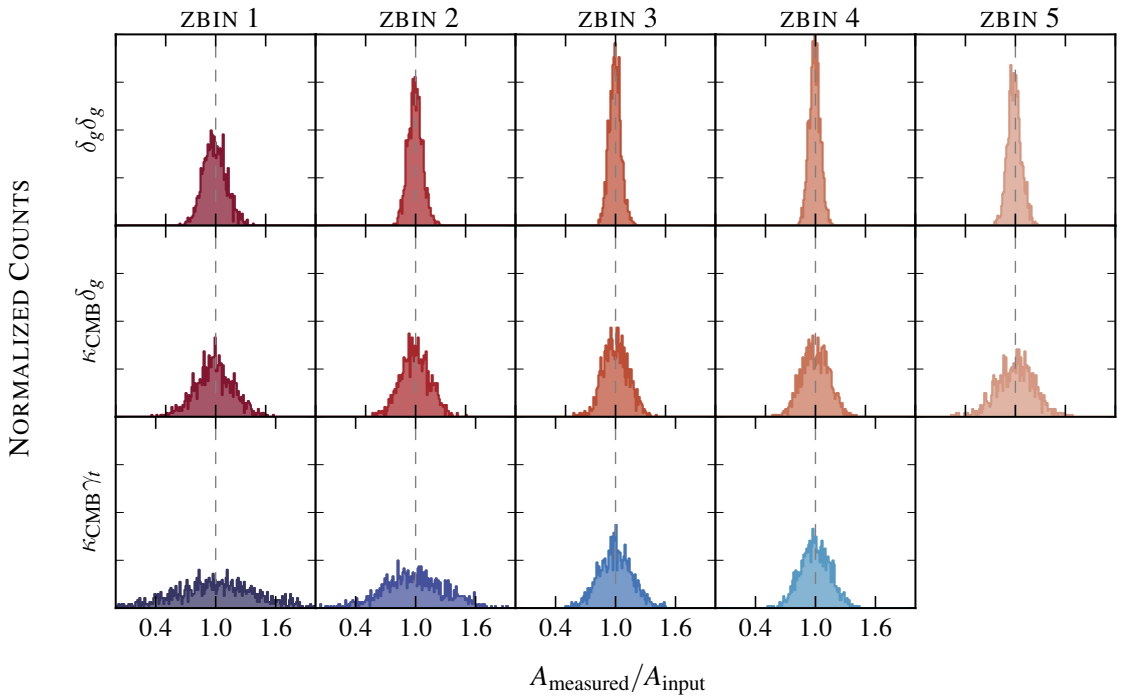

Figure 7.7 Histograms of the best-fit amplitudes relative to the input amplitudes for $\delta_{\rm g} \times \delta_{\rm g}$ (top row), $\kappa_{\rm CMB} \times \delta_{\rm g}$ (middle row), and $\kappa_{\rm CMB} \times \gamma_{\rm t}$ (bottom row) using 1200 FLASK realizations.

Measurement	$b_{\rm input}$	$\langle b \rangle$	$b_{\rm sim=1}$	$\chi^2_{\rm sim=1}/dof$ (PTE)	S/N
redMaGiC × redMaGiC					
$0.15 < z < 0.30$	1.45	1.45	1.48 ± 0.11	10.7/7 (0.15)	13
$0.30 < z < 0.45$	1.55	1.55	1.48 ± 0.07	7.7/9 (0.56)	22
$0.45 < z < 0.60$	1.65	1.65	1.66 ± 0.06	5.3/10 (0.87)	28
$0.60 < z < 0.75$	1.80	1.80	1.84 ± 0.05	11.7/11 (0.39)	37
$0.75 < z < 0.90$	2.00	2.00	2.00 ± 0.07	8.8/12 (0.72)	29

Measurement	$A^{\kappa_{\rm CMB}\delta_{\rm g}}_{\rm input}$	$\langle A^{\kappa_{\rm CMB}\delta_{\rm g}} \rangle$	$A^{\kappa_{\rm CMB}\delta_{\rm g}}_{\rm sim=1}$	$\chi^2_{\rm sim=1}/dof$ (PTE)	S/N
redMaGiC × SPT-SZ + *Planck* $\kappa_{\rm CMB}$					
$0.15 < z < 0.30$	1.45	1.44	1.58 ± 0.19	11.5/16 (0.77)	8
$0.30 < z < 0.45$	1.55	1.55	1.59 ± 0.14	31.0/16 (0.01)	11
$0.45 < z < 0.60$	1.65	1.66	1.69 ± 0.13	18.0/16 (0.32)	13
$0.60 < z < 0.75$	1.80	1.81	1.85 ± 0.13	10.9/16 (0.81)	14
$0.75 < z < 0.90$	2.00	2.01	1.66 ± 0.18	7.3/16 (0.97)	11

Table 7.1 Table summarizing the best-fit auto- and cross-correlation amplitudes for the mean of the 1200 Flask simulations and a single realization. S/N is calculated using the mean amplitude and the variance.

7.4 DES-Y1 Galaxy Weak Lensing

7.4.1 Data

The effective overlap between DES-year 1 (Y1) weak lensing data and the SPT 2500 deg^2 patch is approximately 1100 deg^2, after accounting for weights. There exists two different shape measurement pipelines for Y1 analysis: im3shape and Metacalibration.

Metacalibration is a new technique that is used to measure the weak lensing signal based solely on the imaging data, without any prior knowledge of the properties of the galaxies being measured. The method was first introduced in Huff & Mandelbaum 2017, and has been extensively tested in Sheldon & Huff 2017 using image based simulations with realistic observational complications such as stellar contamination and variations in the detection thresholds. The code is applied to the Y1 galaxy shape catalogue using r, i, z-bands. We refer the reader to the aforementioned papers for details of the calibration processes and results from applying this method on simulations as well as Zuntz et al. 2017, where the descriptions of the catalogues are given. These independent pipelines produce shape catalogues with different redshift distributions (as

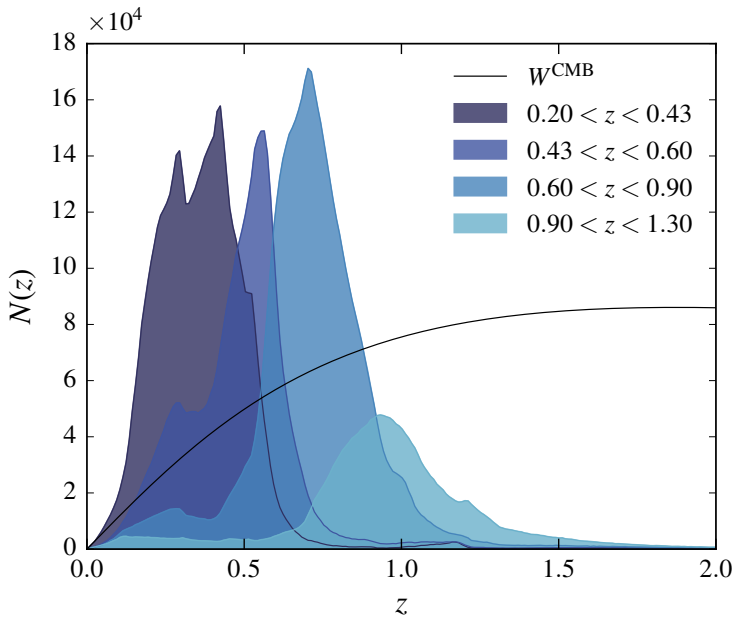

Figure 7.8 Redshift distributions for METACALIBRATION galaxy samples for the four redshift bins.

shown in Figure 7.8) and number densities. We produce our simulations based on the properties of METACALIBRATION samples, since the galaxy number densities are higher, the calibration is more stable, and are used in other analyses (Troxel et al., 2017).

7.4.2 METHODS

Redshift cuts are applied to to the full shape catalogues to extract four tomographic bins $0.2 < z < 0.43$, $0.43 < z < 0.6$, $0.6 < z < 0.9$, and $0.9 < z < 1.3$, which were determined to be optimal for galaxy-galaxy lensing and cosmic shear analyses (see e.g. Prat et al. 2017 and Troxel et al. 2017). Noise calibration bias is applied to each tomographic sample separately.

For Y1 analysis, the average correlation between CMB weak lensing and tangential shear $\xi_\theta^{\kappa_{\rm CMB}\gamma_{\rm t}}$ is calculated using the TREECORR package. Unlike the SV analysis, we make our measurements in position-space to remain consistent with all the other correlation analyses. Like with $\delta_{\rm g} \times \delta_{\rm g}$ and $\delta_{\rm g} \times \kappa_{\rm CMB}$ correlations, the covariance is calculated using 1200 FLASK realizations.

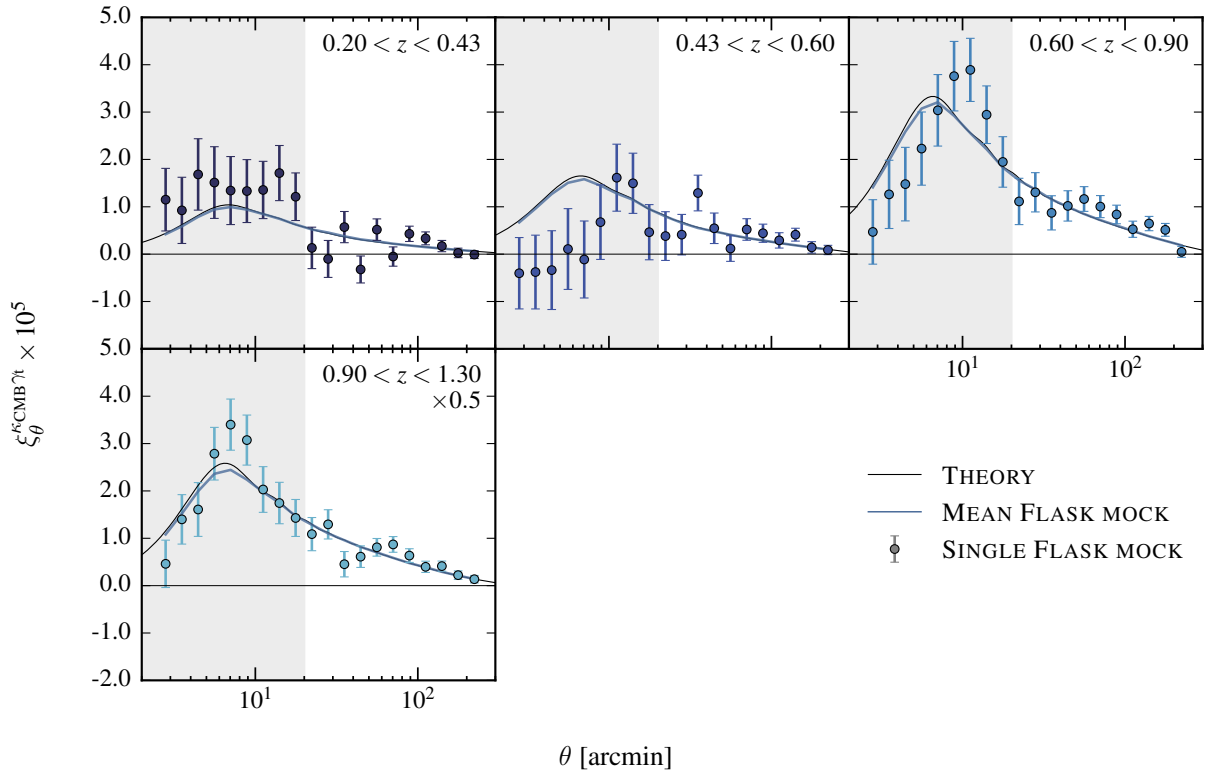

Figure 7.9 The position-space correlation between galaxy tangential shear γ_t and CMB convergence $\kappa_{\rm CMB}$ for the four individual redshift bins $0.2 < z < 0.43$, $0.43 < z < 0.6$, $0.6 < z < 0.9$, $0.9 < z < 1.3$.

7.4.3 Results

The main results are shown in Figure 7.9. The measurements that we obtain are visually noisy, and appear to fit the theoretical predictions poorly. However, this is largely due to strong correlations between the first few bin as shown in Figure 7.10. We fit a best-fit amplitude by computing:

$$\chi^2 = \sum_{ij} (\xi_{i,\rm obs}^{\kappa_{\rm CMB}\gamma_t} - \xi_{i,\rm fid}^{\kappa_{\rm CMB}\gamma_t}) \mathcal{C}_{ij}^{-1} (\xi_{j,\rm obs}^{\kappa_{\rm CMB}\gamma_t} - \xi_{j,\rm fid}^{\kappa_{\rm CMB}\gamma_t}) \tag{7.14}$$

where $\mathcal{C}^{-1}$ is the inverse covariance matrix and i, j are bin numbers. We restrict our calculation to $\theta > 20'$ since we find that the mean of 1200 realizations disagrees with the input theory correlation function at approximately 2% below this scale.

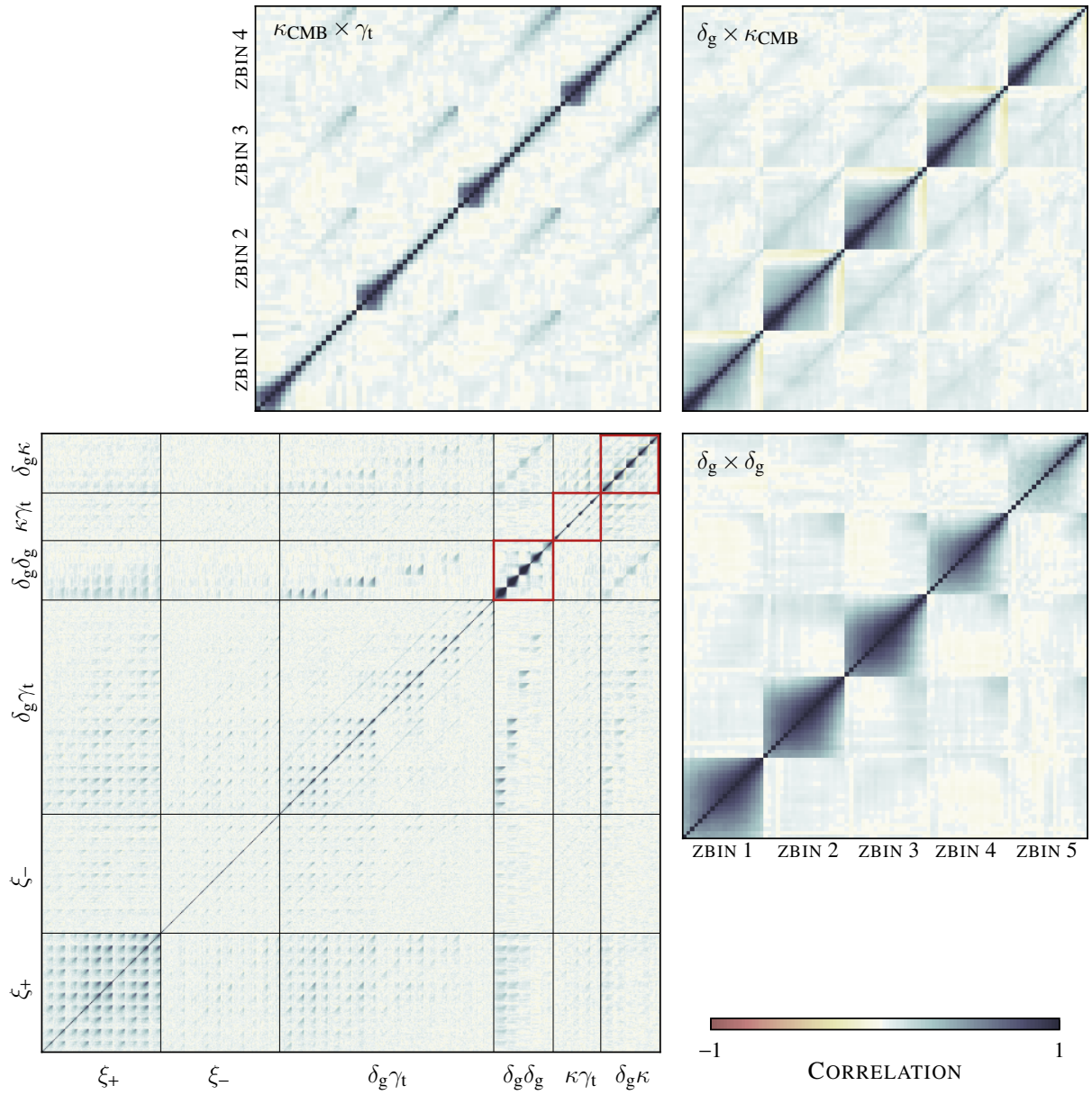

Figure 7.10 Correlation matrix for all the probes (lower left), which will be important in Chapter 8, and close-up views of the three probes ($\delta_{\rm g} \times \delta_{\rm g}$, $\kappa_{\rm CMB} \times \delta_{\rm g}$, $\kappa_{\rm CMB} \times \gamma_{\rm t}$) discussed in this chapter. Each redshift bin contains 20 angular bins in the range of $2.5' < \theta < 250'$, but not all bins are used.

Measurement	$A^{\kappa_{\rm CMB}\gamma_{\rm t}}_{\rm input}$	$\langle A^{\kappa_{\rm CMB}\gamma_{\rm t}}\rangle$	$A^{\kappa_{\rm CMB}\gamma_{\rm t}}_{\rm sim=1}$	$\chi^2_{\rm sim=1}/dof$ (PTE)	S/N
Metacalibration × SPT-SZ + *Planck* $\kappa_{\rm CMB}$					
$0.20 < z < 0.43$	1.00	1.01	0.83 ± 0.35	20.8/10 (0.02)	3
$0.43 < z < 0.60$	1.00	1.00	1.13 ± 0.26	11.4/10 (0.33)	4
$0.60 < z < 0.90$	1.00	1.00	1.10 ± 0.14	10.3/10 (0.41)	7
$0.90 < z < 1.30$	1.00	1.00	1.00 ± 0.13	12.1/10 (0.28)	8

Table 7.2 Table summarizing the cross-correlation amplitudes between $\kappa_{\rm CMB}$ and $\gamma_{\rm t}$, for the mean of 1200 Flask realizations and a single realization.

We obtain best-fit amplitudes of $A^{\kappa_{\rm CMB}\gamma_{\rm t}} = 0.83 \pm 0.35, 1.13 \pm 0.26, 1.10 \pm 0.14, 1.00 \pm 0.13$, with χ^2/dof of $20.8/10, 11.4/10, 10.3/10, 12.1/10$ for the four redshift bins, for a single realization. While the scatter is large for a single realization, we obtain mean amplitudes of $\langle A^{\kappa_{\rm CMB}\gamma_{\rm t}}\rangle = 1.01, 1.00, 1.00, 1.00$ using all 1200 realizations, which match with the input amplitude of $A^{\kappa_{\rm CMB}\gamma_{\rm t}} = 1$. The distributions of best-fit amplitudes for the 1200 realizations are shown in Figure 7.7. The signal-to-noise ratio varies from ~ 3 (lowest redshift bin) to ~ 8 (highest redshift bin).

7.5 Biases to Cross-correlations due to Foregrounds in the CMB Lensing Data

Numerous rigorous tests are carried out to validate the galaxy samples. This is especially important for shear measurements, where systematics must be controlled to at least $\mathcal{O}(\sim 1\%)$ to extract useful signal. Cross-correlations are often less prone to non-astrophysical systematics, such as issues related to the modelling of the point spread function, scan patterns and depth variations. This is particularly true for cross-correlations between different probes using separate surveys, since instrumental and observational systematics are not correlated. There are, however, astrophysical correlations which bias the cross-correlation measurements.

The 150 GHz map has emission from the primary CMB as well as astrophysical foregrounds such as tSZ and CIB. These foreground components are late time effects induced by non-linear structures; tSZ is due to inverse Compton scattering of photons by energetic gas in galaxy clusters (Carlstrom et al., 2002), and CIB is due to dusty star forming galaxies with a redshift distribution that peaks at $1<z<3$ (Viero et al., 2013). These secondary anisotropies imprint non-Gaussian signatures onto the observed sub-millimeter sky. Some of the components, such as

bright AGNs can be readily identified and removed due to their brightness. For fainter sources, the amount of contribution to the total power spectrum must be modelled, and subtracted out.

The off-diagonal terms in the covariance are generated by non-Gaussian foregrounds in addition to the lensing effect. Therefore, the reconstructed lensing map will contain some contamination. This is picked up when cross-correlating the CMB lensing map with galaxies and galaxy weak lensing, since these foreground contaminants are correlated with the large-scale structure.

tSZ bias ($\kappa_{\rm tSZ} \times \delta_{\rm g}/\kappa_{\rm E}$ correlation)

We estimate the amplitude and the shape of the bias by first creating a simulated tSZ map from the DES REDMAPPER cluster catalogue (Rykoff et al., 2014, 2016). We select clusters with richness (denoted with λ, defined as the sum of the membership probability of all the galaxies near the cluster (Rykoff et al., 2016)) greater than 20. While the most massive REDMAPPER clusters are also detected by SPT-SZ, the majority of the clusters in this sample fall below the SPT-SZ detection threshold.

From the richness measurement of the galaxy clusters, masses are estimated using the mass-richness relation given in Melchior et al. 2017:

$$M(\lambda, z) \equiv \langle M|\lambda, z\rangle = M_0 \left(\frac{\lambda}{30}\right)^{F_\lambda} \left(\frac{1+z}{1.5}\right)^{G_\lambda}, \tag{7.15}$$

where $M_0, F_\lambda, G_\lambda$ are parameters determined from fitting the model to data, λ is the richness, and z is the redshift of the galaxy cluster. Melchior et al. 2017 reports $\log_{10} M_0 = 14.371$, $F_\lambda = 1.12$, $G_\lambda = 0.18$ as their best-fit values. However, we increase the amplitude of this relation by 1σ to obtain an upper limit of the tSZ power. Using these mass estimates, we convert to temperature decrement using:

$$\frac{\Delta T(\vec{\theta}, M, z)}{T_{\rm CMB}} = g_\nu y(\vec{\theta}, M, z) \tag{7.16}$$

$$= g_\nu \frac{\sigma_T}{m_{\rm e} c^2} \int_{\rm LOS} dl P_{\rm e}(\sqrt{l^2 + d_{\rm A}^2 |\vec{\theta}|^2}, M, z), \tag{7.17}$$

where σ_T is the Thomson cross-section, m_e is the electron mass, and the term in the integral is the electron pressure (l is the line of sight distance, d_A is the angular diameter distance and $\vec{\theta}$ is the angular separation relative to the cluster centre). For a fully ionized medium, the electron pressure is $P_\mathrm{e} = 2 \times P_\mathrm{th}(X_\mathrm{H}+1)/(5X_\mathrm{H}+3)$, where P_th is the thermal pressure and $X_\mathrm{H} = 0.76$ is the primordial hydrogen mass fraction. We employ the Battaglia et al. 2012 profile for P_th:

$$\frac{P_\mathrm{th}(x)}{P_{200,\mathrm{c}}(M_{200,\mathrm{c}},z)} = P_0(M_{200,\mathrm{c}},z)\frac{(x/x_\mathrm{c})}{[1+(x/x_\mathrm{c})]^{\beta(M_{200,\mathrm{c}},z)}}, \qquad x \equiv r/r_{200,\mathrm{c}} \tag{7.18}$$

where $M_{200,\mathrm{c}}$ denotes the total mass enclosed in a region with density 200 times the critical density (obtained from 7.15) and $r_{200,\mathrm{c}} = \left(\frac{M_{200,\mathrm{c}}}{\frac{4}{3}\pi\rho_\mathrm{crit}200}\right)^{1/3}$. $P_{200,\mathrm{c}}$, P_0, x_c and β depend on the mass and redshift of the individual clusters, and the form is fitted using simulations (Battaglia et al., 2012; Hill & Pajer, 2013):

$$P_{200,\mathrm{c}}(M_{200,\mathrm{c}},z) = \frac{200GM_{200,\mathrm{c}}\rho_\mathrm{crit}(z)\Omega_\mathrm{b}}{2\Omega_m r_{200,\mathrm{c}}} \tag{7.19}$$

$$P_0(M_{200,\mathrm{c}},z) = 18.1\left(\frac{M_{200,\mathrm{c}}}{10^{14}M_\odot}\right)^{0.154}(1+z)^{-0.758}, \tag{7.20}$$

$$x_\mathrm{c}(M_{200,\mathrm{c}},z) = 0.497\left(\frac{M_{200,\mathrm{c}}}{10^{14}M_\odot}\right)^{-0.00865}(1+z)^{0.731} \tag{7.21}$$

$$\beta(M_{200,\mathrm{c}},z) = 4.35\left(\frac{M_{200,\mathrm{c}}}{10^{14}M_\odot}\right)^{0.0393}(1+z)^{0.415}. \tag{7.22}$$

Using these equations, we model the temperature decrement around redMaGiC clusters with $\lambda > 20$, and apply the lensing reconstruction procedure to generate a κ_tSZ map, which is an estimate of the tSZ bias in the SPT-SZ $\times$ *Planck* lensing map due to galaxy clusters that do not reach SPT-SZ's detection threshold. A mask that removes circular regions of $R = 5'$ centred at redMaPPer clusters with $\lambda > 80$ is applied to this map and is then cross-correlated with galaxy density and galaxy weak lensing maps. The results are shown as coloured points in Figure 7.11. For $\kappa_\mathrm{CMB} \times \delta_\mathrm{g}$ cross-correlations, the tSZ bias is found to be strongest for the lower redshift bins and tends to decrease towards higher redshifts. This tSZ redshift evolution trend agrees with the measurements in works such as Hurier et al. 2014. The bias has a characteristic shape that is

negative at scales $L < 2000$, and is positive for scales $L > 2000$. The cross-correlations between $\kappa_{\rm tSZ} \times \kappa_{\rm E}$[‡] are also negative but significantly smaller in amplitude. We fit a function to these biases in Chapter 8 and incorporate this effect in the theoretical modelling.

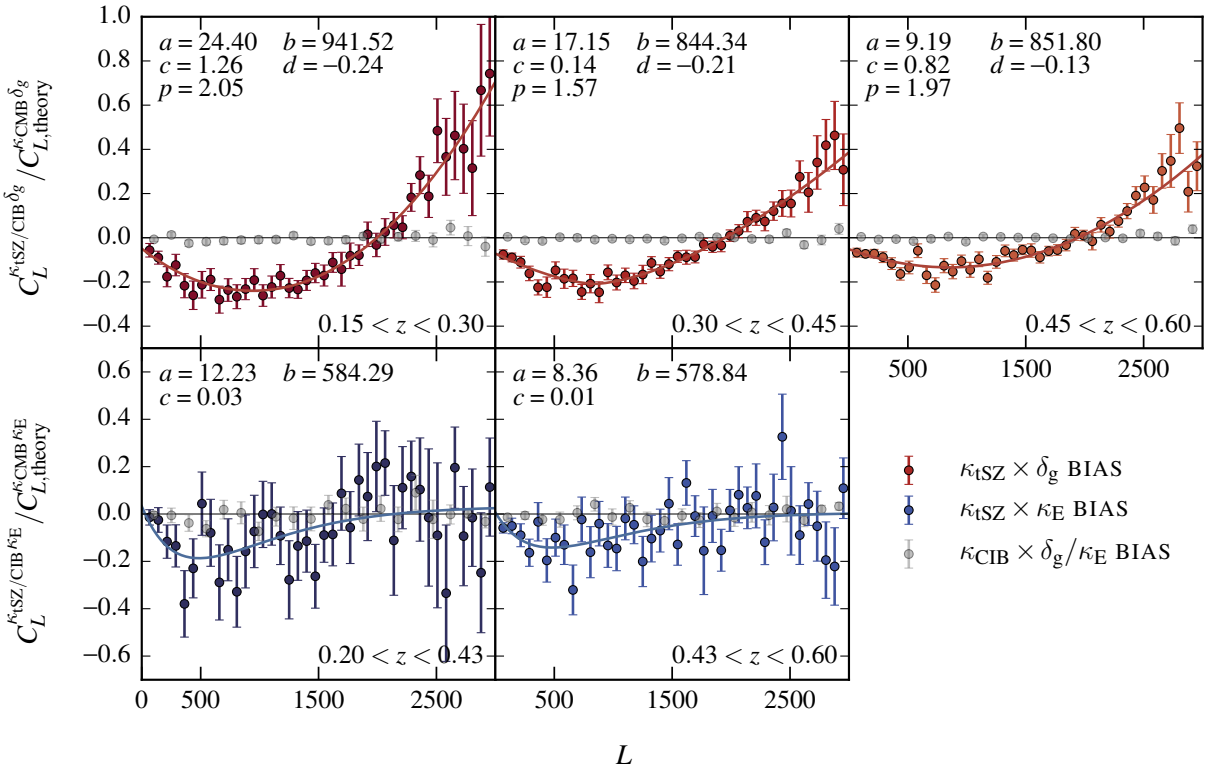

Figure 7.11 The ratio of bias to input signal ($C_L^{\kappa_{\rm tSZ/CIB}\delta_{\rm g}}/C_L^{\kappa_{\rm CMB}\delta_{\rm g}}, C_L^{\kappa_{\rm tSZ/CIB}\kappa_{\rm E}}/C_L^{\kappa_{\rm CMB}\kappa_{\rm E}}$). Equations 8.4 and 8.5 are fit to each $C_L^{\kappa_{\rm tSZ/CIB}\delta_{\rm g}}/C_L^{\kappa_{\rm CMB}\delta_{\rm g}}$ and $C_L^{\kappa_{\rm tSZ/CIB}\kappa_{\rm E}}/C_L^{\kappa_{\rm CMB}\kappa_{\rm E}}$ ratio, and the fits are used in Equation 8.6 to compute the biased cross-spectra for each probe and redshift bin. The error bars shown are calculated using the block jackknife method. Biases are not calculated for redshift bins that involve galaxies $z > 0.6$ since the REDMAPPER catalogue is not complete at those redshifts. We instead employ the fits for the last redshift below $z = 0.6$ and consider the biases as upper limits (since the biases are expected to be smaller for higher redshifts, as it can be seen from the plot).

CIB bias ($\kappa_{\rm CIB} \times \delta_{\rm g}/\kappa_{\rm E}$ correlation):

To quantify the $\kappa_{\rm CIB} \times \delta_{\rm g}/\kappa_{\rm E}$ bias, we utilize the $\kappa_{\rm CIB}$ map presented in Section 5.3. The corre-

[‡]The modelling is done in harmonic-space and hence $\kappa_{\rm E}$ is used instead of $\gamma_{\rm t}$.

lation between DES galaxies and CIB is expected to be small since the CIB is mostly composed of dusty sub-millimeter galaxies peaking at $z \sim 2$, whereas the distribution of DES galaxies peaks at $z \sim 0.7$. This is confirmed by cross-correlating $\delta_{\rm g}$ and $\kappa_{\rm E}$ with $\kappa_{\rm CIB}$, for which the results are shown as grey points in Figure 7.11. We find that the cross-correlation measurements are noisier than that of $\kappa_{\rm tSZ} \times \delta_{\rm g}/\kappa_{\rm E}$ and no strong evidence of bias is found.

8

Multi-Probe Analysis

One of the key goals of measuring the cross-correlations between CMB weak lensing, galaxy density and galaxy weak lensing is to combine the measurements to attain the most stringent cosmological constraints. Forecasts in the literature show that adding CMB cross-correlation measurements improve the constraints on σ_8, sum of neutrino masses $\sum m_\nu$, galaxy bias and shear calibration bias relative to galaxy surveys alone (Vallinotto, 2012; Das et al., 2013; Pearson & Zahn, 2014; Liu et al., 2016; Schaan et al., 2016). Recently, multiple studies have attempted to perform a joint analysis of three cosmological probes from galaxy surveys (van Uitert et al., 2017), and also with CMB lensing, using data (Nicola et al. 2017; Doux et al. 2017). Such multi-probe analyses are expected to become extremely powerful in the coming era (Schaan et al., 2016). Combining DES and SPT will be the first study to include *tomographic* measurements of cosmic shear, galaxy-galaxy lensing, CMB lensing-galaxy density and CMB lensing-galaxy lensing correlations, with the source and lens galaxy samples from the same survey. This will have considerable statis-

tical power relative to non-tomographic measurements (Hu, 1999; Hildebrandt et al., 2017), and will be self-consistent in terms of data reduction procedures.

The DES collaboration internally combined measurements of galaxy clustering ($\delta_g \times \delta_g$), galaxy-galaxy lensing ($\delta_g \times \gamma$) and cosmic shear ($\gamma \times \gamma$) using the five lens and four source redshift bins (Krause et al., 2017; DES Collaboration et al., 2017). It was shown that the constraints from DES-Y1 data are comparable to the constraints found by *Planck*, and therefore, our understanding of the early and late universe can be on placed on equal footing (DES Collaboration et al., 2017). The combined measurement involves three two-point correlation measurements, $\delta_g \times \delta_g$, $\delta_g \times \gamma_t$, $\gamma \times \gamma$ (although $\gamma \times \gamma$ is separated into ξ_-/ξ_+, and there are 45 different measurements including all the tomographic bins), and is therefore referred to as "3×2pt".

Since the SPT footprint overlaps with DES, 3×2pt could be extended to include the cross-correlations with CMB lensing. Using SPT-SZ +*Planck* × DES-Y1 FLASK simulated data, we measure all the two-point correlation functions and forecast the constraints that we will obtain by combining all the results. We will refer to this as "5×2pt" (since we are using five two-point correlation measurements).

8.1 METHODS

Obtaining parameter constraints from a *tomographic* multi-probe analysis is challenging due to the vast number of data vectors and the elements in the covariance matrix which must be evaluated. We estimate the full covariance using the 1200 lognormal FLASK simulations presented in Chapter 7.1 with realistic noise estimates and masks applied. Measurements for $\delta_g \times \delta_g$, $\kappa_{CMB} \times \delta_g$, $\kappa_{CMB} \times \gamma_t$ were presented in Chapter 7.1, but the additional correlations ($\delta_g \times \gamma_t$, ξ_-, ξ_+) are also measured. For simplicity, the input fiducial spectrum is treated as the data vector (which we refer to as the theory data vector), while the covariance is constructed from the measurements made on FLASK realizations.

8.2 Likelihood Calculation

The publicly available code CosmoSIS[*] (Zuntz et al., 2015) is utilized to calculate the cosmological parameter constraints. Within CosmoSIS, the internal DES libraries and the relevant modules built specifically for DES×SPT cross-correlations are used. We let the cosmological parameters $\Omega_{\rm m}, h_0, \Omega_{\rm b}, n_{\rm s}, A_{\rm s}$ vary in the ranges listed in Table A.2 and fix the other cosmological parameters. The list of nuisance parameters being considered in the likelihood calculations are also summarized in Table A.2, and we give brief descriptions of each of these below.

Photometric redshift bias

The redshift distribution of galaxies affects the amplitude and the shape of the fiducial spectrum. The uncertainty of the redshift distribution is modelled as a single shift parameter in the galaxy distribution:

$$n_i^l(z) = \hat{n}_i^l(z - \Delta_i^l) \qquad i \in \{1,2,3,4,5\}, \tag{8.1}$$

$$n_i^{\rm s}(z) = \hat{n}_i^{\rm s}(z - \Delta_i^{\rm s}) \qquad i \in \{1,2,3,4\}, \tag{8.2}$$

where i is an index for the redshift bin, $\hat{n}_i^l$, $\hat{n}_i^{\rm s}$ are the estimated photometric redshift distributions, and Δ_i^l, $\Delta_i^{\rm s}$ are the photometric redshift biases for the lens and source samples respectively. These parameters are varied independently for the five lens and four source redshift bins.

Linear galaxy bias

Galaxy bias b_i is a multiplicative function that directly affects the amplitude and shape of galaxy auto- and cross-correlations. Under the assumption of *linear* galaxy bias (i.e. scale-independent) galaxy bias is a multiplicative constant, which is directly degenerate with the correlation amplitude and hence with combinations of σ_8 and $\Omega_{\rm m}$. Therefore, these parameters must be varied simultaneously. A measurement that involves the galaxy density field will inevitably contain this bias; the amplitude of galaxy clustering measurements (galaxy auto-correlation) is proportional

[*] https://bitbucket.org/joezuntz/cosmosis/wiki/Home

to b_i^2, and galaxy-galaxy lensing, galaxy-$\kappa_{\rm CMB}$ correlations are proportional to b_i. Although we assume a simple linear galaxy bias model in this forecast, higher order terms are currently being implemented.

Shear calibration bias

Multiplicative shear bias arises from the mismatch between the inferred and the true underlying shear signal, which can be parametrized by a single multiplicative factor $(1 + m_i)$, where i is an index for the redshift bin. Calibration errors result from failures in the shear measurement method itself, stellar contamination in the galaxy sample, false object detection and selection bias (Heymans et al., 2006). The amplitude of galaxy-galaxy lensing and $\kappa_{\rm CMB} \times \gamma_{\rm t}$ correlations are proportional to $(1 + m_i)$, and cosmic shear correlations are proportional to $(1 + m_i)(1 + m_j)$. Similar to the linear galaxy bias, these parameters are varied independently for the four source redshift bins.

Intrinsic alignment

The non-linear alignment model given in Equation 6.10 is employed to capture the effect of intrinsic alignment. The basic form is slightly modified to additionally capture the redshift evolution:

$$-C_1\rho_{\rm crit}\frac{\Omega_{\rm m}}{D_\chi}n^{\rm s}(\chi) \rightarrow -A^{\rm IA}\left(\frac{1+z}{1+z_0}\right)^{\alpha^{\rm IA}} C_1\rho_{\rm crit}\frac{\Omega_{\rm m}}{D_\chi}n^{\rm s}(\chi). \tag{8.3}$$

Following Krause et al. 2017, we use the values $z_0 = 0.62$, $C_1\rho_{\rm crit} = 0.0134$ and let $A^{\rm IA}$ and $\alpha^{\rm IA}$ vary.

tSZ/CIB biases

We ignore the CIB bias in this section, as it has been shown in Section 7.5 that the contamination is negligible. The $\kappa_{\rm tSZ} \times \delta_{\rm g}$ bias is modelled by fitting a function of the form:

$$y(L) = a(|(L - b)/c|)^p \times 10^{-8} + d \tag{8.4}$$

to the ratio $C_L^{\kappa_{\rm tSZ}\times\delta_{\rm g}}/C_{L,\rm fid}^{\kappa_{\rm CMB}\times\delta_{\rm g}}$ [†] for each redshift bin, where a, b, c, d, p are free parameters obtained by fitting the model to the measurements. Similarly, a function of the form:

$$y(L) = -aL\exp(-(L/b))^{1.2} \times 10^{-4} + c \tag{8.5}$$

is fit to $C_L^{\kappa_{\rm tSZ}\times\kappa_{\rm E}}/C_{L,\rm fid}^{\kappa_{\rm CMB}\times\kappa_{\rm E}}$. The measurements and the fits for the various redshift bins are shown in Figure 7.11, and the best-fit parameters are tabulated in Table 8.1. The biased cross-spectrum is written in terms of a scaling constant $A_{\rm tSZ}$, the fitted function $y(L)$, and the unbiased spectrum $C_{L,\rm fid}^{\kappa_{\rm CMB}\alpha,\rm unbiased}$:

$$C_{L,\rm fid}^{\kappa_{\rm CMB}\alpha,\rm biased} = [1 + A_{\rm tSZ}^2 y(L)]C_{L,\rm fid}^{\kappa_{\rm CMB}\alpha,\rm unbiased} \tag{8.6}$$

where $\alpha = \{\delta_{\rm g}, \kappa_{\rm E}\}$. Rather than varying the amplitude of this bias, we set $A_{\rm tSZ} = 1$ and investigate the angular scales at which the bias impacts the constraints the most, and remove those scales from the analysis. We run two types of likelihood calculations: one with tSZ bias convolved in the theory data vector, and one without. We run each of these calculations with minimal cuts (using $\theta > 5'$ for $\kappa_{\rm CMB} \times \delta_{\rm g}$ and $\theta > 20'$ for $\kappa_{\rm CMB} \times \gamma_{\rm t}$, which are the angular scales for which we trust the FLASK covariance as shown in Sections 7.3 and 7.4) and conservative cuts. The conservative cuts are chosen such that all angular bins with $|\xi_\theta^{\rm biased} - \xi_\theta^{\rm unbiased}|/\sigma > 0.3$ (where σ is the standard deviation for a particular bin, calculated from FLASK simulations) are removed, as illustrated in Figure 8.1.

[†]The motivation for this is purely computational – as it reduces the time to load a file.

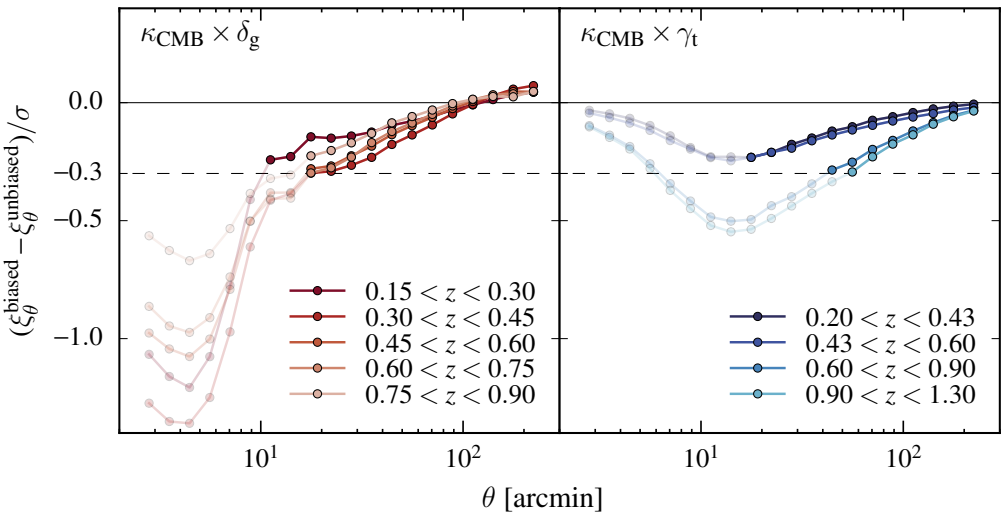

Figure 8.1 Scale cuts used in the analysis. For "minimal cuts", we remove angular bins smaller than $5'$ for $\kappa_{\rm CMB} \times \delta_{\rm g}$ and $20'$ for $\kappa_{\rm CMB} \times \gamma_{\rm t}$. For "conservative cuts", we additionally remove all angular bins where the difference between the biased and unbiased theory correlation functions are greater than 0.3σ (shown as faint points). This results in removing angular bins smaller than $[10.4', 17.7', 17.7', 16.9', 14.3']$ for $\kappa_{\rm CMB} \times \delta_{\rm g}$ and $[20.0', 20.0', 54.0', 42.0']$ for $\kappa_{\rm CMB} \times \gamma_{\rm t}$.

8.3 Results

In Figure 8.2, the constraints on $\Omega_{\rm m}$ and $S_8 = \sigma_8(\Omega_{\rm m}/0.3)^{0.5}$ obtained for the different test cases are shown. We observe that the tSZ bias does have a significant impact on the results if left untreated (blue contours in the left panel). Specifically, the inferred value of S_8 is shifted towards a lower value, and $\Omega_{\rm m}$ is shifted towards a slightly higher value at the level of $\sim 1.4\sigma$ and $\sim 0.4\sigma$ respectively. We find that the effect can be mitigated by applying the conservative scale cuts (teal contours in the left panel) reducing the shift to $\sim 0.3\sigma$ in S_8 and 0.04σ in $\Omega_{\rm m}$. However, by applying these scale cuts, we also lose signal, and our constraining power is weakened, as shown in the right panel. Nonetheless, the constraints that we obtain are slightly tighter than that of 3×2pt.

Similar conclusions can be drawn for the other parameters as shown in Figures 8.3 and 8.4. We find that the best-fit values for b_3, m_3 and $\Delta_3^{\rm s}$ (and also for the other redshift bins as shown

Redshift bin	a	b	c	d	p
$\kappa_{\rm tSZ} \times \delta_{\rm g}$					
$(0.15 < z < 0.30)$	24.40	941.52	1.26	−0.24	2.05
$(0.30 < z < 0.45)$	17.15	844.34	0.14	−0.21	1.57
$(0.45 < z < 0.60)$	9.19	851.80	0.82	−0.13	1.97
$(0.60 < z < 0.75)$	$''$	$''$	$''$	$''$	$''$
$(0.75 < z < 0.90)$	$''$	$''$	$''$	$''$	$''$
$\kappa_{\rm tSZ} \times \kappa_{\rm E}$					
$(0.20 < z < 0.43)$	12.23	584.29	0.03		
$(0.43 < z < 0.60)$	8.36	578.84	0.01		
$(0.60 < z < 0.90)$	$''$	$''$	$''$		
$(0.90 < z < 1.30)$	$''$	$''$	$''$		

Table 8.1 Table summarizing the best-fit parameters for fitting $y(L) = a(|(L-b)/c|)^p \times 10^{-8} + d$ to $C_L^{\kappa_{\rm tSZ}\delta_{\rm g}}/C_L^{\kappa_{\rm CMB}\delta_{\rm g}}$ and $y(L) = -aL\exp(-(L/b))^{1.2} \times 10^{-4} + c$ to $C_L^{\kappa_{\rm tSZ}\kappa_{\rm E}}/C_L^{\kappa_{\rm CMB}\kappa_{\rm E}}$. For $\kappa_{\rm tSZ} \times \delta_{\rm g}$, the fit for the $0.45 < z < 0.60$ redshift bin is also used for the fourth and fifth redshift bins since the redMaPPer catalogue is not complete at $z > 0.6$. Similarly for $\kappa_{\rm tSZ} \times \kappa_{\rm E}$, the fit for $0.43 < z < 0.60$ is used for the third and fourth redshift bin.

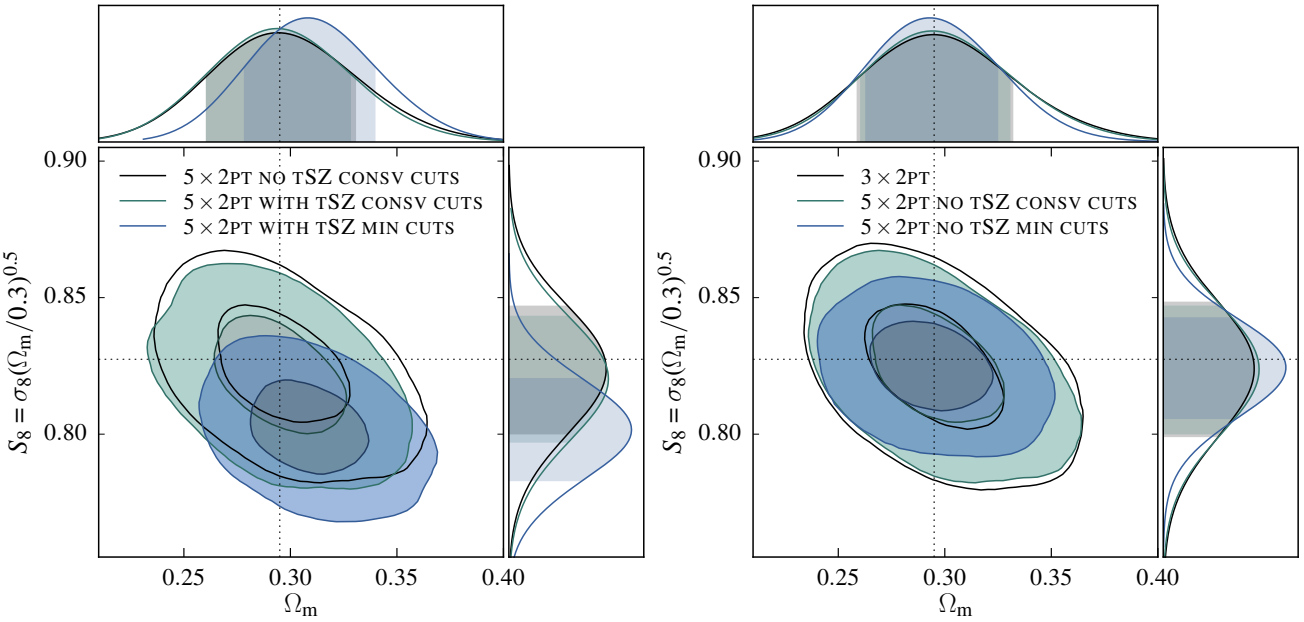

Figure 8.2 **Left:** Constraints on $\Omega_{\rm m}$ and $S_8 = \sigma_8(\Omega_{\rm m}/0.3)^{0.5}$ for 5×2pt with or without the tSZ bias effect included in the theory data vector and with minimal or conservative scale cuts applied. **Right:** comparing the constraints that we obtain from 5×2pt without tSZ bias using conservative scale cuts (teal), 5×2pt without tSZ bias and with minimal scale cuts (blue) and 3×2pt using galaxies only (black). We see marginal improvements in constraining $\Omega_{\rm m}$ and S_8. In each panel, the inner and outer contours represent the 68% and the 95% confidence intervals.

in Figure A.1) are shifted towards a higher value, but we recover (to within 0.3σ) the unbiased case when the conservative cuts are used.

These results show that we are able to gain subtle improvements in the cosmological parameter constraints by adding CMB weak lensing cross-correlations to the 3×2pt analysis, provided that systematic errors are handled with care. Although only the tSZ bias is considered here, other effects such as baryonic feedback, breakdown of linear galaxy bias, redshift evolution of galaxy bias and redshift space distortions could also impact the measurements. We leave these considerations for future work.

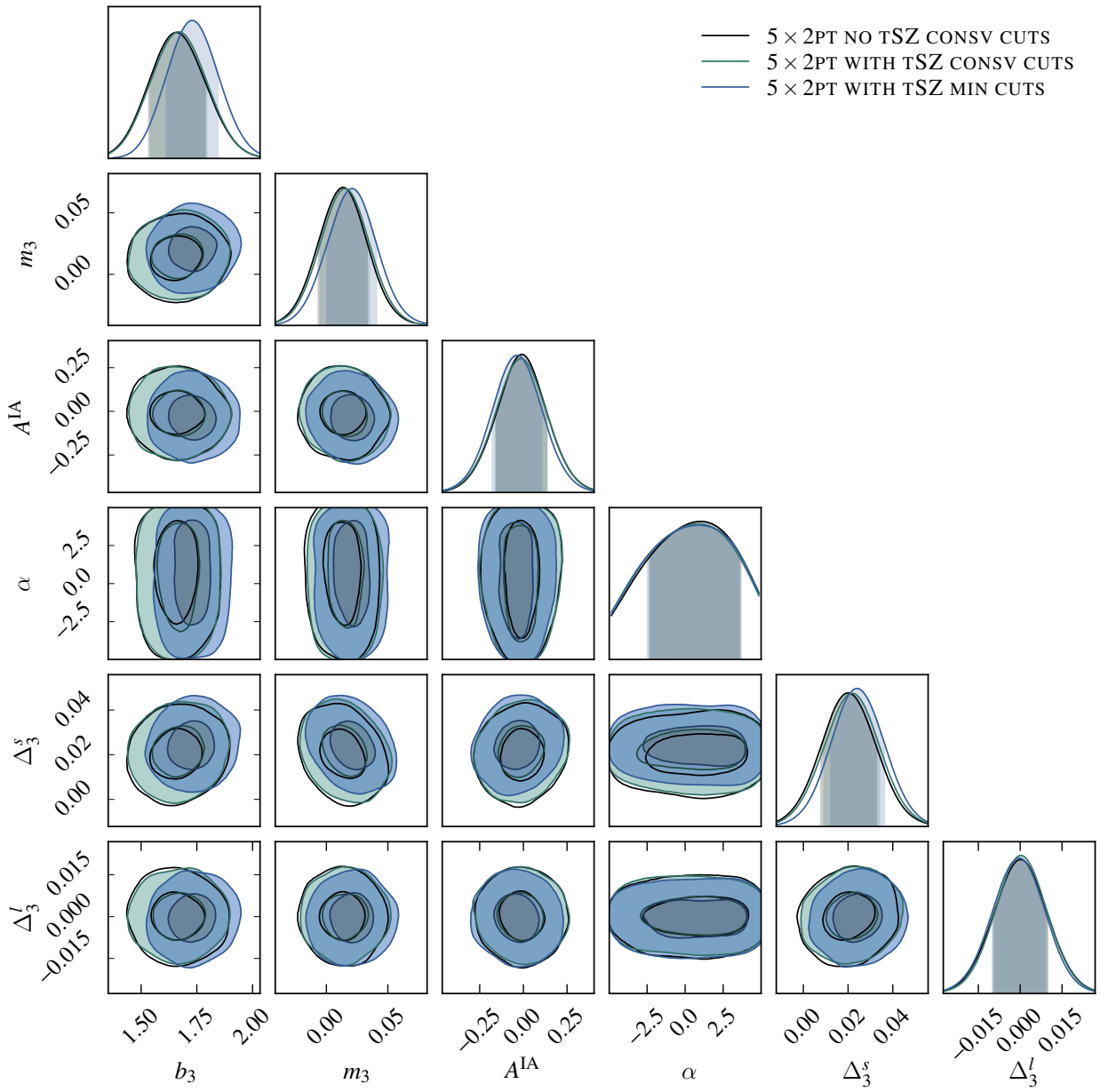

Figure 8.3 Constraints on b_3, m_3, $A^{\rm IA}$, α, $\Delta_3^{\rm s}$, Δ_3^l for 5×2pt without tSZ bias and with conservative scale cuts (black), 5×2pt with tSZ bias and conservative scale cuts (teal) and 5×2pt with tSZ bias and minimal scale cuts (blue). Here we only show results for the third redshift bin (for all the other redshift bins see Figure A.1).

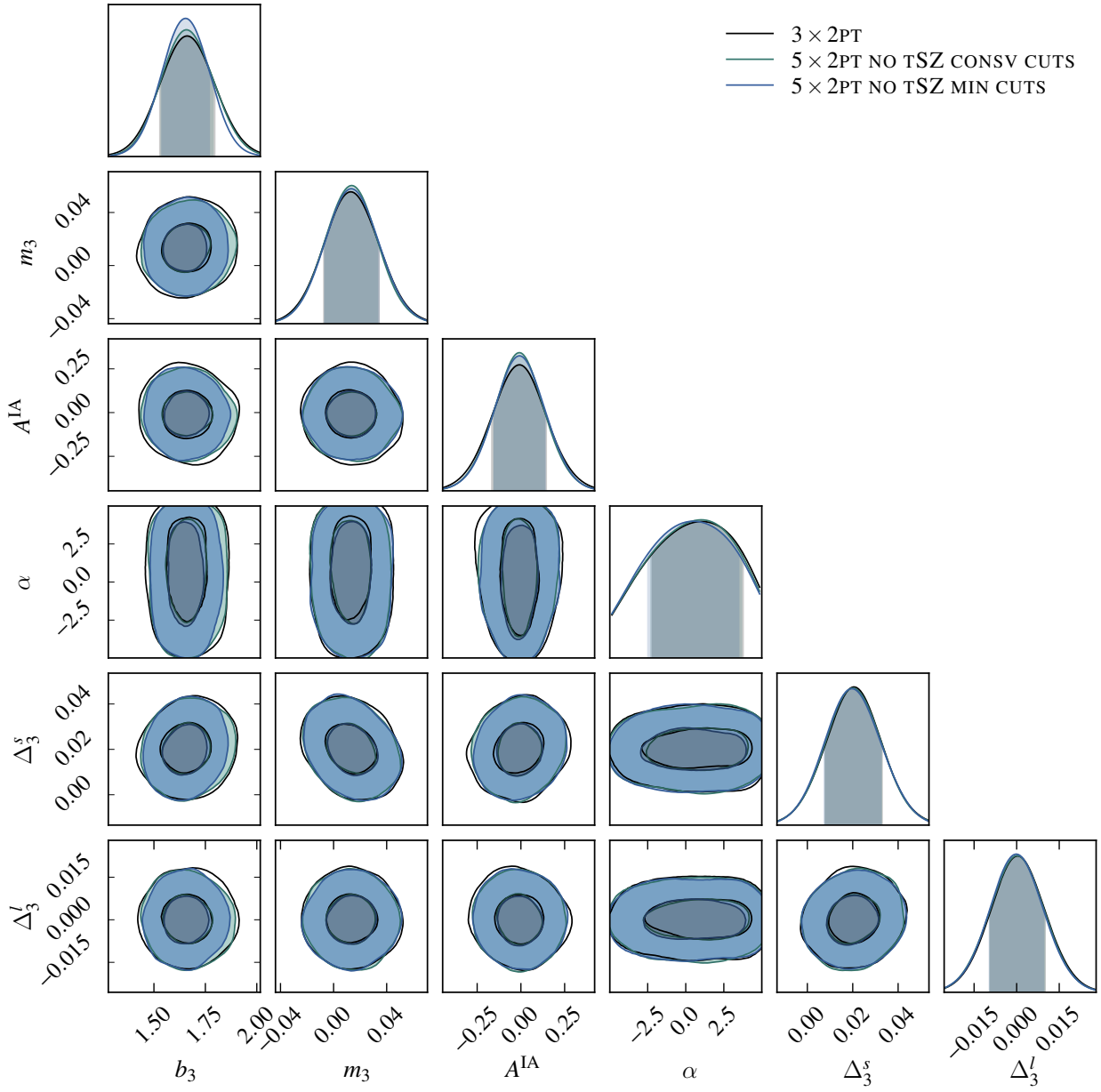

Figure 8.4 Constraints on b_3, m_3, $A^{\rm IA}$, α, $\Delta_3^{\rm s}$, Δ_3^l for 3×2pt (black), 5×2pt without tSZ bias and with conservative scales cuts (teal) and 5×2pt without tSZ bias and with minimal scales cuts (blue). We see marginal improvements in b_3 and $A^{\rm IA}$ when adding the cross-correlations with the CMB. The results for all the parameters are shown in Figure A.2.

9

Future Data and Prospective Work

Cross-correlations between CMB lensing and the large-scale structure have become increasingly popular in the past decade due to the improvement in the signal-to-noise ratio of the CMB lensing maps and the increased cosmological volume covered by galaxy surveys. In the previous chapters, the current state-of-the-art measurements from SPT-SZ + *Planck* and DES-Y1-like simulations have been presented. In this chapter, we forecast the noise levels of these surveys in the coming years (DES-Y1/Y3 data is planned to be released in December 2017, and DES-Y5 data will be released in 2019), and predict the cosmological constraints that we will obtain using these data sets.

9.1 SPT-3G and DES-Y5

SPT-3G was deployed in the winter season of 2016 and is planned to observe for four years. The camera has $\sim$15000 detectors, and is planned to cover 2500 deg^2 down to a noise level of $3.5/\sqrt{2}$

and 3.5 μK-arcmin in temperature and polarization respectively at 150 GHz. The 95 and 220 GHz channels will observe down to a noise level of $\sim 6/\sqrt{2}$ μK-arcmin and ~ 6 μK-arcmin for temperature and polarization respectively (Benson et al., 2014). By having multiple frequencies observing the same patch of the sky, we are able to separate out the various foreground components, since their emission characteristics are different in the three frequency channels. This requires all three frequency channels to be low in noise; component separated maps are produced by taking combinations of the raw frequency maps and hence including a channel with excess noise degrades all the output maps. For SPT-SZ, the high noise in the 220 GHz channel made it challenging to separate CMB, tSZ and dust. With the noise level of SPT-3G, these maps are producible and will be used in various analyses (e.g. lensing reconstruction on a tSZ free CMB map, tSZ cross-correlated with galaxies or clusters).

DES will also complete its nominal five-year observing campaign in 2018. The depth will approximately reach 24$^{\text{th}}$ magnitude (10σ limits in $1.5''$ apertures assuming $0.9''$ seeing for faint extended sources) in *griz* filters over 5000 deg^2 and is expected to observe 300 million galaxies with photometric redshifts, of which 200 million will have shape measurements (The Dark Energy Survey Collaboration, 2005; Dark Energy Survey Collaboration et al., 2016). The DES-Y5 footprint covers almost all of the SPT 2500 deg^2 nominal region as well as the stripe-82 region as shown in Figure 9.1.

9.1.1 Forecast: DES-Y5 galaxies

The true redshift distribution of the source galaxies is modeled using the functional form (Foreman et al., 2016):

$$n(z) \propto z^{\alpha} \exp\left[-\left(\frac{z}{z_0}\right)^{\beta}\right], \tag{9.1}$$

and we use the values $\alpha = 1.75, z_0 = 0.25, \beta = 1.0$. We further take in account for the uncertainties in the measured redshift by assuming a Gaussian spread:

$$p(z_{\rm p}|z) = \frac{1}{\sqrt{2\pi\sigma_z^2}} \exp\left[-\frac{(z_{\rm p} - z - \Delta_z)^2}{2\sigma_z^2}\right], \tag{9.2}$$

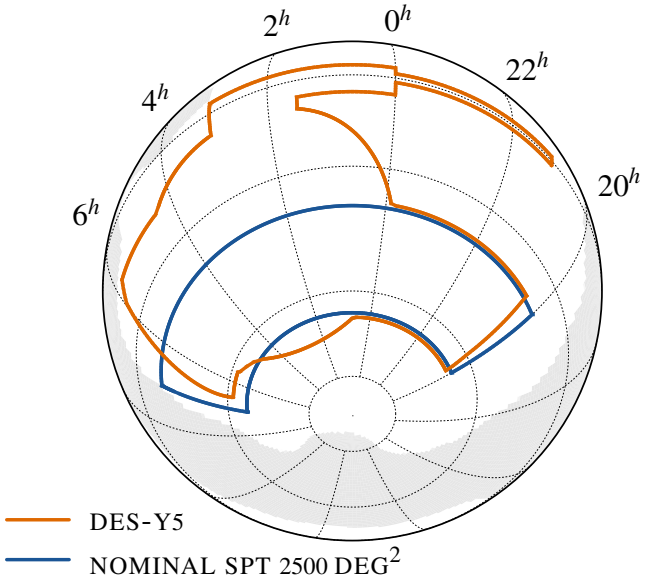

Figure 9.1 **Blue:** SPT nominal 2500 deg^2 footprint, **Orange:** DES-Y5 footprint.

where $p(z_{\rm p}|z)$ denotes the probability of measuring $z_{\rm p}$ for a galaxy with a true redshift z, σ_z is the scatter or spread in the distribution, and Δ_z is the photo-z bias. The true source galaxy distribution is first divided into four redshift bins $0.20 < z < 0.43$, $0.43 < z < 0.60$, $0.60 < z < 0.90$, $0.90 < z < 1.30$. Secondly, a $z_{\rm p}$ drawn randomly from Equation (9.2) is assigned to each galaxy based on its true redshift z. Finally, galaxies that fall in a particular redshift bin are selected based on $z_{\rm p}$, and their true redshift are retrieved. The total number of galaxies is set to 10 galaxies/arcmin^2 (Kirk et al., 2016), and each of the tomographic bins are scaled accordingly. This results in average galaxy densities of 3.39, 2.43, 2.79, 1.40 galaxies/arcmin^2 for the four source redshift bins. Shear noise σ_γ is set to 0.30 for all four redshift bins.

For the REDMAGIC lens galaxy sample, the number density is not expected to increase significantly for DES-Y5 since the existing data is already volume limited. Therefore, the same redshift distribution as the DES-Y1 data is assumed for DES-Y5. While the redshift distribution will not change, our statistical power will still improve since the survey area will increase. The redshift distributions of the source and lens galaxies are shown in the left panel of Figure 9.2

9.1.2 Forecast: SPT-3G $\kappa_{\rm CMB}$ noise level

Following Section 9.1, the CMB lensing noise is estimated by assuming noise levels of $3.5/\sqrt{2}$ and 3.5 μK-arcmin in temperature and polarization respectively. Here we restrict our analysis to the 150 GHz channel only. The beam width is set to FWHM=1.4′, and we use multipoles up to $\ell_{\rm max}$ = 3000 for temperature (due to foregrounds) and 5000 for polarization. We estimate the noise levels by taking the inverse of the analytical response function[*]:

$$\mathcal{R}_L^\alpha = \frac{1}{2L+1}\sum_{\ell_1\ell_2}\frac{1}{2}W^\alpha_{\ell_1\ell_2 L}W^\alpha_{\ell_1\ell_2 L}F^{(1)}_{\ell_1}F^{(2)}_{\ell_2}, \tag{9.3}$$

where $\alpha = \{\phi(TT), \phi(EE), \phi(TE), \phi(TB), \phi(EB)\}$, $W^\alpha_{\ell_1\ell_2 L}$ is the weight function (Equation 4.14, but generalized to include polarization) and $F^{(1)}_\ell, F^{(2)}_\ell$ are filtering functions (Equation 4.18). We reconstruct the noise levels for each non-zero component pair $\{TT, EE, TE, TB, EB\}$, and combine them by taking:

$$N_L^{MV} = \frac{\sum_\alpha N_L^\alpha \mathcal{R}_L^\alpha}{\sum_\alpha \mathcal{R}_L^\alpha} \tag{9.4}$$

with $N_L^\alpha = 1/\mathcal{R}_L^\alpha$ to form the minimum variance estimate of the CMB convergence noise spectrum. The cross-components between the fields (e.g. $\mathcal{R}_L^{TT}\mathcal{R}_L^{EE}$) are ignored. The amplitude of N_L^{MV} in comparison to the individual noise components are shown in the right panel of Figure 9.2.

9.1.3 Simulations

The input C_L^{ij} are produced using CosmoSIS assuming the central values of DES-Y1-fiducial cosmology listed in Table A.2, and the derived galaxy redshift distribution described in Section 9.1.1. Flask is run in lognormal mode to produce 300 full-sky realizations. The procedures described in Section 6.2 are used to produce realistic CMB maps and galaxy catalogues. We extract four patches from a single realization as shown in Figure 9.3, producing 1200 DES-Y5-like realizations

[*]This is a direct consequence of using the optimal quadratic estimator, as described in Okamoto & Hu 2003

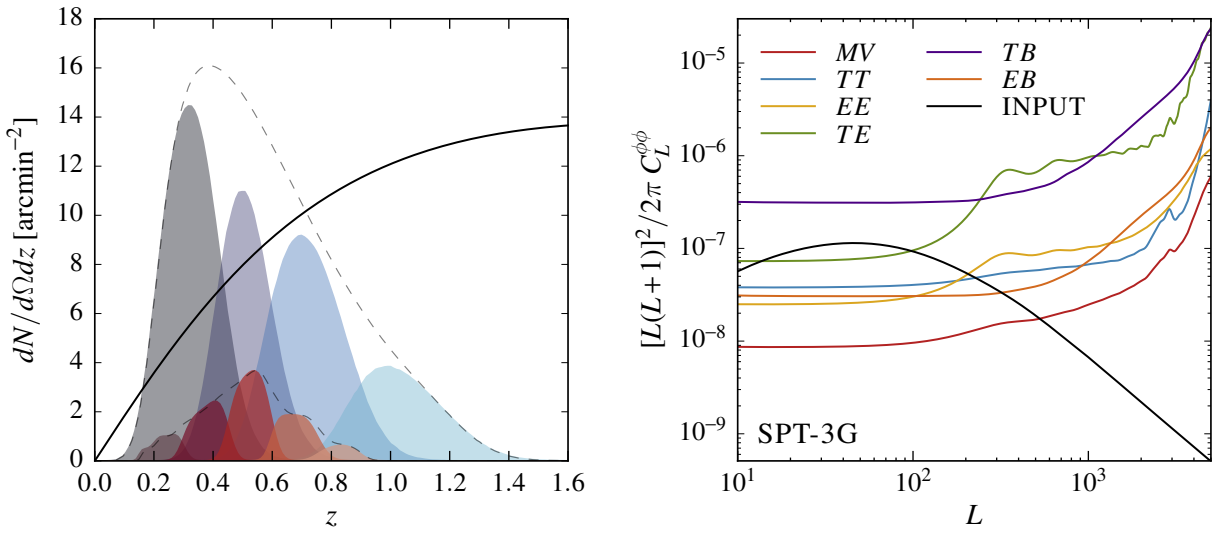

Figure 9.2 **Left:** The predicted redshift distribution of DES-Y5 galaxies. Distributions shaded in blue are the source galaxy samples, and in red are the lens galaxy samples. The dashed lines show the overall distribution. The solid line represents the CMB weak lensing kernel $W^{\kappa_{\rm CMB}}$ which represents the lensing efficiency as a function of redshift. **Right:** forecast of CMB lensing noise levels from different estimators. We utilize the minimum variance noise spectrum (red) for the forecast. The fiducial lensing spectrum is shown as the black solid line.

in total. From these mocks, all the correlation functions between $\delta_{\rm g}, \gamma$ and $\kappa_{\rm CMB}$ are measured in the same way as described in Chapter 7. One important aspect of this forecast is that we presume that polarization maps will be used to reconstruct the lensing map. Since the tSZ effect is

SPT-3G	Resolution	$N_{\rm T}$ [μK-arcmin]	$N_{\rm P}$ [μK-arcmin]	$\ell_{\rm max,T}$	$\ell_{\rm max,P}$	$f_{\rm sky}$
	$1.4'$	$3.5/\sqrt{2}$	3.5	3000	5000	0.06

DES-Y5	$\bar{n}^l$ [10^{-2}arcmin^{-2}]	galaxy bias	$\bar{n}^{\rm s}$ [arcmin^{-2}]	σ_γ	$\ell^\gamma_{\rm max}$	$f_{\rm sky}$
	$[1.3, 3.4, 5.0, 3.0, 0.9]$	$[1.45, 1.55, 1.65, 1.8, 2.0]$	$[3.39, 2.43, 2.79, 1.40]$	0.3	4096	0.12

Table 9.1 Table summarizing the experimental setups used for SPT-3G and DES-Y5. For SPT-3G, only the 150 GHz channel (temperature and polarization) is considered over the 2500 deg^2 footprint. For DES-Y5, we use the same redshift bins as DES-Y1: ($0.15 < z < 0.30$, $0.30 < z < 0.45$, $0.45 < z < 0.60$, $0.60 < z < 0.75$, $0.75 < z < 0.90$) for the lenses, and ($0.20 < z < 0.43$, $0.43 < z < 0.60$, $0.60 < z < 0.90$, $0.90 < z < 1.30$) for the sources.

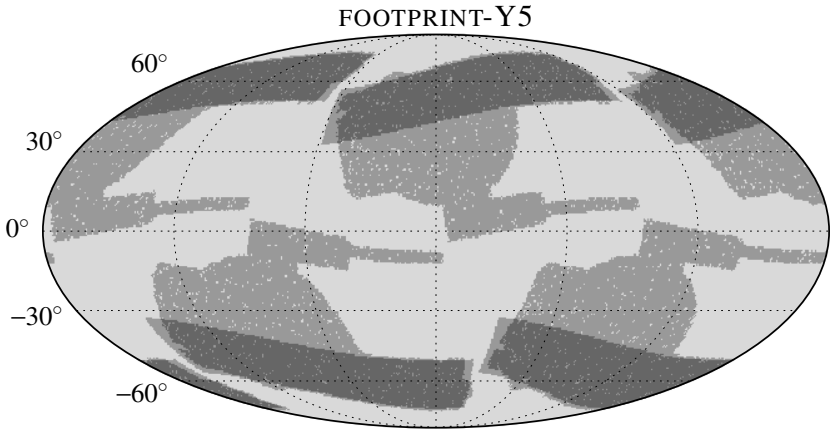

Figure 9.3 Footprints of four SPT and DES cut-outs from one full-sky FLASK realization shown in Mollweide projection. The darker grey regions are equivalent to the SPT 2500 deg^2 patch, and the lighter grey regions corresponds to the DES-Y5 footprint.

expected to be small in polarization, we assume that the lensing map will be free of tSZ bias, and is therefore ignored. This allows us to use a wider angular range without being biased[†].

9.1.4 RESULTS

The correlation function measurements for $\kappa_{\rm CMB} \times \delta_{\rm g}$ and $\kappa_{\rm CMB} \times \gamma_{\rm t}$ using simulated SPT-SZ +*Planck*× DES-Y1 and SPT-3G × DES-Y5 data are shown in Figure 9.4. The size of the uncertainties are reduced by factors of $\sim$ 2 and $\sim$ 5 for $\kappa_{\rm CMB} \times \delta_{\rm g}$ and $\kappa_{\rm CMB} \times \gamma_{\rm t}$ respectively. The smaller improvements in $\kappa_{\rm CMB} \times \delta_{\rm g}$ can be explained by the similarity between the DES-Y5 and DES-Y1 lens samples, and the difference is solely due to the increased survey overlap area and the decrease in the $\kappa_{\rm CMB}$ noise (i.e. the galaxy number density remains the same). For $\kappa_{\rm CMB} \times \gamma_{\rm t}$, we observe a significant improvement since the number density of source galaxies increases, and the noise in shear is reduced (since $\sigma = \sigma_\gamma/\sqrt{N}$), in addition to the reduced $\kappa_{\rm CMB}$ noise and the increased area.

Cosmological parameter constraints are obtained using the theory SPT-3G × DES-Y5 data vector (fiducial correlations computed using the central parameter values), and the covariance ob-

[†]Here we are only considering the tSZ bias, which is the dominant bias. At the level of SPT-3G, other effects may be significant.

tained from the FLASK realizations. We again use COSMOSIS to sample through the parameter space using the same initial values, priors and ranges as described in Chapter 8.

The likelihoods that we obtain are shown in Figures 9.5 and 9.6, and we observe that constraints will be significantly better for DES-Y5. Some of the key improvements are:

- Constraints on cosmological parameters such as S_8 and $\Omega_{\rm m}$ improve from $\Delta S_8 = 0.023$ to 0.009 and $\Delta\Omega_{\rm m} = 0.034$ to 0.017 (such an improvement is due to both the improvement in the CMB lensing data as well as the lower shape noise in DES-Y5)

- Error on galaxy biases are reduced by $\sim 50\%$ (due to improvements in $\delta_{\rm g} \times \delta_{\rm g}$, $\delta_{\rm g} \times \gamma_{\rm t}$ and $\kappa_{\rm CMB} \times \delta_{\rm g}$)

- Uncertainty in the amplitude of intrinsic alignment is reduced to $\Delta A^{\rm IA} = 0.062$ from 0.147 (due to improvements in ξ_+, ξ_-, $\delta_{\rm g} \times \gamma_{\rm t}$ and $\kappa_{\rm CMB} \times \gamma_{\rm t}$ correlations)

The forecasts presented here are conservative since we have only considered the SPT 150 GHz frequency channel and we could expect further improvements when temperature and polarization data from the 95 and 220 GHz channels are added.

9.1.5 FUTURE WORK

Using the existing pipeline of two-point correlation measurements and likelihood calculations, the simulated data vectors will be replaced with the SPT-SZ +*Planck* CMB lensing map and galaxies/galaxy weak lensing data from DES-Y1. Such a measurement is expected to give the most stringent cosmological constraint from large-scale structure to date, and the results are expected to be released by the end of 2017.

In the next decade, galaxy surveys such as LSST (LSST Science Collaboration et al., 2009), *WFIRST* (Spergel et al., 2013) and *Euclid* (Laureijs et al., 2011) are planned to cover $\sim 18000, \sim 2200, \sim 15000$ deg^2 respectively, of the sky at an unprecedented depth, looking at larger cosmological volumes. These surveys will probe more distant galaxies, which is advantageous for cross-correlation with CMB lensing, since the galaxy and galaxy lensing kernels will have more

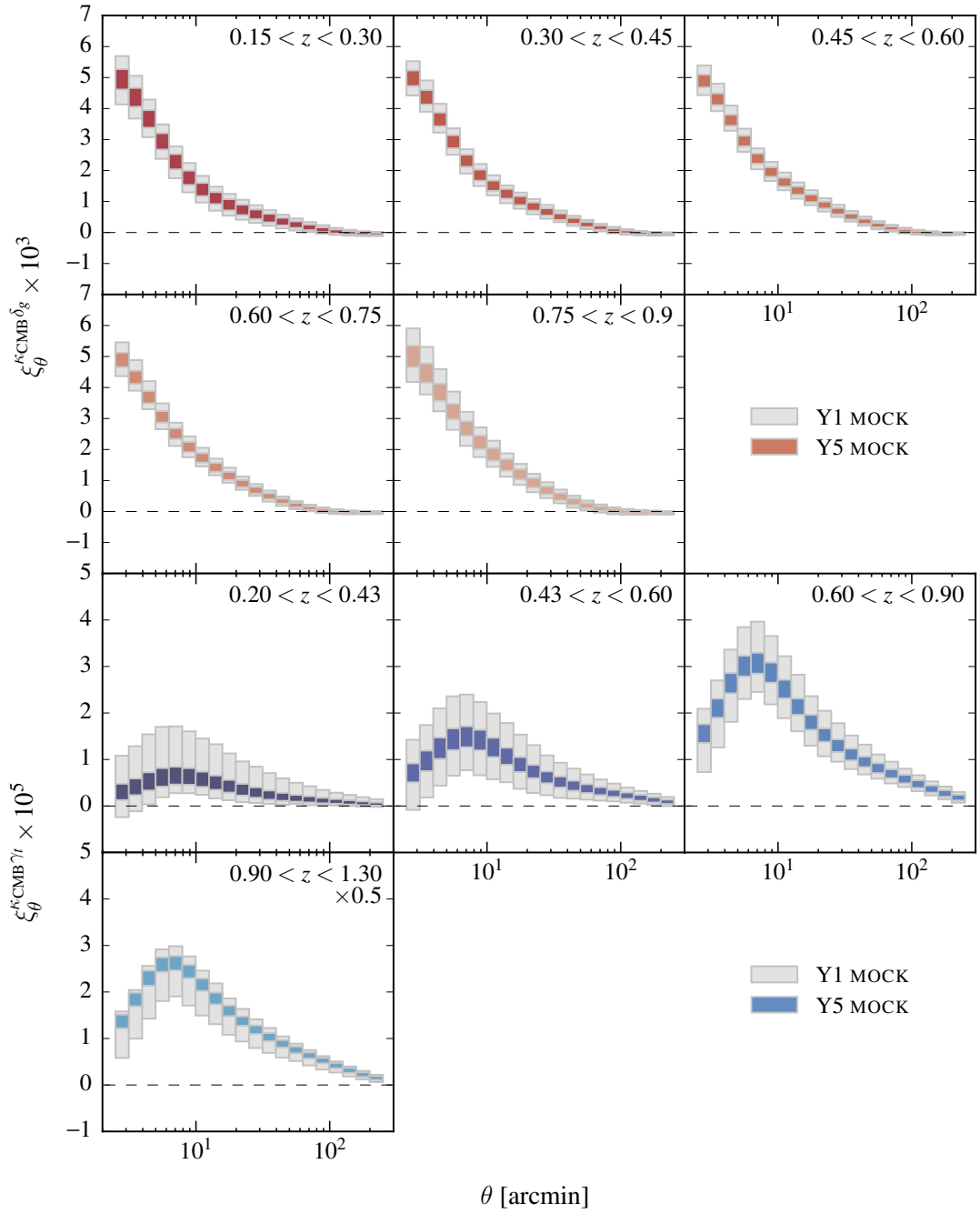

Figure 9.4 The estimated errors calculated using 1200 FLASK lognormal realizations for $\kappa_{\rm CMB} \times \delta_{\rm g}$ (upper five panels) and $\kappa_{\rm CMB} \times \gamma_{\rm t}$ (lower four panels). Results for SPT-SZ +*Planck* × DES-Y1 simulated data are shown in grey and in colour for SPT-3G × DES-Y5 simulated data.

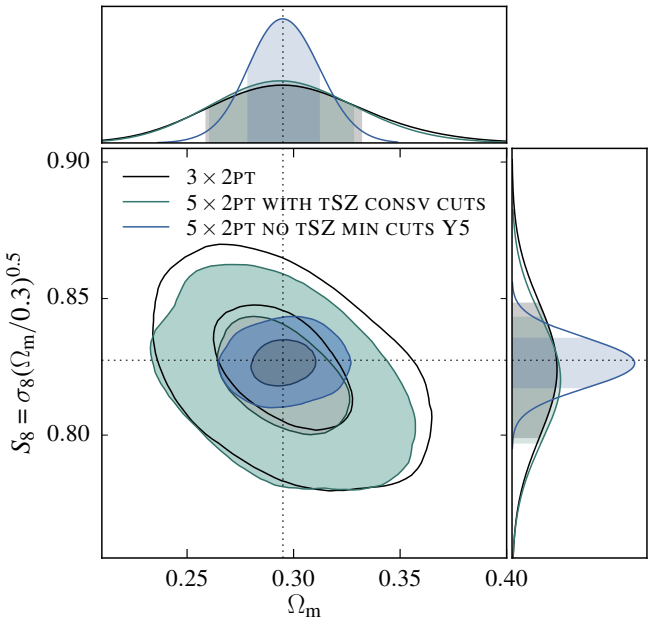

Figure 9.5 Constraints on Ω_m and S_8 for DES-Y1 3×2pt (black), SPT-SZ +*Planck* × DES-Y1 5×2pt with tSZ bias and conservative scale cuts (teal) and SPT-3G × DES-Y5 5×2pt without tSZ bias and with minimal scale cuts (blue).

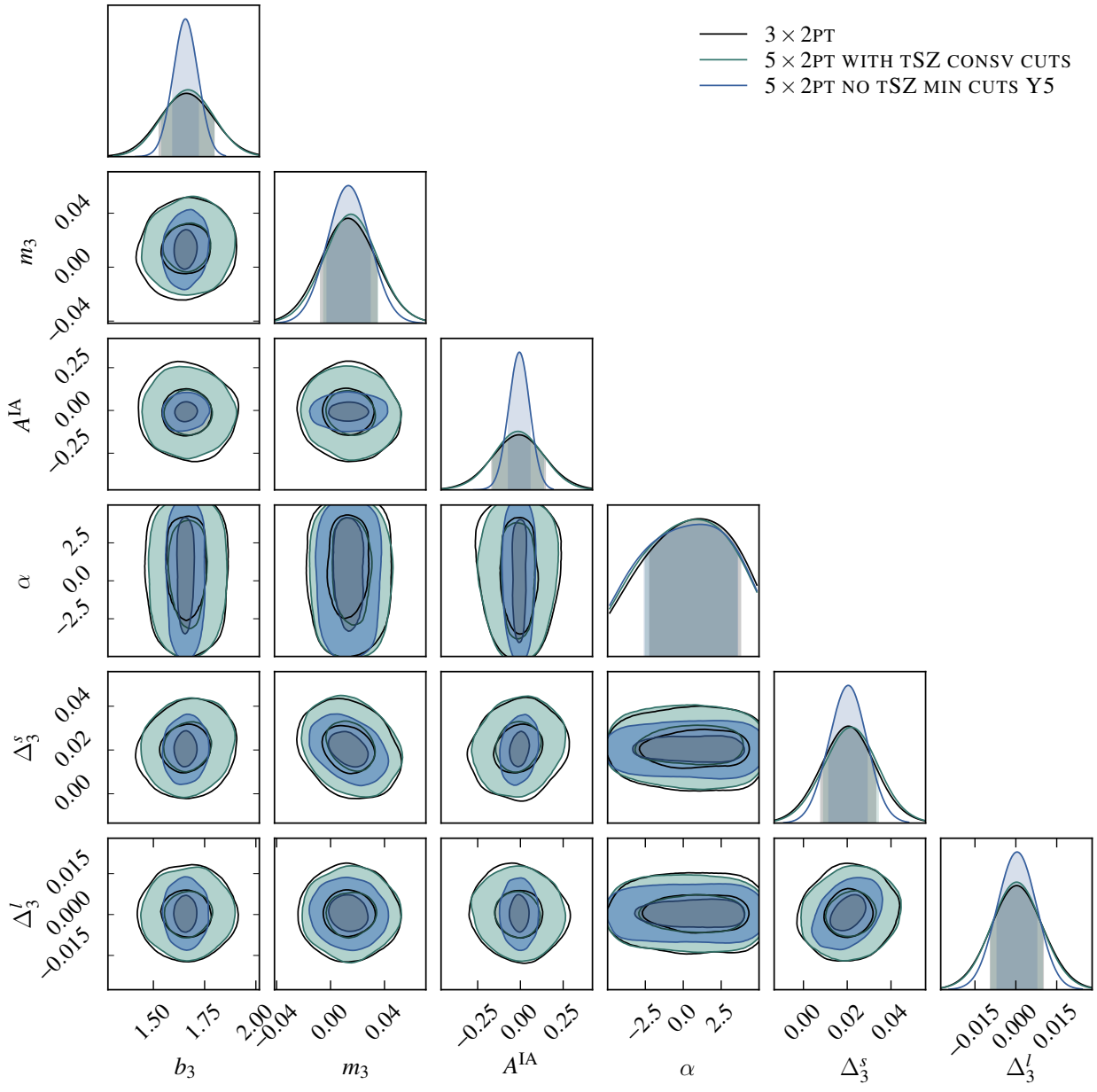

Figure 9.6 Constraints on b_3, m_3, $A^{\rm IA}$, α, Δ_3^s, Δ_3^l for DES-Y1 3×2pt (black), SPT-SZ +*Planck* × DES-Y1 5×2pt with tSZ bias and conservative scale cuts (teal) and SPT-3G × DES-Y5 5×2pt without tSZ bias and with minimal scale cuts (blue). We see that the constraints improve for all the parameters except for α. All the other parameters are shown in Figure A.3.

overlap with the CMB lensing kernel. *WFIRST* and *Euclid* will be conducting observations in space allowing for excellent shape measurements without contamination from atmospheric fluctuations. While LSST will not have this advantage, it is planned to cover a larger area to fainter magnitudes. Most importantly, these surveys are planned to operate in synergy, where *Euclid* and *WFIRST* will be used to calibrate systematic errors in LSST shape measurements as well as identifying blended galaxy images (Jain et al., 2015).

The next generation proposed ground based stage-4 CMB experiment (CMB-S4), is a collaboration of many CMB groups using multiple telescopes at various locations such as the South Pole and Atacama desert. While the specifications of the instruments are currently under discussion, forecasts are being carried out to explore the optimal designs to ensure maximum scientific gain. One important scientific aspect is the synergy of CMB-S4 and optical surveys, and therefore the footprint is likely to overlap with the aforementioned future-generation galaxy surveys (Abazajian et al., 2016).

The analysis presented in this thesis could be directly applied to future data sets. With the precision that is expected, characterization of systematic errors and biases to high precision will be crucial. Cross-correlation measurements are expected to become increasingly useful since they are less sensitive to systematic biases, and therefore can be used as a valuable cross-check.

10

Summary and Conclusion

10.1 Summary

This thesis begins by describing the background and history of observational cosmology, and in particular, the historical developments of CMB and galaxy surveys as well as the scientific milestones reached in our current data rich era. While the individual results are not described in depth, it is important to realize that our current understanding of the universe is an accumulation of successive knowledge acquired through past experiments.

Chapter 2 is dedicated to the theoretical framework of weak gravitational lensing. The equations derived in the chapter are used to quantify our measurements and to map theoretical models to observables.

In producing a map of the gravitational potential, we make use of CMB temperature data from the South Pole Telescope (which has the best signal-to-noise ratio per mode over the SPT 2500 deg^2 patch) and *Planck* (which covers a large fraction of the sky, with high signal-to-noise

ratio for the large angular modes), both of which are described in Chapter 3. We optimally combine temperature maps from the two experiments to produce a map that is valid across a wider range of angular scales than the individual maps alone. The combined temperature map has many useful applications (including the measurement of the CMB power spectrum and the making of component separated maps), but is particularly suited for CMB lensing reconstruction since mode pairs with large L separations in harmonic-space can be used.

In Chapter 4 we use the quadratic estimator technique presented in Hu 2000 and Okamoto & Hu 2003 to reconstruct a map of the gravitational potential, which is a widely used method, since it is easily applicable to data. The resulting map from this procedure is presented in Figure 4.2. This is the largest lensing map produced using a high-resolution ground-based experiment, and has the highest signal-to-noise ratio over the SPT 2500 deg^2 patch. In the near future, we will have a lensing map from SPTpol, reconstructed from polarization maps in addition to the temperature map (Mocanu et al. 2017, in preparation). However, this map will only cover 500 deg^2, and therefore, the lensing map presented in this thesis will remain valuable until the next generation 2500 deg^2 lensing map is produced (upon completion of the SPT-3G survey).

Chapter 5 is dedicated to the various validation tests carried out on the CMB weak lensing map obtained in the previous chapter. We first demonstrate that the mean lensing power spectrum calculated from simulated lensing maps matches with the input spectrum to high accuracy (see Figure 5.1). We measure the power spectrum of the data map and obtain $\eta^{\phi\phi} = \hat{C}_L^{\phi\phi}/\hat{C}_{L,\mathrm{fid}}^{\phi\phi} = 0.95^{+0.06}_{-0.06}(\mathrm{Stat.})^{+0.02}_{-0.02}(\mathrm{Sys.})$ after removing foregrounds biases, which is consistent with the theoretical prediction of $\eta^{\phi\phi} = 1$.

We perform null tests by calculating the auto/cross-spectra of the curl mode, unlensed and the L-R (equivalent to noise) maps. We find that all these results are consistent with a lensing amplitude of zero. We additionally vary the temperature multipole range used for the lensing reconstruction, mode masking on a (ℓ, m) grid, masking radii, cluster masking level, response function smoothing length, SPT-SZ beam and SPT-SZ calibration to probe whether the auto and cross-spectra (with *WISE*) are sensitive to these systematics. We conclude that these variations

only lead to a small difference in the resulting spectra relative to our statistical uncertainties and that our map making pipeline is robust to systematic errors.

One of the primary uses of the SPT-SZ + *Planck* lensing map is for cross-correlations with external tracers such as galaxies from DES. In particular, the DES-Y5 is planned to almost completely cover the SPT nominal footprint, and is therefore ideal for cross-correlation analyses, which is the main focus of Chapter 7. While cross-correlations have been measured using other CMB lensing maps and galaxies catalogues, SPT×DES cross-correlations are unique in that they are cross-correlations between high S/N CMB lensing maps (relative to *Planck*) and deep galaxy data over a large sky area. In the chapter, the galaxy lensing - CMB weak lensing cross-spectrum is presented. More specifically, the cross-correlation between the DES-SV NGMIX shear catalogue and the SPT-SZ weak lensing map is calculated, and the correlation amplitude relative to the fiducial mode was found to be $A = 0.88 \pm 0.30$ giving us a $\sim 3\sigma$ measurement. We show that this measurement is robust against systematics by calculating the cross-spectrum using a different pipeline such as the Kaiser-Squires reconstruction for which we obtain consistent results. Systematics errors such as photometric redshift bias are also tested for, and the effects are found to be smaller than our statistical uncertainties. A simple test of varying the tSZ mask is also conducted to test the contamination in the CMB weak lensing map, and this effect is shown to have negligible impact on the resulting spectrum. Although the results are not ground breaking, it is nonetheless important that such a correlation can be measured at all. We will soon have higher signal-to-noise ratio measurements using future data sets with more sky coverage, higher galaxy number density and improved shape measurements.

DES-Y1 data are currently blinded for the cross-correlation analyses, and we are unable to present the scientific results we have obtained so far. Therefore, instead, we produced realistic simulations of galaxy density $\delta_{\rm g}$, galaxy weak lensing γ and CMB weak lensing $\kappa_{\rm CMB}$ to forecast the signal-to-noise ratio that we will obtain for SPT-SZ + *Planck* × DES-Y1 cross-correlations. Correlated maps (five lens, four source bins and one CMB lensing bin) were generated using FLASK, and galaxy catalogues were extracted by sampling the maps. The simulations were tai-

lored to match the Y1 data as closely as possible by using the same galaxy redshift distributions, number densities and shear noise. Realistic CMB weak lensing maps were obtained by computing the shear field at the redshift of last scattering surface, and adding a noise realization.

The two-point correlation functions between $\kappa_{\rm CMB} \times \delta_{\rm g}$ and $\kappa_{\rm CMB} \times \gamma_{\rm t}$ using the FLASK simulations were calculated, and the results are summarized in Tables 7.1 and 7.2. We find that the signal-to-noise ratios for $\kappa_{\rm CMB} \times \delta_{\rm g}$ range between 15 and 28, while for $\kappa_{\rm CMB} \times \gamma_{\rm t}$ the ratios range between 3 and 8. For both of these probes, the correlation with the convergence map produced from a simulated tSZ map (using DES REDMAPPER galaxies with $\lambda > 20$) and *Planck* GNILC 545 GHz CIB map were calculated to quantify the $\kappa_{\rm tSZ/CIB} \times \delta_{\rm g}$ and $\kappa_{\rm tSZ/CIB} \times \kappa_{\rm E}$ bispectra, which are biases of concern in cross-correlations with CMB weak lensing. While we find that the bias due to CIB is small, bias due to tSZ can not be neglected. In this thesis, we simply exclude the angular scales that are affected by this bias from the analysis. Characterization of these bispectra have never been attempted before in the literature, but is essential for any future cross-correlation analyses that involve CMB lensing maps derived from temperature data.

In Chapter 8, we add the two cross-correlations that involve CMB weak lensing to the galaxy/galaxy weak lensing measurement-only framework (3×2pt), and investigate the improvements that we gain in constraining cosmological parameters. We additionally test whether the $\kappa_{\rm tSZ}$ bias impacts the constraints by comparing the likelihood obtained from data vectors with and without the tSZ bias and scale cuts. We compare the constraints obtained from five setups:

- 3×2pt,
- 5×2pt with tSZ bias with minimal scale cuts,
- 5×2pt with tSZ bias with conservative scale cuts,
- 5×2pt without tSZ bias with minimal scale cuts, and
- 5×2pt without tSZ bias with conservative scale cuts.

The results are shown in Figures 8.3 and 8.4. We find improvements in constraining $\Omega_{\rm m}$, S_8 and linear galaxy bias b when adding the cross-correlation probes. However, we also find that the tSZ bias does shift the constraints, but the effect could be mitigated by applying conservative scales cuts.

Finally in Chapter 9, we model the anticipated noise levels of SPT-3G and DES-Y5 to forecast the constraining power that these data sets will provide. This is accomplished by producing 1200 SPT-3G-like CMB lensing maps and DES-Y5-like galaxy catalogues using FLASK and calculating all the two-point correlation functions which is then used to calculate the covariance matrix. Results (Figure 9.4) show that we could expect significant improvements if SPT-3G $\times$ DES-Y5 data are used in comparison to SPT-SZ $+$*Planck* $\times$ DES-Y1 data. In particular, the uncertainties on $\kappa_{\rm CMB} \times \gamma_{\rm t}$ correlations are expected to reduce to $\sim$ 35% of the SPT-SZ $+$*Planck* $\times$ DES-Y1 values. This leads to significant improvements in the cosmological parameter constraints as well as constraints on systematics as shown in Figure 9.6).

10.2 Conclusion

With the vast amount of CMB and galaxy data available today, we are currently in a golden age of observational cosmology, on the verge of making various ground breaking discoveries pertaining to the origin and growth of the universe. However, the universe does not reveal its nature on its own; raw data must be cleaned and processed in order to extract accurate and precise cosmological information. The development of robust and reliable analysis tools is therefore critical in moving towards a better understanding of the universe.

Data analysis techniques are continuously evolving according to the resources available. One of the factors that is driving this is the growth of high-performance computing facilities. With more computing power, higher-order calculations that were intractable previously become feasible. For example, while we have shown that our quadratic estimator technique is sufficient given our current noise levels, Carron & Lewis 2017 recently developed a maximum-likelihood lensing reconstruction method which is able to extract more signal, in exchange for computational expense. Such advancements are imperative for future CMB lensing analyses, which will require unprecedented precision.

A major aspect that is missing from this thesis is the prospect of using the SPT-SZ $+$*Planck* lensing map for *delensing*; an increasingly important technique to reverse the gravitational lens-

ing effect to recover the undistorted view of the CMB. Such an effort is essential in searching for signatures of primordial gravitational waves imprinted on the CMB, which will give us new insights into the very early universe. While delensing can be done using existing data, it is anticipated that we will only be able to do so partially, given our noisy estimate of the lensing potential. Future CMB experiments with much lower noise such as SPT-3G and CMB-S4 will provide better results.

The 5×2pt analysis between SPT-SZ +*Planck* and DES-Y1 data will be the first analysis to combine 3×2pt from a single galaxy survey and CMB lensing data generated from a high-resolution ground-based experiment. While the combination of these two data sets will already provide competitive results, improvements will be made rapidly; DES-Y3 data are presently available, DES-Y4 data are being processed and DES-Y5/SPT-3G observations are currently being conducted. Therefore, our understanding of the universe will progressively improve over the next few years.

On a longer timescale, the next generation CMB experiments as well as new galaxy surveys such as LSST, *Euclid* and *WFIRST* will be launched. These experiments will work in synergy, complementing each other by reducing systematic errors by serving as cross-checks. The various probes will slice through the cosmological parameter space differently, and are expected to yield some of the tightest constraints on cosmological parameters yet obtained.

A

Appendix A

A.1 Block Jackknife Method

The most common approach in estimating uncertainties for a cosmological measurement is by using simulations. However, we frequently encounter situations where simulations that match the data do not exist. In such cases, we resort to resampling error estimation techniques, which use the data themselves.

One popular resampling technique is the jackknife method developed by Quenouille 1949, and in particular, the "delete one jackknife" method detailed in Shao 1986. In this method, the data is first divided into N sub-samples, and the measurement is made by removing one of the sub-samples. The same measurement is repeated N times removing a different sub-sample each time, and the scatter in the N measurements are used to estimate the covariance. Mathematically, this

is calculating:

$$\mathcal{C}_{ij}^{\rm jackknife} = \frac{N-1}{N}\sum_{k=1}^{N}(x_i^k - \langle x_i\rangle)(x_j^k - \langle x_j,\rangle) \tag{A.1}$$

where N is the number of sub-samples, x^k is the measurement made by removing the k-th sub-sample, i, j are bin indices, and

$$\langle x_i\rangle = \sum_{k=1}^{N} x_i^k/N. \tag{A.2}$$

In the context of large-scale structure analyses, the data map is divided into sub-regions and each jackknife sample is computed by calculating the correlation function with one sub-region (or block) removed (hence the name "block jackknife"). A comprehensive analysis comparing the jackknife method with other resampling techniques and errors estimated through simulations can be found in Norberg et al. 2009; Friedrich et al. 2016 and references therein.

A.2 Wigner-3j Properties

The integral of three spherical harmonics can be written in terms of Wigner-3j symbols. For regular spin-0 spherical harmonics this is:

$$\begin{aligned}&\int d\hat{\boldsymbol{n}}\; Y_{\ell_1 m_1}(\hat{\boldsymbol{n}})Y_{\ell_2 m_2}(\hat{\boldsymbol{n}})Y_{\ell_3 m_3}(\hat{\boldsymbol{n}})\\ &=\sqrt{\frac{(2\ell_1+1)(2\ell_2+1)(2\ell_3+1)}{4\pi}}\begin{pmatrix}\ell_1 & \ell_2 & \ell_3\\ 0 & 0 & 0\end{pmatrix}\begin{pmatrix}\ell_1 & \ell_2 & \ell_3\\ m_1 & m_2 & m_3\end{pmatrix},\end{aligned} \tag{A.3}$$

and for spin-weighted spherical harmonics (if $s_1 + s_2 + s_3 = 0$):

$$\begin{aligned}&\int d\hat{\boldsymbol{n}}\; {}_{s_1}Y_{\ell_1 m_1}(\hat{\boldsymbol{n}})_{s_2}Y_{\ell_2 m_2}(\hat{\boldsymbol{n}})_{s_3}Y_{\ell_3 m_3}(\hat{\boldsymbol{n}})\\ &=\sqrt{\frac{(2\ell_1+1)(2\ell_2+1)(2\ell_3+1)}{4\pi}}\begin{pmatrix}\ell_1 & \ell_2 & \ell_3\\ -s_1 & -s_2 & -s_3\end{pmatrix}\begin{pmatrix}\ell_1 & \ell_2 & \ell_3\\ m_1 & m_2 & m_3\end{pmatrix}\end{aligned} \tag{A.4}$$

The $3j$ symbol is invariant under an even permutation of its columns:

$$\begin{pmatrix} \ell_1 & \ell_2 & \ell_3 \\ m_1 & m_2 & m_3 \end{pmatrix} = \begin{pmatrix} \ell_2 & \ell_3 & \ell_1 \\ m_2 & m_3 & m_1 \end{pmatrix} = \begin{pmatrix} \ell_3 & \ell_1 & \ell_2 \\ m_3 & m_1 & m_2 \end{pmatrix}, \tag{A.5}$$

and gains a phase factor under an odd permutation:

$$\begin{pmatrix} \ell_1 & \ell_2 & \ell_3 \\ m_1 & m_2 & m_3 \end{pmatrix} = (-1)^{\ell_1+\ell_2+\ell_3} \begin{pmatrix} \ell_2 & \ell_1 & \ell_3 \\ m_2 & m_1 & m_3 \end{pmatrix} = (-1)^{\ell_1+\ell_2+\ell_3} \begin{pmatrix} \ell_1 & \ell_3 & \ell_2 \\ m_1 & m_3 & m_2 \end{pmatrix}, \tag{A.6}$$

and also when the sign of m are flipped:

$$\begin{pmatrix} \ell_1 & \ell_2 & \ell_3 \\ -m_1 & -m_2 & -m_3 \end{pmatrix} = (-1)^{\ell_1+\ell_2+\ell_3} \begin{pmatrix} \ell_1 & \ell_2 & \ell_3 \\ m_1 & m_2 & m_3 \end{pmatrix}. \tag{A.7}$$

The Wigner-$3j$ symbol also obeys the orthogonality relation:

$$\sum_{m_1 m_2} \begin{pmatrix} \ell_1 & \ell_2 & \ell_3 \\ m_1 & m_2 & m_3 \end{pmatrix} \begin{pmatrix} \ell_1 & \ell_2 & \ell_4 \\ m_1 & m_2 & m_4 \end{pmatrix} = \delta_{\ell_3 \ell_4} \delta_{m_3 m_4} \frac{\delta(\ell_1, \ell_2, \ell_3)}{2\ell_3 + 1} \tag{A.8}$$

where $\delta(\ell_1, \ell_2, \ell_3) = 1$ when the triangular relation $|\ell_1 - \ell_2| \leq \ell_3 \leq \ell_1 + \ell_2$ is satisfied, and equals 0 otherwise. These properties are used in Sections A.3 and A.4.

A.3 Separability of the Building Blocks

A brief description of QUICKLENS is given in Section 4.1. Here, we give a more thorough derivation of the calculation that is being carried out internally. We begin by rewriting Equations 4.12

as

$$
\begin{aligned}
{}_0F_{\ell_1 L \ell_2} &= \sqrt{\frac{(2\ell_1+1)(2\ell_2+1)(2L+1)}{16\pi}}[L(L+1)+\ell_2(\ell_2+1)-\ell_1(\ell_1+1)]\begin{pmatrix}\ell_1 & L & \ell_2\\ 0 & 0 & 0\end{pmatrix} \\
&= -\sqrt{\frac{(2\ell_1+1)(2\ell_2+1)(2L+1)}{4\pi}}\sqrt{L(L+1)\ell_2(\ell_2+1)}\begin{pmatrix}\ell_1 & \ell_2 & L\\ 0 & -1 & 1\end{pmatrix}\left(\frac{1+(-1)^{\ell_1+\ell_2+L}}{2}\right)
\end{aligned}
\tag{A.9}
$$

(and similarly for Equation 4.11). Equation 4.14 can then be written as:

$$
\begin{aligned}
W^{TT}_{\ell_1\ell_2 L} = &-\sqrt{\frac{(2\ell_1+1)(2\ell_2+1)(2L+1)}{4\pi}}\left(\frac{1+(-1)^{\ell_1+\ell_2+L}}{2}\right) \\
&\times\left[C^{TT,\mathrm{unl}}_{\ell_1}\sqrt{L(L+1)\ell_1(\ell_1+1)}\begin{pmatrix}\ell_1 & \ell_2 & L\\ -1 & 0 & 1\end{pmatrix}\right. \\
&\left.+\,C^{TT,\mathrm{unl}}_{\ell_2}\sqrt{L(L+1)\ell_2(\ell_2+1)}\begin{pmatrix}\ell_1 & \ell_2 & L\\ 0 & -1 & 1\end{pmatrix}\right]
\end{aligned}
\tag{A.10}
$$

(any permutation in the ordering of the Wigner-3j does not affect the sign since $\ell_1+\ell_2+L$ is always even, which is ensured by the last term of the first line). This can be further broken up

into:

$$
\begin{aligned}
W^{TT}_{\ell_1\ell_2 L} = &- \sqrt{\frac{(2\ell_1+1)(2\ell_2+1)(2L+1)}{4\pi}} \left(\frac{1+(-1)^{\ell_1+\ell_2+L}}{2}\right) \\
&\times \left[\frac{1}{2} C^{TT,\mathrm{unl}}_{\ell_1} \sqrt{L(L+1)\ell_1(\ell_1+1)} \begin{pmatrix} \ell_1 & \ell_2 & L \\ -1 & 0 & 1 \end{pmatrix}\right. \\
&+ \frac{1}{2} C^{TT,\mathrm{unl}}_{\ell_1} \sqrt{L(L+1)\ell_1(\ell_1+1)} \begin{pmatrix} \ell_1 & \ell_2 & L \\ 1 & 0 & -1 \end{pmatrix} (-1)^{(\ell_1+\ell_2+L)} \\
&+ \frac{1}{2} C^{TT,\mathrm{unl}}_{\ell_2} \sqrt{L(L+1)\ell_2(\ell_2+1)} \begin{pmatrix} \ell_1 & \ell_2 & L \\ 0 & -1 & 1 \end{pmatrix} \\
&\left.+ \frac{1}{2} C^{TT,\mathrm{unl}}_{\ell_2} \sqrt{L(L+1)\ell_2(\ell_2+1)} \begin{pmatrix} \ell_1 & \ell_2 & L \\ 0 & 1 & -1 \end{pmatrix} (-1)^{(\ell_1+\ell_2+L)}\right],
\end{aligned} \tag{A.11}
$$

and we can set $(-1)^{\ell_1+\ell_2+L} = 1$ since it is always even. This can be rewritten as:

$$
W^{TT}_{\ell_1\ell_2 L} = (-1)^{S^{\phi,j}_L} \sum_j^4 \sqrt{\frac{(2\ell_1+1)(2\ell_2+1)(2L+1)}{4\pi}} \begin{pmatrix} \ell_1 & \ell_2 & L \\ -s^{TT,j}_{\ell_1} & -s^{TT,j}_{\ell_2} & S^{TT,j}_L \end{pmatrix} w^{TT,j}_{\ell_1} w^{TT,j}_{\ell_2} w^{TT,j}_L, \tag{A.12}
$$

with

$$(j=1):$$
$$s_{\ell_1}^{TT,j}=1, s_{\ell_2}^{TT,j}=0, S_L^{TT,j}=1, w_{\ell_1}^{TT,j}=\sqrt{\ell_1(\ell_1+1)}C_{\ell_1}^{TT,\mathrm{unl}}, w_{\ell_2}^{TT,j}=\frac{1}{2}, w_L^{TT,j}=\sqrt{L(L+1)}$$

$$(j=2):$$
$$s_{\ell_1}^{TT,j}=-1, s_{\ell_2}^{TT,j}=0, S_L^{TT,j}=-1, w_{\ell_1}^{TT,j}=\sqrt{\ell_1(\ell_1+1)}C_{\ell_1}^{TT,\mathrm{unl}}, w_{\ell_2}^{TT,j}=\frac{1}{2}, w_L^{TT,j}=\sqrt{L(L+1)}$$

$$(j=3):$$
$$s_{\ell_1}^{TT,j}=0, s_{\ell_2}^{TT,j}=1, S_L^{TT,j}=1, w_{\ell_1}^{TT,j}=\sqrt{\ell_2(\ell_2+1)}C_{\ell_2}^{TT,\mathrm{unl}}, w_{\ell_2}^{TT,j}=\frac{1}{2}, w_L^{TT,j}=\sqrt{L(L+1)}$$

$$(j=4):$$
$$s_{\ell_1}^{TT,j}=0, s_{\ell_2}^{TT,j}=-1, S_L^{TT,j}=-1, w_{\ell_1}^{TT,j}=\sqrt{\ell_2(\ell_2+1)}C_{\ell_2}^{TT,\mathrm{unl}}, w_{\ell_2}^{TT,j}=\frac{1}{2}, w_L^{TT,j}=\sqrt{L(L+1)}.$$

The net weight function is now written as the product of three different weight functions $w_{\ell_1}^{TT,j}, w_{\ell_2}^{TT,j}, w_L^{TT,j}$. This separability allows us to write Equation 4.17 as:

$$\bar{\phi}=\sum_{\ell_1 m_1 \ell_2 m_2}\sum_{j}^{4}\frac{(-1)^M}{2}\sqrt{\frac{(2\ell_1+1)(2\ell_2+1)(2L+1)}{4\pi}}\begin{pmatrix}\ell_1 & \ell_2 & L\\ m_1 & m_2 & -M\end{pmatrix}\begin{pmatrix}\ell_1 & \ell_2 & L\\ -s_{\ell_1}^{TT,j} & -s_{\ell_2}^{TT,j} & S_L^{TT,j}\end{pmatrix}$$
$$\times(-1)^{S_L^{TT,j}}w_{\ell_1}^{TT,j}w_{\ell_2}^{TT,j}w_L^{TT,j}\bar{T}_{\ell_1 m_1}\bar{T}_{\ell_2 m_2}, \tag{A.13}$$

and therefore, using the relationship between Wigner-3j symbols and spin-weighted spherical harmonics (Equation A.4):

$$\bar{\phi}_{LM}=\frac{1}{2}\int d\hat{\boldsymbol{n}}\sum_j {}_{s_L^{TT,j}}Y_{LM}^*(\hat{\boldsymbol{n}})w_L^{TT,j}\left[\sum_{\ell_1 m_1}{}_{s_1^{TT,j}}Y_{\ell_1 m_1}(\hat{\boldsymbol{n}})w_{\ell_1}^{TT,j}T_{\ell_1 m_1}\right]\left[\sum_{\ell_2 m_2}{}_{s_2^{TT,j}}Y_{\ell_2 m_2}(\hat{\boldsymbol{n}})w_{\ell_2}^{TT,j}T_{\ell_2 m_2}\right] \tag{A.14}$$

which is a calculation of $\mathcal{O}(j_{\max}\ell_{\max}^2 L_{\max})$ instead of $\mathcal{O}(\ell_{\max}^4 L_{\max}^2)$, leading to a considerable speed-up in computations (Planck Collaboration XV., 2015).

A.4 Mode-Coupling due to the Mask

This section follows the derivation presented in (Hivon et al., 2002). The spherical harmonic transform is an idealization in the case of a full-sphere. In most real applications, the full sphere is not available, either due to the survey area or masking of foregrounds (most commonly the Galactic plane). Therefore, in practice, the spherical harmonic expansion we take is:

$$\begin{aligned}\tilde{a}_{\ell_2 m_2} &= \int d\hat{\boldsymbol{n}} a(\hat{\boldsymbol{n}}) W(\hat{\boldsymbol{n}}) Y^*_{\ell 2 m_2}(\hat{\boldsymbol{n}}) \\ &= \sum_{\ell_1, m_1} a_{\ell_1 m_1} \int d\hat{\boldsymbol{n}} Y_{\ell_1, m_1}(\hat{\boldsymbol{n}}) W(\hat{\boldsymbol{n}}) Y^*_{\ell_2, m_2}(\hat{\boldsymbol{n}}) \\ &= \sum_{\ell_1 m_1} a_{\ell_1 m_1} K_{\ell_1 m_1 \ell_2 m_2}, \end{aligned} \tag{A.15}$$

where tilde is used to denote the biased $a_{\ell m}$, $W(\hat{\boldsymbol{n}})$ is the weight map, and K is the mode coupling kernel:

$$\begin{aligned} K_{\ell_1 m_1 \ell_2 m_2} &\equiv \int d\hat{\boldsymbol{n}} Y_{\ell_1 m_1}(\hat{\boldsymbol{n}}) W(\hat{\boldsymbol{n}}) Y^*_{\ell 2 m_2}(\hat{\boldsymbol{n}}) \\ &= \sum_{\ell_3 m_3} w_{\ell_3 m_3} \int d\hat{\boldsymbol{n}} Y_{\ell_1 m_1}(\hat{\boldsymbol{n}}) Y_{\ell_3 m_3}(\hat{\boldsymbol{n}}) Y^*_{\ell 2 m_2}(\hat{\boldsymbol{n}}) \\ &= \sum_{\ell_3 m_3} w_{\ell_3 m_3} (-1)^{m_2} \left[\frac{(2\ell_1+1)(2\ell_2+1)(2\ell_3+1)}{4\pi} \right]^{1/2} \begin{pmatrix} \ell_1 & \ell_2 & \ell_2 \\ 0 & 0 & 0 \end{pmatrix} \begin{pmatrix} \ell_1 & \ell_2 & \ell_2 \\ m_1 & -m_2 & m_3 \end{pmatrix} \end{aligned} \tag{A.16}$$

where we have used $Y^*_{\ell_2 m_2} = (-1)^{m_2} Y_{\ell_2 - m_2}$ and the property of the Wigner-3j symbol. Therefore, when computing the spectrum:

$$\begin{aligned}
\langle \tilde{C}_{\ell_1} \rangle &= \frac{1}{2\ell_1 + 1} \sum_{m_1=-\ell_1}^{\ell_1} \langle \tilde{a}_{\ell_1 m_1} \tilde{a}^*_{\ell_1 m_1} \rangle \\
&= \frac{1}{2\ell_1 + 1} \sum_{m_1=-\ell_1}^{\ell_1} \sum_{\ell_2 m_2} \sum_{\ell_3 m_3} \langle a_{\ell_2 m_2} a^*_{\ell_3 m_3} \rangle K_{\ell_1 m_1 \ell_2 m_2} K^*_{\ell_1 m_1 \ell_3 m_3} \\
&= \frac{1}{2\ell_1 + 1} \sum_{m_1=-\ell_1}^{\ell_1} \sum_{\ell_2} \langle C_{\ell_2} \rangle \sum_{m_2=-\ell_2}^{\ell_2} |K_{\ell_1 m_1 \ell_2 m_2}|^2,
\end{aligned} \tag{A.17}$$

where $\langle a_{\ell_2 m_2} a^*_{\ell_3 m_3} \rangle = \langle C_{\ell_2} \rangle \delta_{\ell_2 \ell_3} \delta_{m_2 m_3}$ was used. We can substitute Equation A.16 here and obtain:

$$\begin{aligned}
\langle \tilde{C}_{\ell_1} \rangle = &\frac{1}{2\ell_1 + 1} \sum_{\ell_2} \langle C_{\ell_2} \rangle \sum_{\ell_3 m_3} \sum_{\ell_4 m_4} w_{\ell_3 m_3} w_{\ell_4 m_4} \\
&\times \left[\frac{(2\ell_1 + 1)(2\ell_2 + 1)(2\ell_3 + 1)}{4\pi} \right]^{1/2} \left[\frac{(2\ell_1 + 1)(2\ell_2 + 1)(2\ell_4 + 1)}{4\pi} \right]^{1/2} \\
&\times \begin{pmatrix} \ell_1 & \ell_2 & \ell_3 \\ 0 & 0 & 0 \end{pmatrix} \begin{pmatrix} \ell_1 & \ell_2 & \ell_4 \\ 0 & 0 & 0 \end{pmatrix} \sum_{m_1 m_2} \begin{pmatrix} \ell_1 & \ell_2 & \ell_3 \\ m_1 & -m_2 & m_3 \end{pmatrix} \begin{pmatrix} \ell_1 & \ell_2 & \ell_4 \\ m_1 & -m_2 & m_4 \end{pmatrix},
\end{aligned} \tag{A.18}$$

and use the orthogonality relations of the Wigner-3j symbols (A.8) and simplify the equation to:

$$\langle \tilde{C}_{\ell_1} \rangle = \sum_{\ell_2} M_{\ell_1 \ell_2} \langle C_{\ell_2} \rangle \tag{A.19}$$

where

$$M_{\ell_1 m_1 \ell_2 m_2} = \frac{2\ell_2 + 1}{2\pi} \sum_{\ell_3} (2\ell_3 + 1) \mathcal{W}_{\ell_3} \begin{pmatrix} \ell_1 & \ell_2 & \ell_3 \\ 0 & 0 & 0 \end{pmatrix}^2 \tag{A.20}$$

and $\mathcal{W}_{\ell_3} = \frac{1}{(2\ell_3+1)} \sum_{m_3} |w_{\ell_3 m_3}|^2$ is the angular power spectrum of the weight function. This calculation is used in the Section 7.2, when calculating the $\kappa_{\rm CMB} \times \kappa_{\rm E}$ cross-spectra in flat-sky.

A.5 Derivation of Kaiser-Squires Reconstruction

The shear components and the convergence can be written as the partial derivatives of the gravitational potential:

$$\gamma_1 = \frac{1}{2}\left(\frac{\partial^2\phi(\theta_1,\theta_2)}{\partial\theta_1^2} - \frac{\partial^2\phi(\theta_1,\theta_2)}{\partial\theta_2^2}\right) \tag{A.21}$$

$$\gamma_2 = \frac{\partial^2\phi(\theta_1,\theta_2)}{\partial\theta_1\partial\theta_2} \tag{A.22}$$

$$\kappa = \frac{1}{2}\left(\frac{\partial^2\phi(\theta_1,\theta_2)}{\partial\theta_1^2} + \frac{\partial^2\phi(\theta_1,\theta_2)}{\partial\theta_2^2}\right) \tag{A.23}$$

Taking the definition of Fourier transforms:

$$f(\theta_1,\theta_2) = \int_{-\infty}^{+\infty} F(k_1,k_2)\exp^{ik_1\theta_1+ik_2\theta_2}\,dk_1dk_2 \tag{A.24}$$

$$\frac{\partial}{\partial\theta_1}f(\theta_1,\theta_2) = \int_{-\infty}^{+\infty} F(k_1,k_2)ik_1\exp^{ik_1\theta_1+ik_2\theta_2}\,dk_1dk_2 \tag{A.25}$$

$$\frac{\partial^2}{\partial\theta_1^2}f(\theta_1,\theta_2) = \int_{-\infty}^{+\infty} F(k_1,k_2)(-k_1^2)\exp^{ik_1\theta_1+ik_2\theta_2}\,dk_1dk_2 \tag{A.26}$$

Therefore Equations A.21, A.22, A.23 can be written as (in Fourier space):

$$\tilde{\gamma}_1 = -\frac{1}{2}(k_1^2 - k_2^2)\tilde{\phi}(\theta_1,\theta_2) \tag{A.27}$$

$$\tilde{\gamma}_2 = -k_1k_2\tilde{\phi}(\theta_1,\theta_2) \tag{A.28}$$

$$\tilde{\kappa} = -\frac{1}{2}(k_1^2 + k_2^2)\tilde{\phi}(\theta_1,\theta_2) \tag{A.29}$$

A.27 and A.28 can be written in terms of $\bar{\kappa}$:

$$\tilde{\kappa} = \frac{k_1^2+k_2^2}{k_1^2-k_2^2}\tilde{\gamma}_1 \rightarrow \tilde{\gamma}_1 = \frac{k_1^2-k_2^2}{k_1^2+k_2^2}\tilde{\kappa} \tag{A.30}$$

$$\tilde{\kappa} = \frac{k_1^2+k_2^2}{2k_1^2k_2^2}\tilde{\gamma}_2 \rightarrow \tilde{\gamma}_2 = \frac{2k_1k_2}{k_1^2+k_2^2}\tilde{\kappa} \tag{A.31}$$

This is in essence a linear equation of the form:

$$\begin{bmatrix} \tilde{\gamma}_1 \\ \tilde{\gamma}_2 \end{bmatrix} = \frac{1}{k_1^2 + k_2^2} \begin{bmatrix} k_1^2 - k_2^2 \\ 2k_1 k_2 \end{bmatrix} \tilde{\kappa} \tag{A.32}$$

$$\begin{aligned} [k_1^2 - k_2^2, 2k_1 k_2] \begin{bmatrix} \tilde{\gamma}_1 \\ \tilde{\gamma}_2 \end{bmatrix} &= \frac{1}{k_1^2 + k_2^2} [k_1^2 - k_2^2, 2k_1 k_2] \begin{bmatrix} k_1^2 - k_2^2 \\ 2k_1^2 k_2^2 \end{bmatrix} \tilde{\kappa} \\ &= \frac{1}{k_1^2 + k_2^2} (k_1^4 + k_2^4 - 2k_1^2 k_2^2 + 4k_1^2 k_2^2) \tilde{\kappa} \\ &= \frac{(k_1^2 + k_2^2)^2}{k_1^2 + k_2^2} \tilde{\kappa} \\ &= (k_1^2 + k_2^2) \tilde{\kappa} \end{aligned} \tag{A.33}$$

Dividing both sides with $(k_1^2 + k_2^2)$ gives:

$$\tilde{\kappa} = \frac{k_1^2 - k_2^2}{k_1^2 + k_2^2} \tilde{\gamma}_1 + \frac{2k_1^2 k_2^2}{k_1^2 + k_2^2} \tilde{\gamma}_2 \tag{A.34}$$

$\kappa_{\rm CMB}\delta_{\rm g}$	
1-1	$[5.0/10.4, 250.0]$
1-2	$[5.0/17.7, 250.0]$
1-3	$[5.0/17.7, 250.0]$
1-4	$[5.0/16.9, 250.0]$
1-3	$[5.0/14.3, 250.0]$

$\kappa_{\rm CMB}\gamma_{\rm t}$	
1-1	$[20.0/20.0, 250.0]$
1-2	$[20.0/20.0, 250.0]$
1-3	$[20.0/54.0, 250.0]$
1-4	$[20.0/42.0, 250.0]$

$\delta_{\rm g}\delta_{\rm g}$	
1-1	$[43.0, 250.0]$
2-2	$[27.0, 250.0]$
3-3	$[20.0, 250.0]$
4-4	$[16.0, 250.0]$
5-5	$[14.0, 250.0]$

$\gamma_{\rm t}$	
1-1	$[64.0, 250.0]$
1-2	$[64.0, 250.0]$
1-3	$[64.0, 250.0]$
1-4	$[64.0, 250.0]$
2-1	$[40.0, 250.0]$
2-2	$[40.0, 250.0]$
2-3	$[40.0, 250.0]$
2-4	$[40.0, 250.0]$
3-1	$[30.0, 250.0]$
3-2	$[30.0, 250.0]$
3-3	$[30.0, 250.0]$
3-4	$[30.0, 250.0]$
4-1	$[24.0, 250.0]$
4-2	$[24.0, 250.0]$
4-3	$[24.0, 250.0]$
4-4	$[24.0, 250.0]$
5-1	$[21.0, 250.0]$
5-2	$[21.0, 250.0]$
5-3	$[21.0, 250.0]$
5-4	$[21.0, 250.0]$

ξ_+	
1-1	$[7.195005, 250.0]$
1-2	$[7.195005, 250.0]$
1-3	$[5.715196, 250.0]$
1-4	$[5.715196, 250.0]$
2-2	$[4.539741, 250.0]$
2-3	$[4.539741, 250.0]$
2-4	$[4.539741, 250.0]$
3-3	$[3.606045, 250.0]$
3-4	$[3.606045, 250.0]$
4-4	$[3.606045, 250.0]$

ξ_-	
1-1	$[90.579750, 250.0]$
1-2	$[71.950053, 250.0]$
1-3	$[71.950053, 250.0]$
1-4	$[71.950053, 250.0]$
2-2	$[57.151958, 250.0]$
2-3	$[57.151958, 250.0]$
2-4	$[45.397414, 250.0]$
3-3	$[45.397414, 250.0]$
3-4	$[45.397414, 250.0]$
4-4	$[36.060448, 250.0]$

Table A.1 Scale cuts applied to measurements in the likelihood calculations in Chapters 8 and 9. The first column for each section corresponds to the z-bin pairs and the second column corresponds to the angular ranges in arcminutes.

Parameter	value	prior
cosmological Parameters		
$\Omega_{\rm m}$	0.295	$[0.10, 0.90]$
h_0	0.688	$[0.55, 0.90]$
$\Omega_{\rm b}$	0.047	$[0.01, 0.07]$
$n_{\rm s}$	0.968	$[0.8, 1.3]$
$A_{\rm s}$	2.26×10^{-9}	$[0.5, 5.0] \times 10^{-9}$
τ	0.08	fixed
Ω_K	0	fixed
$\Omega_\nu h^2$	0.0006155	fixed
w	-1.0	fixed
$Y_{\rm He}$	0.245341	fixed
Nuisance Parameters		
linear galaxy bias		
b_1, b_2, b_3, b_4, b_5	$1.45, 1.55, 1.65, 1.8, 2.0$	$[0.8, 2.5]$
shear calibration bias		
m_1, m_2, m_3, m_4	$0.013, 0.013, 0.013, 0.013$	$(0.021, 0.021, 0.021, 0.021)$
Intrinsic alignment parameters		
$A^{\rm IA}$	0	$[-5, 5]$
$\alpha^{\rm IA}$	0	$[-5, 5]$
z_0	0.62	fixed
lens photoz error		
$\Delta^l_1, \Delta^l_2, \Delta^l_3, \Delta^l_4, \Delta^l_5$	$0, 0, 0, 0, 0$	$(0.01, 0.01, 0.01, 0.01, 0.01)$
source photoz error		
$\Delta^{\rm s}_1, \Delta^{\rm s}_2, \Delta^{\rm s}_3, \Delta^{\rm s}_4$	$-0.0037, -0.0171, 0.0200, 0.0224$	$(0.017, 0.015, 0.0138, 0.0215)$
tSZ amplitude		
$A_{\rm tSZ}$	0 (1 for tSZ biased data vector)	fixed

Table A.2 Table summarizing the central values and priors used in the analysis. Square brackets denote a flat prior in the range given, while regular brackets denote a Gaussian prior with μ and σ listed in the "value" and "prior" columns respectively.

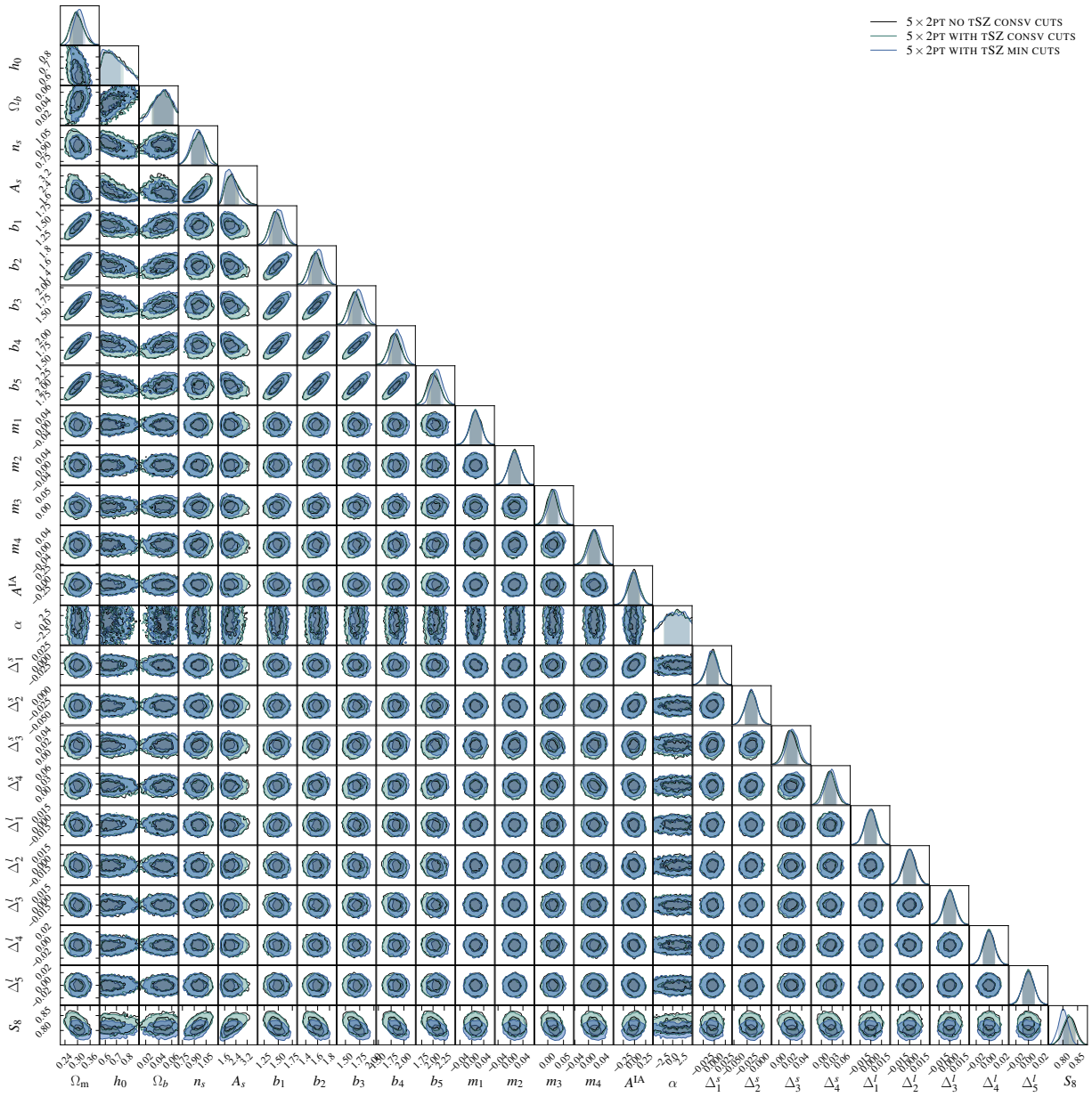

Figure A.1 Constraints on all the parameters for 5×2pt without tSZ bias and with conservative scale cuts (black), 5×2pt with tSZ bias and conservative scale cuts (teal), and 5×2pt with tSZ bias and minimal scale cuts (blue). Same as Figure 8.3, but for all 26 parameters (and less smoothing applied).

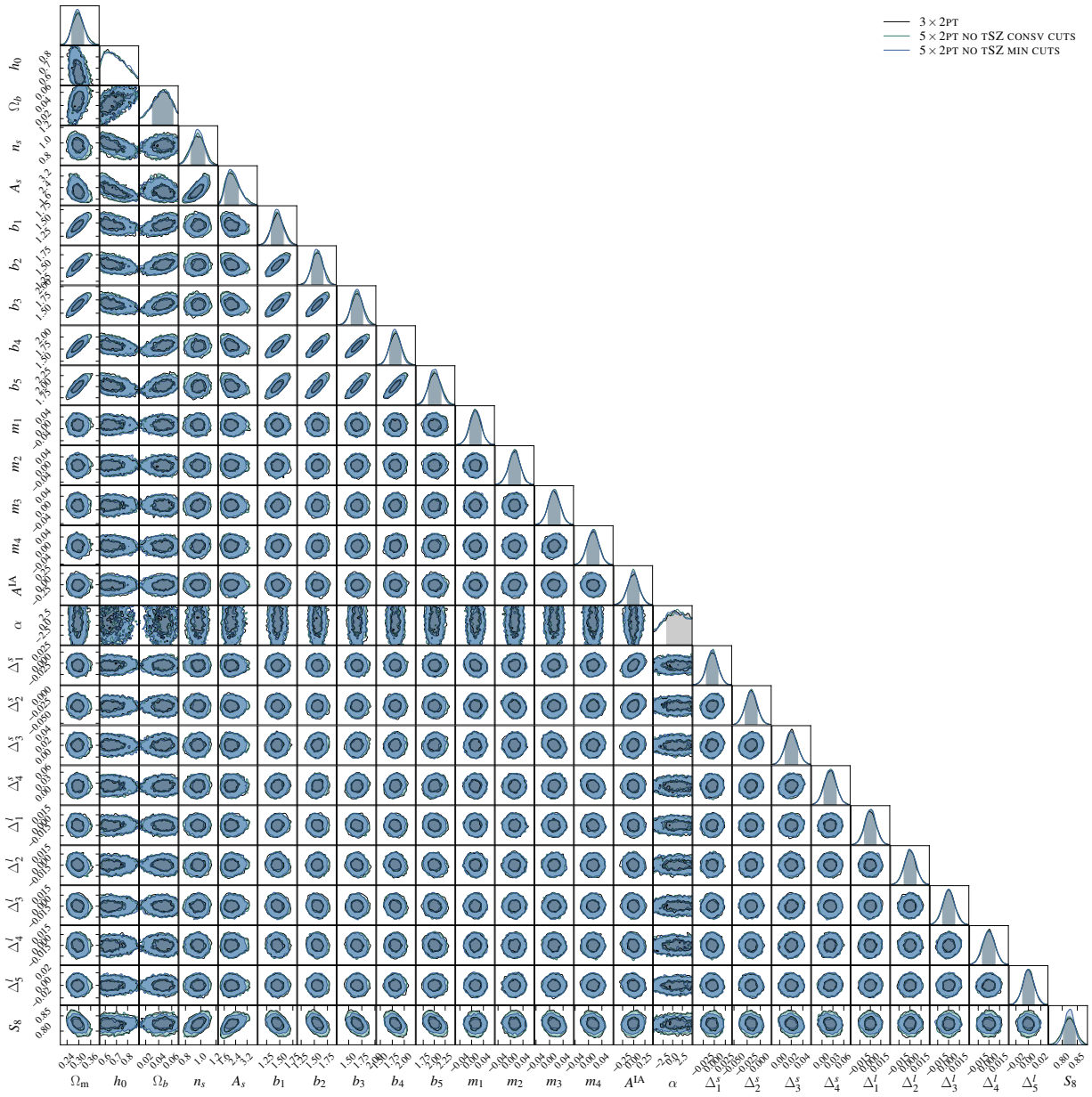

Figure A.2 Constraints on all the parameters for 3×2pt (black), 5×2pt without tSZ bias and with conservative scales cuts (teal), and 5×2pt without tSZ bias and with minimal scales cuts (blue). Same as Figure 8.4, but for all 26 parameters (and less smoothing applied).

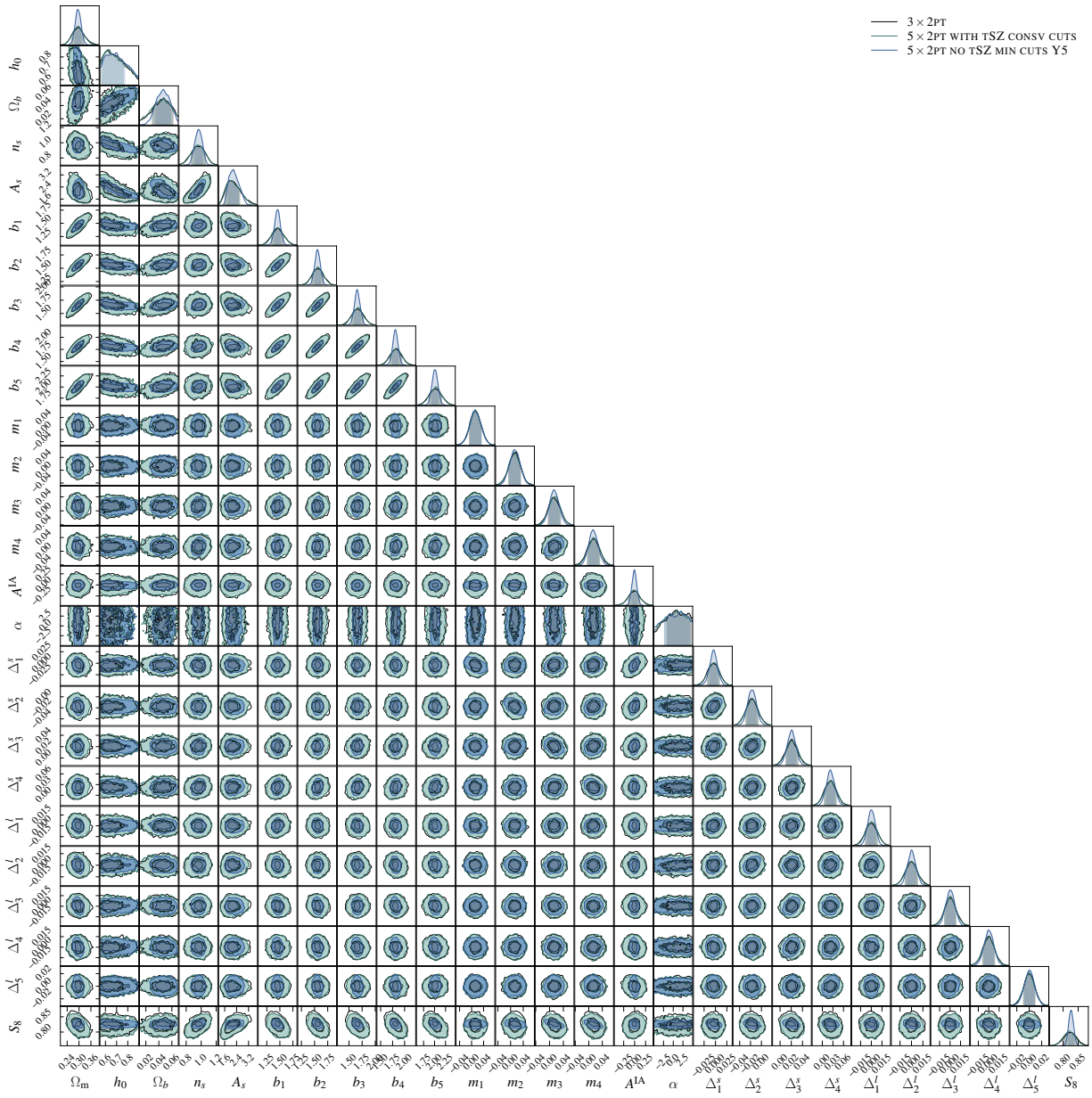

Figure A.3 Constraints on all the parameters for DES-Y1 3×2pt (black), SPT-SZ +*Planck* × DES-Y1 5×2pt with tSZ bias and conservative scale cuts (teal), and SPT-3G × DES-Y5 5×2pt without tSZ bias and with minimal scale cuts (blue). Same as figure 9.6, but for all 26 parameters (and less smoothing applied).

References

Abazajian, K. N., Adshead, P., Ahmed, Z., et al., CMB-S4 Science Book, First Edition. 2016, ArXiv e-prints, arXiv:1610.02743

Albrecht, A., & Steinhardt, P. J., Cosmology for grand unified theories with radiatively induced symmetry breaking. 1982, Physical Review Letters, 48, 1220

Allison, R., Lindsay, S. N., Sherwin, B. D., et al., The Atacama Cosmology Telescope: measuring radio galaxy bias through cross-correlation with lensing. 2015, MNRAS, 451, 849

Ansari, R., & Magneville, C., Partial CMB maps: bias removal and optimal binning of the angular power spectrum. 2010, MNRAS, 405, 1421

Arnold, K., Ade, P. A. R., Anthony, A. E., et al. 2010, in Society of Photo-Optical Instrumentation Engineers (SPIE) Conference Series, Vol. 7741, Society of Photo-Optical Instrumentation Engineers (SPIE) Conference Series

Astropy Collaboration, Robitaille, T. P., Tollerud, E. J., et al., Astropy: A community Python package for astronomy. 2013, A&A, 558, A33

Bartelmann, M., TOPICAL REVIEW Gravitational lensing. 2010, Classical and Quantum Gravity, 27, 233001

Battaglia, N., Bond, J. R., Pfrommer, C., & Sievers, J. L., On the Cluster Physics of Sunyaev-Zel'dovich and X-Ray Surveys. I. The Influence of Feedback, Non-thermal Pressure, and Cluster Shapes on Y-M Scaling Relations. 2012, ApJ, 758, 74

Becker, M. R., Troxel, M. A., MacCrann, N., et al., Cosmic shear measurements with Dark Energy Survey Science Verification data. 2016, Phys. Rev. D, 94, 022002

Benítez, N., Bayesian Photometric Redshift Estimation. 2000, ApJ, 536, 571

Bennett, C. L., Halpern, M., Hinshaw, G., et al., First-Year Wilkinson Microwave Anisotropy Probe (WMAP) Observations: Preliminary Maps and Basic Results. 2003a, ApJS, 148, 1

Bennett, C. L., Halpern, M., Hinshaw, G., et al., —. 2003b, ApJS, 148, 1

Bennett, C. L., Bay, M., Halpern, M., et al., The Microwave Anisotropy Probe Mission. 2003c, ApJ, 583, 1

Benoit-Lévy, A., Déchelette, T., Benabed, K., et al., Full-sky CMB lensing reconstruction in presence of sky-cuts. 2013, A&A, 555, A37

Benson, B. A., Ade, P. A. R., Ahmed, Z., et al. 2014, in Society of Photo-Optical Instrumentation Engineers (SPIE) Conference Series, Vol. 9153, Society of Photo-Optical Instrumentation Engineers (SPIE) Conference Series

Bertschinger, E., Cosmological dynamics. 1995, NASA STI/Recon Technical Report N, 96, astro-ph/9503125

Bleem, L. E., van Engelen, A., Holder, G. P., et al., A Measurement of the Correlation of Galaxy Surveys with CMB Lensing Convergence Maps from the South Pole Telescope. 2012, ApJ, 753, L9

Bleem, L. E., Stalder, B., de Haan, T., et al., Galaxy Clusters Discovered via the Sunyaev-Zel'dvich Effect in the 2500 Square Degree SPT-SZ Surveyo. 2015, ApJS, 216, 27

Bonnett, C., Troxel, M. A., Hartley, W., et al., Redshift distributions of galaxies in the Dark Energy Survey Science Verification shear catalogue and implications for weak lensing. 2016, Phys. Rev. D, 94, 042005

Bridle, S., & King, L., Dark energy constraints from cosmic shear power spectra: impact of intrinsic alignments on photometric redshift requirements. 2007, New Journal of Physics, 9, 444

Brown, M. L., Taylor, A. N., Hambly, N. C., & Dye, S., Measurement of intrinsic alignments in galaxy ellipticities. 2002, MNRAS, 333, 501

Bucher, M. 2016, in International Journal of Modern Physics Conference Series, Vol. 43, International Journal of Modern Physics Conference Series, 1660188

Cardoso, J.-F., Le Jeune, M., Delabrouille, J., Betoule, M., & Patanchon, G., Component Separation With Flexible Models Application to Multichannel Astrophysical Observations. 2008, IEEE Journal of Selected Topics in Signal Processing, 2, 735

Carlstrom, J. E., Holder, G. P., & Reese, E. D., Cosmology with the Sunyaev-Zel'dovich Effect. 2002, ARA&A, 40, 643

Carlstrom, J. E., Ade, P. A. R., Aird, K. A., et al., The 10 Meter South Pole Telescope. 2011, PASP, 123, 568

Carrasco Kind, M., & Brunner, R. J., TPZ: photometric redshift PDFs and ancillary information by using prediction trees and random forests. 2013, MNRAS, 432, 1483

Carron, J., & Lewis, A., Maximum a posteriori CMB lensing reconstruction. 2017, Phys. Rev. D, 96, 063510

Cavaliere, A., & Fusco-Femiano, R., X-rays from Hot Plasma in Clusters of Galaxies. 1976, A&A, 49, 137

Chon, G., Challinor, A., Prunet, S., Hivon, E., & Szapudi, I., Fast estimation of polarization power spectra using correlation functions. 2004, MNRAS, 350, 914

Clampitt, J., Sánchez, C., Kwan, J., et al., Galaxy-galaxy lensing in the Dark Energy Survey Science Verification data. 2017, MNRAS, 465, 4204

Clerkin, L., Kirk, D., Manera, M., et al., Testing the lognormality of the galaxy and weak lensing convergence distributions from Dark Energy Survey maps. 2017, MNRAS, 466, 1444

Coil, A. L. 2013, The Large-Scale Structure of the Universe, ed. T. D. Oswalt & W. C. Keel, 387

Coles, P., & Jones, B., A lognormal model for the cosmological mass distribution. 1991, MNRAS, 248, 1

Colless, M., Dalton, G., Maddox, S., et al., The 2dF Galaxy Redshift Survey: spectra and redshifts. 2001, MNRAS, 328, 1039

Condon, J. J., Cotton, W. D., Greisen, E. W., et al., The NRAO VLA Sky Survey. 1998, AJ, 115, 1693

Cooray, A., Kamionkowski, M., & Caldwell, R. R., Cosmic shear of the microwave background: The curl diagnostic. 2005, Phys. Rev. D, 71, 123527

Cooray, A., Li, C., & Melchiorri, A., Trispectrum of 21-cm background anisotropies as a probe of primordial non-Gaussianity. 2008, Phys. Rev. D, 77, 103506

Crawford, T. M., Chown, R., Holder, G. P., et al., Maps of the Magellanic Clouds from Combined South Pole Telescope and PLANCK Data. 2016, ApJS, 227, 23

Crocce, M., Carretero, J., Bauer, A. H., et al., Galaxy clustering, photometric redshifts and diagnosis of systematics in the DES Science Verification data. 2016, MNRAS, 455, 4301

Dark Energy Survey Collaboration, Abbott, T., Abdalla, F. B., et al., The Dark Energy Survey: more than dark energy - an overview. 2016, MNRAS, 460, 1270

Das, S., Errard, J., & Spergel, D., Can CMB Lensing Help Cosmic Shear Surveys? 2013, ArXiv e-prints, arXiv:1311.2338 [astro-ph.CO]

Das, S., Marriage, T. A., Ade, P. A. R., et al., The Atacama Cosmology Telescope: A Measurement of the Cosmic Microwave Background Power Spectrum at 148 and 218 GHz from the 2008 Southern Survey. 2011, ApJ, 729, 62

de Haan, T., Benson, B. A., Bleem, L. E., et al., Cosmological Constraints from Galaxy Clusters in the 2500 Square-degree SPT-SZ Survey. 2016, ApJ, 832, 95

de Jong, J. T. A., Verdoes Kleijn, G. A., Kuijken, K. H., & Valentijn, E. A., The Kilo-Degree Survey. 2013, Experimental Astronomy, 35, 25

De Zotti, G., Ricci, R., Mesa, D., et al., Predictions for high-frequency radio surveys of extragalactic sources. 2005, A&A, 431, 893

DES Collaboration, Abbott, T. M. C., Abdalla, F. B., et al., Dark Energy Survey Year 1 Results: Cosmological Constraints from Galaxy Clustering and Weak Lensing. 2017, ArXiv e-prints, arXiv:1708.01530

Dodelson, S. 2003, Modern cosmology

—. 2017, Gravitational Lensing

Doux, C., Penna-Lima, M., Vitenti, S. D. P., et al., Cosmological constraints from a joint analysis of cosmic microwave background and large-scale structure. 2017, ArXiv e-prints, arXiv:1706.04583

Durrer, R., The cosmic microwave background: the history of its experimental investigation and its significance for cosmology. 2015, Classical and Quantum Gravity, 32, 124007

Durrer, R., Novosyadlyj, B., & Apunevych, S., Acoustic Peaks and Dips in the Cosmic Microwave Background Power Spectrum: Observational Data and Cosmological Constraints. 2003, ApJ, 583, 33

Eisenstein, D. J., Weinberg, D. H., Agol, E., et al., SDSS-III: Massive Spectroscopic Surveys of the Distant Universe, the Milky Way, and Extra-Solar Planetary Systems. 2011, AJ, 142, 72

Elvin-Poole, J., Crocce, M., Ross, A. J., et al., Dark Energy Survey Year 1 Results: Galaxy clustering for combined probes. 2017, ArXiv e-prints, arXiv:1708.01536

Fixsen, D. J., Kogut, A., Levin, S., et al., ARCADE 2 Measurement of the Extra-Galactic Sky Temperature at 3-90 GHz. 2009, submitted to ApJ, arXiv:0901.0555

Flaugher, B., Diehl, H. T., Honscheid, K., et al., The Dark Energy Camera. 2015, AJ, 150, 150

Foreman, S., Becker, M. R., & Wechsler, R. H., Cosmic shear as a probe of galaxy formation physics. 2016, MNRAS, 463, 3326

Fowler, J. W., Acquaviva, V., Ade, P. A. R., et al., The Atacama Cosmology Telescope: A Measurement of the 600 < ell < 8000 Cosmic Microwave Background Power Spectrum at 148 GHz. 2010, ApJ, 722, 1148

Friedrich, O., Seitz, S., Eifler, T. F., & Gruen, D., Performance of internal covariance estimators for cosmic shear correlation functions. 2016, MNRAS, 456, 2662

Gamow, G., The Evolution of the Universe. 1948, Nature, 162, 680

George, E. M., Reichardt, C. L., Aird, K. A., et al., A Measurement of Secondary Cosmic Microwave Background Anisotropies from the 2500-Square-degree SPT-SZ Survey. 2015, ApJ, 799, 177

Giannantonio, T., Fosalba, P., Cawthon, R., et al., CMB lensing tomography with the DES Science Verification galaxies. 2016, MNRAS, 456, 3213

Górski, K. M., Hivon, E., Banday, A. J., et al., HEALPix: A Framework for High-Resolution Discretization and Fast Analysis of Data Distributed on the Sphere. 2005, ApJ, 622, 759

Graff, P., Feroz, F., Hobson, M. P., & Lasenby, A., SKYNET: an efficient and robust neural network training tool for machine learning in astronomy. 2014, MNRAS, 441, 1741

Guth, A. H., Inflationary universe: A possible solution to the horizon and flatness problems. 1981, Phys. Rev. D, 23, 347

Hall, N. R., Knox, L., Reichardt, C. L., et al., Angular Power Spectra of the Millimeter Wavelength Background Light from Dusty Star-forming Galaxies with the South Pole Telescope. 2010, ApJ, 718, 632

Hanany, S., Ade, P., Balbi, A., et al., MAXIMA-1: A Measurement of the Cosmic Microwave Background Anisotropy on Angular Scales of 10'-5°. 2000, ApJ, 545, L5

Hand, N., Leauthaud, A., Das, S., et al., First measurement of the cross-correlation of CMB lensing and galaxy lensing. 2015, Phys. Rev. D, 91, 062001

Hanson, D., Challinor, A., Efstathiou, G., & Bielewicz, P., CMB temperature lensing power reconstruction. 2011, Phys. Rev. D, 83, 043005

Hanson, D., Challinor, A., & Lewis, A., Weak lensing of the CMB. 2010, General Relativity and Gravitation, 42, 2197

Harnois-Déraps, J., Tröster, T., Hojjati, A., et al., CFHTLenS and RCSLenS cross-correlation with Planck lensing detected in fourier and configuration space. 2016, MNRAS, 460, 434

Harnois-Déraps, J., Tröster, T., Chisari, N. E., et al., KiDS-450: Tomographic Cross-Correlation of Galaxy Shear with {\it Planck} Lensing. 2017, ArXiv e-prints, arXiv:1703.03383

Hasselfield, M., Hilton, M., Marriage, T. A., et al., The Atacama Cosmology Telescope: Sunyaev-Zel'dovich selected galaxy clusters at 148 GHz from three seasons of data. 2013, J. Cosmology Astropart. Phys., 7, 8

Heymans, C., Van Waerbeke, L., Bacon, D., et al., The Shear Testing Programme - I. Weak lensing analysis of simulated ground-based observations. 2006, MNRAS, 368, 1323

Heymans, C., Van Waerbeke, L., Miller, L., et al., CFHTLenS: the Canada-France-Hawaii Telescope Lensing Survey. 2012, MNRAS, 427, 146

Hildebrandt, H., Viola, M., Heymans, C., et al., KiDS-450: cosmological parameter constraints from tomographic weak gravitational lensing. 2017, MNRAS, 465, 1454

Hill, J. C., & Pajer, E., Cosmology from the thermal Sunyaev-Zel'dovich power spectrum: Primordial non-Gaussianity and massive neutrinos. 2013, Phys. Rev. D, 88, 063526

Hinshaw, G., Spergel, D. N., Verde, L., et al., First-Year Wilkinson Microwave Anisotropy Probe (WMAP) Observations: The Angular Power Spectrum. 2003, ApJS, 148, 135

Hinshaw, G., Larson, D., Komatsu, E., et al., Nine-year Wilkinson Microwave Anisotropy Probe (WMAP) Observations: Cosmological Parameter Results. 2013, ApJS, 208, 19

Hirata, C. M., & Seljak, U., Reconstruction of lensing from the cosmic microwave background polarization. 2003, Phys. Rev. D, 68, 083002

Hirata, C. M., & Seljak, U., Intrinsic alignment-lensing interference as a contaminant of cosmic shear. 2004, Phys. Rev. D, 70, 063526

Hivon, E., Górski, K. M., Netterfield, C. B., et al., MASTER of the Cosmic Microwave Background Anisotropy Power Spectrum: A Fast Method for Statistical Analysis of Large and Complex Cosmic Microwave Background Data Sets. 2002, ApJ, 567, 2

Hoffman, Y., & Ribak, E., Constrained realizations of Gaussian fields - A simple algorithm. 1991, ApJ, 380, L5

Honscheid, K., DePoy, D. L., & for the DES Collaboration, The Dark Energy Camera (DECam). 2008, ArXiv e-prints, arXiv:0810.3600

Hou, Z., Aylor, K., Benson, B. A., et al., A Comparison of Maps and Power Spectra Determined from South Pole Telescope and Planck Data. 2017, ArXiv e-prints, arXiv:1704.00884

Howlett, C., Lewis, A., Hall, A., & Challinor, A., CMB power spectrum parameter degeneracies in the era of precision cosmology. 2012, J. Cosmology Astropart. Phys., 4, 027

Hu, W., Power Spectrum Tomography with Weak Lensing. 1999, ApJ, 522, L21

Hu, W., Weak lensing of the CMB: A harmonic approach. 2000, Phys. Rev. D, 62, 043007

Hu, W., & Dodelson, S., Cosmic Microwave Background Anisotropies. 2002, ARA&A, 40, 171

Hu, W., & Okamoto, T., Mass Reconstruction with Cosmic Microwave Background Polarization. 2002, ApJ, 574, 566

Hu, W., Sugiyama, N., & Silk, J., The Physics of Microwave Background Anisotropies. 1997, Nature, 386, 37

Huff, E., & Mandelbaum, R., Metacalibration: Direct Self-Calibration of Biases in Shear Measurement. 2017, ArXiv e-prints, arXiv:1702.02600

Hunter, J. D., Matplotlib: A 2D graphics environment. 2007, Computing In Science & Engineering, 9, 90

Hurier, G., Aghanim, N., Douspis, M., & Pointecouteau, E., Measurement of the T_{CMB} evolution from the Sunyaev-Zel'dovich effect. 2014, A&A, 561, A143

Jain, B., Spergel, D., Bean, R., et al., The Whole is Greater than the Sum of the Parts: Optimizing the Joint Science Return from LSST, Euclid and WFIRST. 2015, ArXiv e-prints, arXiv:1501.07897 [astro-ph.IM]

Jarvis, M. 2015, TreeCorr: Two-point correlation functions, Astrophysics Source Code Library, ascl:1508.007

Jarvis, M., Bernstein, G., & Jain, B., The skewness of the aperture mass statistic. 2004, MNRAS, 352, 338

Jarvis, M., Sheldon, E., Zuntz, J., et al., The DES Science Verification weak lensing shear catalogues. 2016, MNRAS, 460, 2245

Joachimi, B., Cacciato, M., Kitching, T. D., et al., Galaxy Alignments: An Overview. 2015, Space Sci. Rev., 193, 1

Kaiser, N., & Squires, G., Mapping the Dark Matter with Weak Gravitational Lensing. 1993, ApJ, 404, 441

Keisler, R., Reichardt, C. L., Aird, K. A., et al., A Measurement of the Damping Tail of the Cosmic Microwave Background Power Spectrum with the South Pole Telescope. 2011, ApJ, 743, 28

Kesden, M., Cooray, A., & Kamionkowski, M., Separation of Gravitational-Wave and Cosmic-Shear Contributions to Cosmic Microwave Background Polarization. 2002, Physical Review Letters, 89, 011304 (4 pages)

Kesden, M., Cooray, A., & Kamionkowski, M., Lensing reconstruction with CMB temperature and polarization. 2003, Phys. Rev. D, 67, 123507

Kilbinger, M., Cosmology with cosmic shear observations: a review. 2015, Reports on Progress in Physics, 78, 086901

Kirk, D., Omori, Y., Benoit-Lévy, A., et al., Cross-correlation of gravitational lensing from DES Science Verification data with SPT and Planck lensing. 2016, MNRAS, 459, 21

Krause, E., Eifler, T. F., Zuntz, J., et al., Dark Energy Survey Year 1 Results: Multi-Probe Methodology and Simulated Likelihood Analyses. 2017, ArXiv e-prints, arXiv:1706.09359

Landy, S. D., & Szalay, A. S., Bias and variance of angular correlation functions. 1993, ApJ, 412, 64

Laureijs, R., Amiaux, J., Arduini, S., et al., Euclid Definition Study Report. 2011, ArXiv e-prints, arXiv:1110.3193 [astro-ph.CO]

Lee, A. T., Ade, P., Balbi, A., et al., A High Spatial Resolution Analysis of the MAXIMA-1 Cosmic Microwave Background Anisotropy Data. 2001, ApJ, 561, L1

Lewis, A., Lensed CMB simulation and parameter estimation. 2005, Phys. Rev. D, 71, 083008

Lewis, A., & Challinor, A., Weak gravitational lensing of the CMB. 2006, Phys. Rep., 429, 1

Lewis, A., Challinor, A., & Lasenby, A., Efficient Computation of CMB anisotropies in closed FRW models. 2000, Astrophys. J., 538, 473

Lewis, A., Challinor, A., & Lasenby, A., Efficient Computation of Cosmic Microwave Background Anisotropies in Closed Friedmann-Robertson-Walker Models. 2000, ApJ, 538, 473

Linde, A. D., A new inflationary universe scenario: A possible solution of the horizon, flatness, homogeneity, isotropy and primordial monopole problems. 1982, Physics Letters B, 108, 389

Liu, J., & Hill, J. C., Cross-correlation of Planck CMB lensing and CFHTLenS galaxy weak lensing maps. 2015, Phys. Rev. D, 92, 063517

Liu, J., Ortiz-Vazquez, A., & Hill, J. C., Constraining multiplicative bias in CFHTLenS weak lensing shear data. 2016, Phys. Rev. D, 93, 103508

LSST Science Collaboration, Abell, P. A., Allison, J., et al., LSST Science Book, Version 2.0. 2009, ArXiv e-prints, arXiv:0912.0201 [astro-ph.IM]

Lyth, D. H. D. H., & Riotto, A. A., Particle physics models of inflation and the cosmological density perturbation. 1999, Phys. Rep., 314, 1

Marriage, T. A., Acquaviva, V., Ade, P. A. R., et al., The Atacama Cosmology Telescope: Sunyaev-Zel'dovich-Selected Galaxy Clusters at 148 GHz in the 2008 Survey. 2011, ApJ, 737, 61

Mather, J. C., Cheng, E. S., Eplee, Jr., R. E., et al., A preliminary measurement of the cosmic microwave background spectrum by the Cosmic Background Explorer (COBE) satellite. 1990, ApJ, 354, L37

Mather, J. C., Cheng, E. S., Cottingham, D. A., et al., Measurement of the cosmic microwave background spectrum by the COBE FIRAS instrument. 1994, ApJ, 420, 439

Melchior, P., Gruen, D., McClintock, T., et al., Weak-lensing mass calibration of redMaPPer galaxy clusters in Dark Energy Survey Science Verification data. 2017, MNRAS, 469, 4899

Miller, A. D., Caldwell, R., Devlin, M. J., et al., A Measurement of the Angular Power Spectrum of the Cosmic Microwave Background from l = 100 to 400. 1999, ApJ, 524, L1

Miralda-Escude, J., Gravitational lensing by clusters of galaxies - Constraining the mass distribution. 1991, ApJ, 370, 1

Miyazaki, S., Komiyama, Y., Nakaya, H., et al. 2012, in Proc. SPIE, Vol. 8446, Ground-based and Airborne Instrumentation for Astronomy IV, 84460Z

Mo, H., van den Bosch, F. C., & White, S. 2010, Galaxy Formation and Evolution

Munshi, D., Porciani, C., & Wang, Y., Galaxy clustering and dark energy. 2004, MNRAS, 349, 281

Namikawa, T., Hanson, D., & Takahashi, R., Bias-hardened CMB lensing. 2013, MNRAS, 431, 609

Namikawa, T., Yamauchi, D., & Taruya, A., Full-sky lensing reconstruction of gradient and curl modes from CMB maps. 2012, J. Cosmology Astropart. Phys., 1, 007

Netterfield, C. B., Ade, P. A. R., Bock, J. J., et al., A Measurement by BOOMERANG of Multiple Peaks in the Angular Power Spectrum of the Cosmic Microwave Background. 2002, ApJ, 571, 604

Nicola, A., Refregier, A., & Amara, A., Integrated cosmological probes: Extended analysis. 2017, Phys. Rev. D, 95, 083523

Norberg, P., Baugh, C. M., Gaztañaga, E., & Croton, D. J., Statistical analysis of galaxy surveys - I. Robust error estimation for two-point clustering statistics. 2009, MNRAS, 396, 19

Okamoto, T., & Hu, W., Cosmic microwave background lensing reconstruction on the full sky. 2003, Phys. Rev. D, 67, 083002

Omori, Y., Chown, R., Simard, G., et al., A 2500 square-degree CMB lensing map from combined South Pole Telescope and Planck data. 2017, ArXiv e-prints, arXiv:1705.00743

Peacock, J. A. 1999, Cosmological Physics, 704

Pearson, R., & Zahn, O., Cosmology from cross correlation of CMB lensing and galaxy surveys. 2014, Phys. Rev. D, 89, 043516

Peebles, P. J. E., Recombination of the Primeval Plasma. 1968, ApJ, 153, 1

Penzias, A. A., & Wilson, R. W., A Measurement of Excess Antenna Temperature at 4080 Mc/s. 1965, ApJ, 142, 419

Pérez, F., & Granger, B. E., IPython: A System for Interactive Scientific Computing. 2007, Computing in Science & Engineering, 9, 21

Planck Collaboration, Ade, P. A. R., Aghanim, N., et al., Planck 2013 results. XV. CMB power spectra and likelihood. 2014a, A&A, 571, A15

Planck Collaboration, Ade, P. A. R., Aghanim, N., et al., Planck 2013 results. XVI. Cosmological parameters. 2014b, A&A, 571, A16

Planck Collaboration, Ade, P. A. R., Aghanim, N., et al., Planck 2013 results. XVIII. The gravitational lensing-infrared background correlation. 2014c, A&A, 571, A18

Planck Collaboration, Ade, P. A. R., Aghanim, N., et al., Planck 2015 results. II. Low Frequency Instrument data processings. 2016a, A&A, 594, A2

Planck Collaboration, Aghanim, N., Ashdown, M., et al., Planck intermediate results. XLVIII. Disentangling Galactic dust emission and cosmic infrared background anisotropies. 2016b, A&A, 596, A109

Planck Collaboration I., Planck 2015 results. I. Overview of products and scientific results. 2015, ArXiv e-prints, arXiv:1502.01582

Planck Collaboration VIII., Planck 2015 results. VIII. High Frequency Instrument data processing: Calibration and maps. 2015, ArXiv e-prints, arXiv:1502.01587

Planck Collaboration XII., Planck 2015 results. XII. Full focal plane simulations. 2016, A&A, 594, A12

Planck Collaboration XV., Planck 2015 results. XV. Gravitational lensing. 2015, ArXiv e-prints, arXiv:1502.01591

Prat, J., Sánchez, C., Miquel, R., et al., Galaxy bias from galaxy-galaxy lensing in the DES Science Verification Data. 2016, ArXiv e-prints, arXiv:1609.08167

Prat, J., Sánchez, C., Fang, Y., et al., Dark Energy Survey Year 1 Results: Galaxy-Galaxy Lensing. 2017, ArXiv e-prints, arXiv:1708.01537

Quenouille, M. H., Problems in Plane Sampling. 1949, The Annals of Mathematical Statistics, 20, 355

Reichardt, C. L., Shaw, L., Zahn, O., et al., A Measurement of Secondary Cosmic Microwave Background Anisotropies with Two Years of South Pole Telescope Observations. 2012, ApJ, 755, 70

Reichardt, C. L., Stalder, B., Bleem, L. E., et al., Galaxy Clusters Discovered via the Sunyaev-Zel'dovich Effect in the First 720 Square Degrees of the South Pole Telescope Survey. 2013, ApJ, 763, 127

Rozo, E., Rykoff, E. S., Abate, A., et al., redMaGiC: selecting luminous red galaxies from the DES Science Verification data. 2016, MNRAS, 461, 1431

Rykoff, E. S., Rozo, E., Busha, M. T., et al., redMaPPer. I. Algorithm and SDSS DR8 Catalog. 2014, ApJ, 785, 104

Rykoff, E. S., Rozo, E., Hollowood, D., et al., The RedMaPPer Galaxy Cluster Catalog From DES Science Verification Data. 2016, ApJS, 224, 1

Sadeh, I., Abdalla, F. B., & Lahav, O., ANNz2: Photometric Redshift and Probability Distribution Function Estimation using Machine Learning. 2016, PASP, 128, 104502

Sato, K., First-order phase transition of a vacuum and the expansion of the Universe. 1981, MNRAS, 195, 467

Schaan, E., Krause, E., Eifler, T., et al., Looking through the same lens: shear calibration for LSST, Euclid and WFIRST with stage 4 CMB lensing. 2016, ArXiv e-prints, arXiv:1607.01761

Schneider, P., Ehlers, J., & Falco, E. E. 1992, Gravitational Lenses, 112

Schneider, P., van Waerbeke, L., & Mellier, Y., B-modes in cosmic shear from source redshift clustering. 2002, A&A, 389, 729

Seitz, C., & Schneider, P., Steps towards nonlinear cluster inversion through gravitational distortions. III. Including a redshift distribution of the sources. 1997, A&A, 318, 687

Seljak, U., & Zaldarriaga, M., A Line-of-Sight Integration Approach to Cosmic Microwave Background Anisotropies. 1996, ApJ, 469, 437

Shao, J., Discussion: Jackknife, Bootstrap and Other Resampling Methods in Regression Analysis. 1986, Ann. Statist., 14, 1322

Shaw, L. D., Nagai, D., Bhattacharya, S., & Lau, E. T., Impact of Cluster Physics on the Sunyaev-Zel'dovich Power Spectrum. 2010, ApJ, 725, 1452

Shaw, L. D., Rudd, D. H., & Nagai, D., Deconstructing the Kinetic SZ Power Spectrum. 2012, ApJ, 756, 15

Sheldon, E. S., An implementation of Bayesian lensing shear measurement. 2014, MNRAS, 444, L25

Sheldon, E. S., & Huff, E. M., Practical Weak Lensing Shear Measurement with Metacalibration. 2017, ArXiv e-prints, arXiv:1702.02601

Smith, K. M., Zahn, O., & Doré, O., Detection of gravitational lensing in the cosmic microwave background. 2007, Phys. Rev. D, 76, 043510

Smoot, G. F., Bennett, C. L., Kogut, A., et al., Structure in the COBE differential microwave radiometer first-year maps. 1992, ApJ, 396, L1

Spergel, D., Gehrels, N., Breckinridge, J., et al., WFIRST-2.4: What Every Astronomer Should Know. 2013, ArXiv e-prints, arXiv:1305.5425 [astro-ph.IM]

Squires, G., & Kaiser, N., Unbiased Cluster Lens Reconstruction. 1996, ApJ, 473, 65

Story, K. T., Reichardt, C. L., Hou, Z., et al., A Measurement of the Cosmic Microwave Background Damping Tail from the 2500-Square-Degree SPT-SZ Survey. 2013, ApJ, 779, 86

Story, K. T., Hanson, D., Ade, P. A. R., et al., A Measurement of the Cosmic Microwave Background Gravitational Lensing Potential from 100 Square Degrees of SPTpol Data. 2015, ApJ, 810, 50

Swetz, D. S., Ade, P. A. R., Amiri, M., et al., Overview of the Atacama Cosmology Telescope: Receiver, Instrumentation, and Telescope Systems. 2011, ApJS, 194, 41

Szapudi, I., Prunet, S., Pogosyan, D., Szalay, A. S., & Bond, J. R., Fast Cosmic Microwave Background Analyses via Correlation Functions. 2001, ApJ, 548, L115

The Dark Energy Survey Collaboration, The Dark Energy Survey. 2005, ArXiv Astrophysics e-prints, astro-ph/0510346

Troxel, M. A., MacCrann, N., Zuntz, J., et al., Dark Energy Survey Year 1 Results: Cosmological Constraints from Cosmic Shear. 2017, ArXiv e-prints, arXiv:1708.01538

Vallinotto, A., Using Cosmic Microwave Background Lensing to Constrain the Multiplicative Bias of Cosmic Shear. 2012, ApJ, 759, 32

van der Walt, S., Colbert, S. C., & Varoquaux, G., The NumPy Array: A Structure for Efficient Numerical Computation. 2011, Computing in Science & Engineering, 13, 22

van Engelen, A., Bhattacharya, S., Sehgal, N., et al., CMB Lensing Power Spectrum Biases from Galaxies and Clusters Using High-angular Resolution Temperature Maps. 2014, ApJ, 786, 13

van Engelen, A., Keisler, R., Zahn, O., et al., A Measurement of Gravitational Lensing of the Microwave Background Using South Pole Telescope Data. 2012, ApJ, 756, 142

van Uitert, E., Joachimi, B., Joudaki, S., et al., KiDS+GAMA: Cosmology constraints from a joint analysis of cosmic shear, galaxy-galaxy lensing and angular clustering. 2017, ArXiv e-prints, arXiv:1706.05004

Viero, M. P., Wang, L., Zemcov, M., et al., HerMES: Cosmic Infrared Background Anisotropies and the Clustering of Dusty Star-forming Galaxies. 2013, ApJ, 772, 77

Wright, E. L., Eisenhardt, P. R. M., Mainzer, A. K., et al., The Wide-field Infrared Survey Explorer (WISE): Mission Description and Initial On-orbit Performance. 2010, AJ, 140, 1868

Xavier, H. S., Abdalla, F. B., & Joachimi, B., Improving lognormal models for cosmological fields. 2016, MNRAS, 459, 3693

York, D. G., Adelman, J., Anderson, Jr., J. E., et al., The Sloan Digital Sky Survey: Technical Summary. 2000, AJ, 120, 1579

Zel'dovich, Y. B., Kurt, V. G., & Syunyaev, R. A., Recombination of Hydrogen in the Hot Model of the Universe. 1969, Soviet Journal of Experimental and Theoretical Physics, 28, 146

Zuntz, J., Kacprzak, T., Voigt, L., et al., IM3SHAPE: a maximum likelihood galaxy shear measurement code for cosmic gravitational lensing. 2013, MNRAS, 434, 1604

Zuntz, J., Paterno, M., Jennings, E., et al., CosmoSIS: Modular cosmological parameter estimation. 2015, Astronomy and Computing, 12, 45

Zuntz, J., Sheldon, E., Samuroff, S., et al., Dark Energy Survey Year 1 Results: Weak Lensing Shape Catalogues. 2017, ArXiv e-prints, arXiv:1708.01533